Quantification of Imaging Biomarkers For Cardiovascular Disease in CT(A)

Rahil Shahzad

QUANTIFICATION OF IMAGING BIOMARKERS FOR CARDIOVASCULAR DISEASE IN CT(A)

Rahil Shahzad

Cover design by Rahil Shahzad & Frans van den Biggelaar.
About the cover:
Painting with light. The image on the front page represents the heart, the coronary arteries and the layer of epicardial fat surrounding the heart.

QUANTIFICATION OF IMAGING BIOMARKERS FOR CARDIOVASCULAR DISEASE IN CT(A)

PROEFSCHRIFT

ter verkrijging van de graad van doctor
aan de Technische Universiteit Delft,
op gezag van de Rector Magnificus prof. ir. K.C.A.M. Luyben,
voorzitter van het College voor Promoties,
in het openbaar te verdedigen op maandag 4 november 2013 om 12:30 uur

door

Rahil SHAHZAD

Master of Science in Biomedical Engineering, University of Warwick
geboren te Bangalore (India)

Dit proefschrift is goedgekeurd door de promotoren:
Prof. dr. W.J. Niessen
Prof. dr. ir. L.J. van Vliet

Copromotor:
Dr. ir. T. van Walsum

Samenstelling promotiecommissie:

Rector Magnificius	voorzitter
Prof. dr. W.J. Niessen	Erasmus MC, Universitair Medisch Centrum Rotterdam en Technische Universiteit Delft, promotor
Prof. dr. ir. L.J. van Vliet	Technische Universiteit Delft, promotor
Dr. ir. T. van Walsum	Erasmus MC, Universitair Medisch Centrum Rotterdam, copromotor
Prof. dr. ir. B.P.F. Lelieveldt	Leids Universitair Medisch Centrum en Technische Universiteit Delft
Prof. dr. ir. M. Orkisz	Universite Claude Bernard Lyon
Prof. Dr. R. Razavi	King's College London
Prof. Dr. A. van der Lugt	Erasmus MC, Universitair Medisch Centrum Rotterdam
Prof. dr. ir. N. de Jong	Erasmus MC, Universitair Medisch Centrum Rotterdam en Technische Universiteit Delft, reservelid

The work in this thesis was conducted at the Quantitative Imaging Group (QI), Faculty of Applied Sciences, Delft University of Technology and at the Biomedical Imaging Group Rotterdam (BIGR), Departments of Radiology and Medical Informatics, Erasmus MC, University Medical Center, Rotterdam, The Netherlands. The work was financially supported by the Dutch Ministry of Economic Affairs (AgentschapNL) under the title "'Het Hart in Drie Dimensies'" (PID06003).

Financial support by
Quantitative Imaging Group (QI), Faculty of Applied Sciences, Delft University of Technology
Medis medical imaging bv, Leiden
BioClinica, Leiden
for the publication of this thesis is gratefully acknowledged.

Printed by GVO Drukkers en Vormgevers BV

ISBN 978-90-6464-705-5

Contents

Dedicated to the bright memory of my late father Shafeeulla Shahzad.
Who has been my best teacher, always encouraged me
and gave me the freedom to do the things I love.

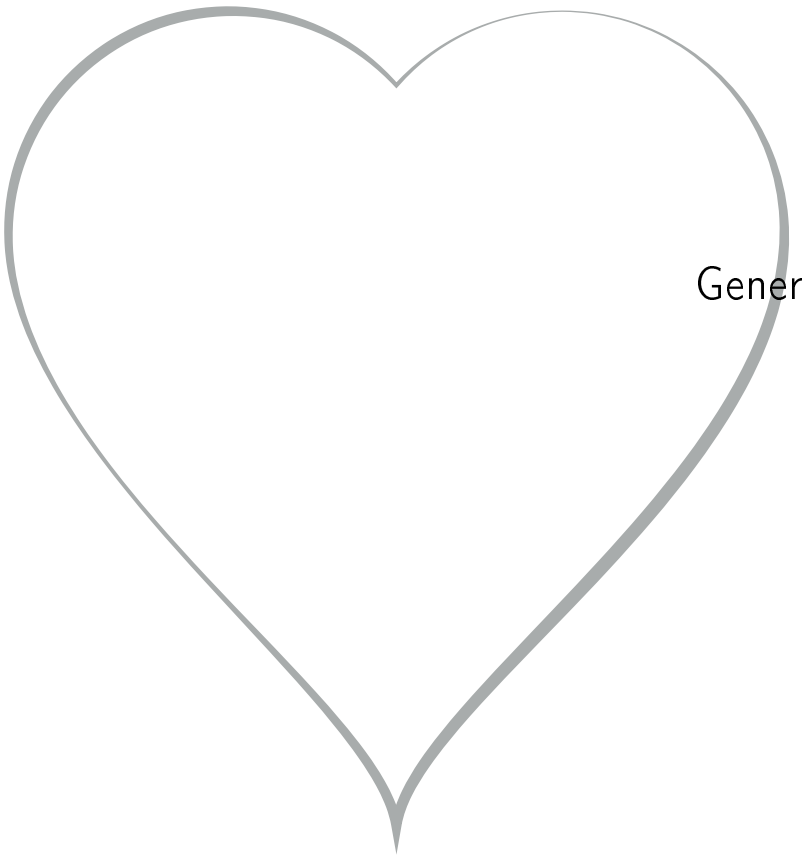

1

General Introduction

Although the average life expectancy of humans has increased dramatically over the last decades (Oeppen and Vaupel, 2002), and despite advances in cardiovascular diagnosis and treatment, cardiovascular related deaths still remain the leading cause of mortality worldwide. It is estimated that by 2030 almost 25 million people per year will die from cardiovascular diseases (CVDs) (WHO, 2012). Generally, CVDs remain unnoticed over a long period of time and when symptoms start appearing the disease may have an advanced stage. Coronary artery diseases (CAD), is the CVD associated with the highest mortality. CAD will ultimately result in reduced blood supply to the cardiac muscle resulting in a permanent damage to the tissue (ischemia). The development of CVD and the risk of a subject having a cardiovascular related event in the near future can be predicted by monitoring risk factors associated to CAD e.g. smoking, obesity, raised lipid levels, blood pressure, diabetes, etc.,

Advances in imaging technologies permit assessment of anatomical and functional heart parameters which may be used to detect the presence of CAD, monitor its progression, and predict the likeliness of future clinical events. Deriving this information from image data either visually or manually can be an overwhelming and tedious task. In order to facilitate the clinicians in the extraction of quantitative information, there is large interest in activities in developing software programs for automating this task.

In this thesis, we describe techniques that we developed and evaluated for automatic extraction of quantitative imaging biomarkers for CVD. In the following sections a brief introduction to cardiac anatomy (1.1), coronary artery disease (1.2), cardiac imaging techniques (1.3), and quantitative imaging biomarkers for cardiovascular disease (1.4) is provided. Lastly, the outline of the thesis is presented in Section 1.5.

1.1 Cardiac anatomy

The heart is an essential organ that supplies blood to the rest of the body through a network of blood vessels. The blood supply chain consists of a network of arteries that originate from the aorta and carry blood from the heart, and a network of veins that carry blood back to the heart. The heart is made up of four chambers: two atria which receive blood coming back to the heart and two ventricles which pump blood out of the heart. The blood coming in through the right atrium is oxygen deficit and is pumped to the lungs via the right ventricle. In the lungs the blood gets enriched with oxygen and returns back to the heart through the left atrium. The heart then pumps this blood to other parts of the body via the left ventricle. Four different types of valves are present between the chambers to maintain a unidirectional blood flow. A web of nerve tissues conducts complex electrical signals that govern the contraction and relaxation of the heart. A protective layer called the pericardial sac covers the heart. Figure 1.1 shows a schematic view of the heart.

Since the heart in itself is made up of muscle tissue (cardiac muscle), it also needs its own share of oxygen rich blood supply. Approximately 5% of the total blood being pumped out of the heart is supplied back to the cardiac muscle through a

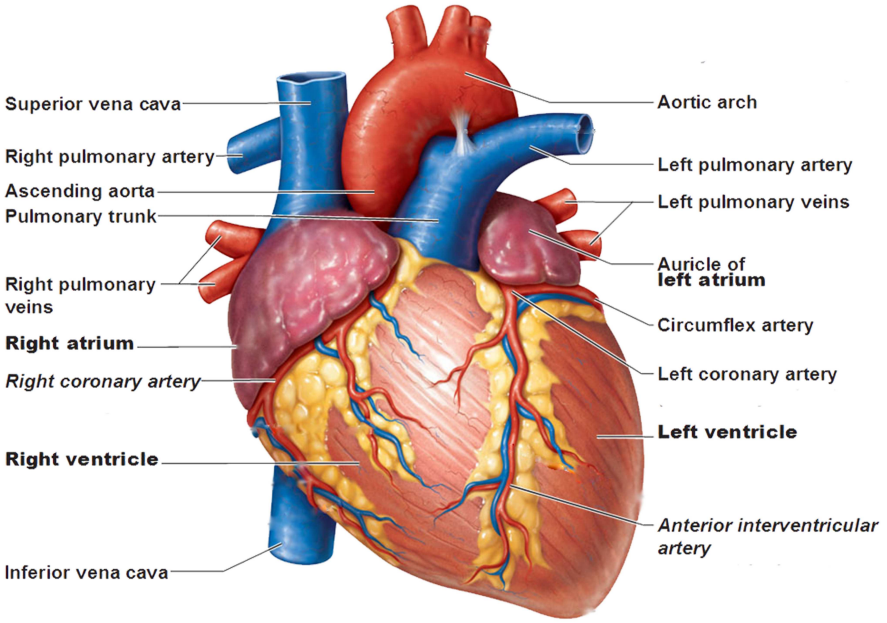

Figure 1.1: Anatomy of the heart. (adapted from www.antranik.org)

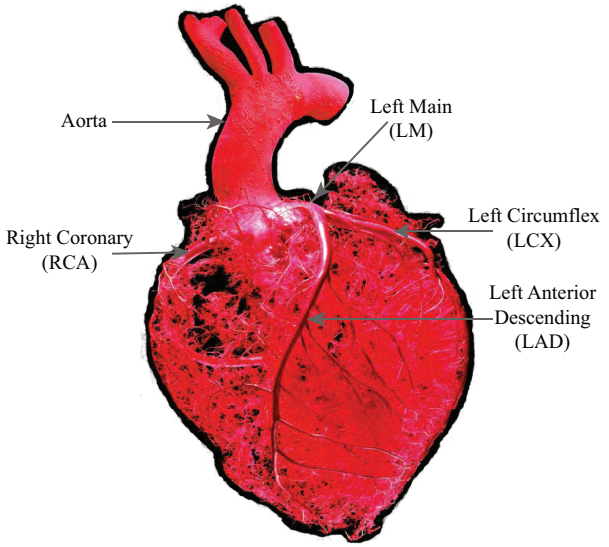

Figure 1.2: Resin cast of the Coronary Arteries (adapted from www.bodyworlds.com)

network of arteries called coronary arteries. The coronary arteries are divided into two branches, the left branch and the right branch, which originate at the beginning of the aorta. Both branches of the coronary arteries are further divided into smaller arteries, eventually branching into capillaries. There are four main branches of the coronary arteries: the left main (LM), the left anterior descending (LAD), the left circumflex (LCX), and the right coronary artery (RCA). Figure 1.2 shows a cast of the coronary arteries.

1.2 Coronary artery disease

CAD causes buildup of plaque in the walls of the arteries. This process is called atherosclerosis. The coronary artery, which is smooth and elastic when healthy, starts to become narrow and rigid due to the buildup of plaque. Plaque consists of fatty substances like cholesterol and other materials such as calcium. Figure 1.3 shows the evolution of atherosclerosis. Due to the narrowing of the artery, the flow of blood is hindered which causes ischemia. If the ischemia is prolonged then a myocardial infarction (heart attack) may occur. Hence it is very important to detect CAD in a very early stage, so appropriate measures can be taken to prevent future cardiac events.

Atherosclerosis was thought to be a disease of modern times, but a recent study conducted by Thompson et al. (Thompson et al., 2013) shows that atherosclerosis is an ancient disease spanning more than 4000 years. The study was performed by CT scanning of 137 mummies from four different geographical regions (ancient Egypt, ancient Peru, the Ancestral Puebloans of south-west America, and the Unangan of the Aleutian Islands) and inspecting the major arteries and the coronaries. It was found that 34% of the mummies had clear deposits of calcium in the arteries, indicating the presence of atherosclerosis.

1.3 Cardiac imaging techniques

Several imaging techniques are available for imaging the coronary arteries.

Conventional Coronary Angiography (CCA) is an X-ray projection technique used to visually assess the coronary arteries. Contrast material is injected into the arteries to increase the contrast within the vessel, for visualization of the lumen. The contrast material is delivered at the origin of the coronary arteries via a catheter. The catheter is usually inserted through the femoral artery in the thigh and advanced into the ascending aorta. This imaging technique results in a two-dimensional (2D) image which is used by a cardiologist to investigate luminal narrowing (stenosis) in the arteries. The visualized stenosis can further be classified as significant if the narrowing in the lumen is $\geq$ 50%. In current practice, CCA is the gold standard imaging technique for diagnosing CAD. Figure 1.4 shows an example of the scanner.

Computed Tomography (CT) is a widely used technique to image the heart and the coronary arteries. CT imaging uses a rotating X-rays source and detectors to enable three-dimensional (3D) image reconstruction. X-rays passing through a subject are partially attenuated depending on the composition of the tissues. The

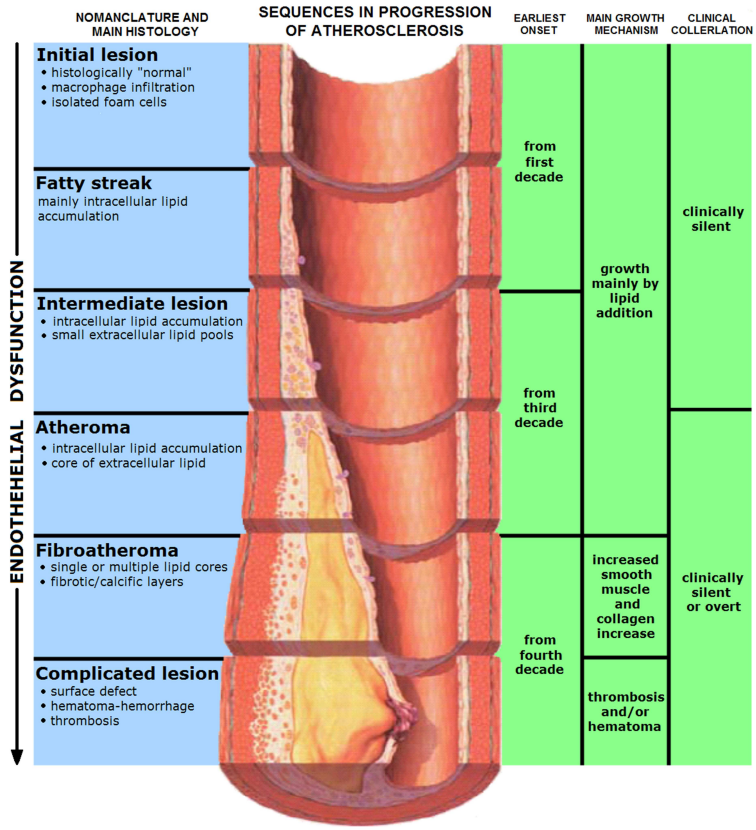

Figure 1.3: Progress of atherosclerosis over time and the different stages (source: wikimedia).

transmitted X-rays are collected by a series of detectors. A 3D image is then digitally reconstructed. Filtered back projection has traditionally been most widely used but is increasingly replaced by iterative algebraic reconstruction techniques. Cardiac CT images are commonly used to assess the presence of calcified lesions. Figure 1.5 shows an example of a CT scanner.

Computed Tomography Angiography (CTA) is a technique where the same principle as CT is used to acquire and reconstruct a 3D image after a iodine based contrast material is injected intravenously. The presence of contrast material makes it easier to visualize the cardiac chambers, coronary arteries and the other structures within the heart. Cardiac CTA images are used to assess the cardiac anatomy and coronary artery lumen. Information such as, lumen narrowing (stenosis), plaque location and plaque composition can be obtained from CTA images. Figure 1.7 shows an example of a CT and a CTA image, the difference due to the contrast material between the two imaging modalities can easily be compared.

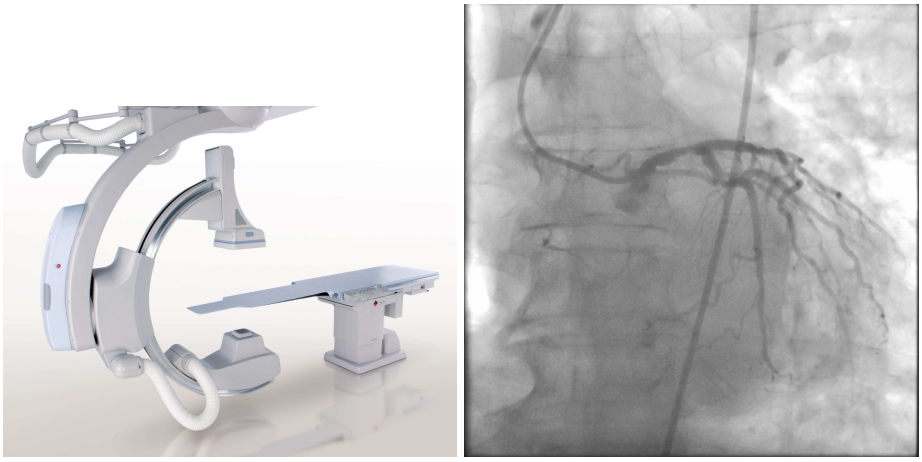

(a) (b)

Figure 1.4: (a) A mono-plane X-ray system . The patient is placed on the table and the C-arm with the X-ray source and the detector is positioned accordingly to acquire the angiogram. (Image copyright Toshiba) (b) An example of the CCA image.

Single-Photon Emission Computed Tomography (SPECT) is a technique were a small amount of radioactive material called radionuclide is intravenously injected into the subject. Based on the type of radionuclide used, it gets bound to a specific tissue. Due to its radioactive nature the radionuclide starts decaying by emitting gamma radiation. These gamma radiations are detected by a gamma camera. Similar to the CT imaging principle, one or more gamma cameras rotate around the subject, acquiring multiple 2D images. A 3D image is then computationally reconstructed by using a computer algorithm. SPECT is used in functional cardiac imaging called myocardial perfusion imaging (MPI). Figure 1.8 shows an example of the scanner and the SPECT image it produces.

1.4 Quantitative imaging biomarkers of cardiovascular disease

Biomarker is a term used for a detectable biological source that could indicate the presence or state of a disease, or the response to a treatment. An imaging biomarker is a feature that is detectable using an imaging modality. Accurate quantification of these imaging biomarkers is of utmost importance, because not only the presence, but also the (feature) distribution and the extent/severity of biomarkers may indicate the stage of a disease, and can potentially be used for predicting the evolution of the disease. Based on these findings the patients can be grouped into different risk categories for disease management, i.e. suitable intervention or treatment planning.

In this thesis we mainly focus on quantitative imaging biomarkers for cardiovascular diseases. The imaging biomarkers that we investigated are described in more detail in the following paragraphs.

Figure 1.5: A CT scanner. Subject is placed on the moving table. Rotating X-ray source and detectors are placed within the circular encasing. (Image copyright Siemens AG)

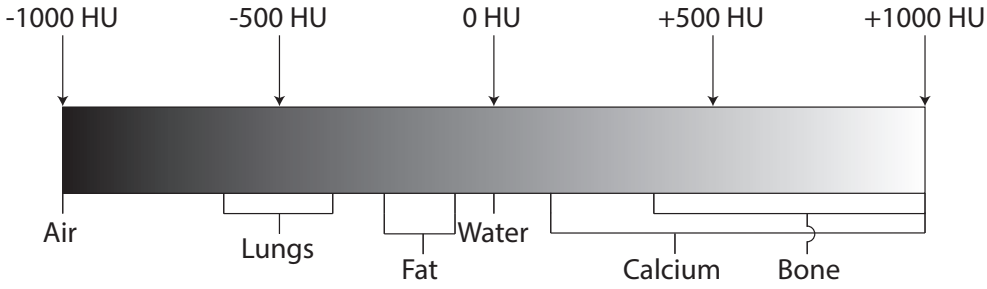

Figure 1.6: Houndsfield attenuation range for various tissue types.

Calcified lesions in the arteries indicate the presence of atherosclerosis. The amount of calcified lesions in the coronary artery indicates the severity of CAD (Rosen et al., 2009). Hence, calcified lesions are one of the important biomarkers of CAD. Calcium can be easily visualized on a CT scan. Calcium lesions have the same attenuation coefficient as that of bone (see Figure 1.6) and appear as bright objects on the scan. They can be detected by setting a threshold level of 130 HU (Agatston et al., 1990). The amount and location of calcium lesions in the coronary arteries indicate the extent and severity of Atherosclerosis. The process of quantifying the amount of calcifications in the arteries is called calcium scoring. There are three widely used calcium scoring algorithms, Agatston score (Agatston et al., 1990), volume score (Callister et al., 1998) and mass score (Hong et al., 2002). Based on the value of the calcium scores and other factors such as the Framingham risk factors, subjects can be assigned into various risk categories (Greenland et al., 2004; Shaw et al., 2003).

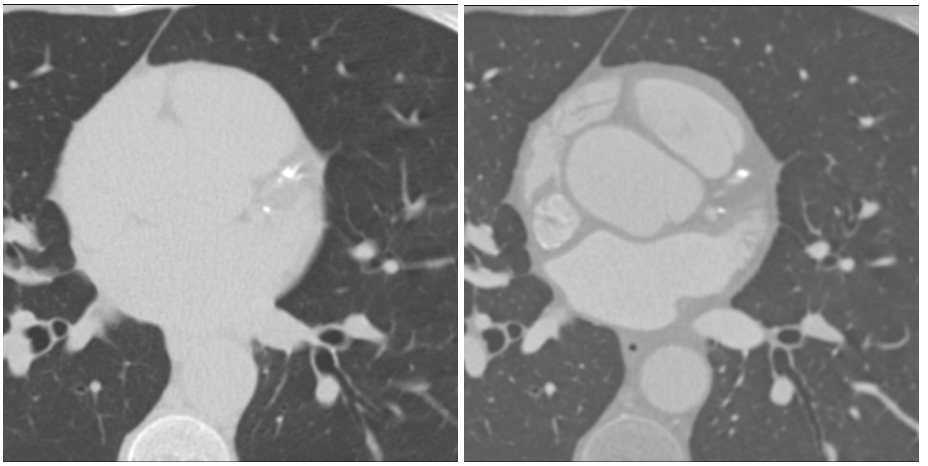

(a) (b)

Figure 1.7: A randomly selected axial slice from a subject. (a) CT scan, (b) corresponding CTA scan.

The *Agatston score* is the most widely used scoring technique and was originally proposed for electron beam CT (EBCT) scanners and is defined as:

$$Ag = \sum_{s=1}^{n} A_s * w_s \ , \tag{1.1}$$

where s is the the slice number of the lesion, A the area of the lesion on slice s and w the weighting factor of the lesion. w is defined as:

$$w = \begin{cases} 1 & 130HU \leq I_s < 200HU \\ 2 & 200HU \leq I_s < 300HU \\ 3 & 300HU \leq I_s < 400HU \\ 4 & 400HU \leq I_s. \end{cases} \tag{1.2}$$

where, I_s is the max intensity value of the calcification on slice s.

The aforementioned definition was used on EBCT scanners that had a slice thickness of 3mm. To use this method on modern CT scanners, a normalized Agatston score (Ohnesorge et al., 2002) is used:

$$Ag_n = \frac{IN}{SW} \sum_{s=1}^{n} A_s * w_s \ , \tag{1.3}$$

where IN is the slice increment and SW the slice thickness. The total Agatston score is computed by summing all the individual lesion scores.

(a)

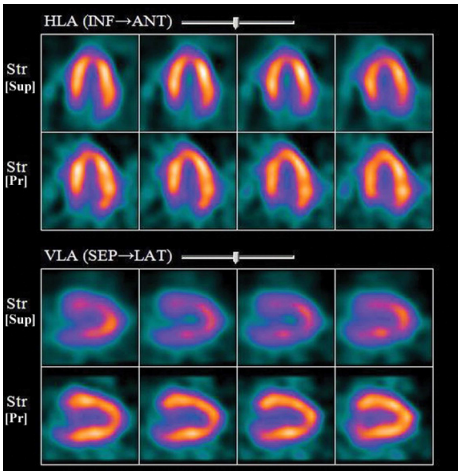

(b)

Figure 1.8: (a) A SPECT scanner. The rectangle boxes in front of the circular encasing (upgradable into a CT-SPECT scanner) are the two gamma cameras. (Image copyright Siemens AG) (b) Example of a typical SPECT image.

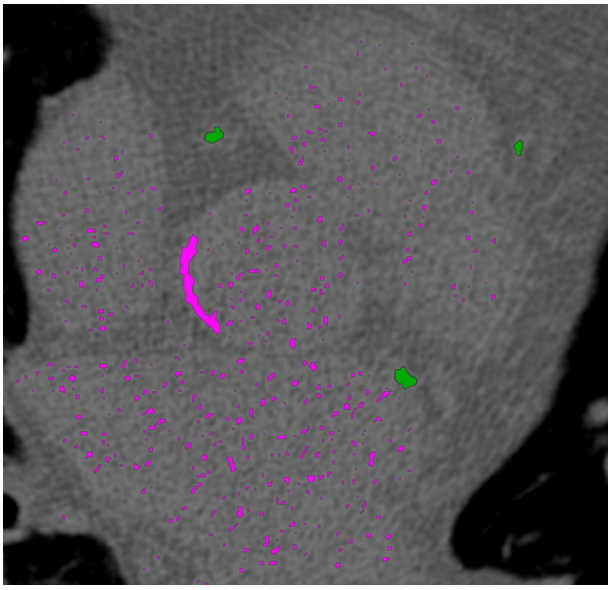

Figure 1.9: A randomly selected axial CT slice. Green objects are the coronary artery calcium lesions, pink objects have characteristics similar to calcium lesions but are actually noise and calcium lesions outside the coronary arteries.

Due to the non-linear scale of the weighting factor w in the Agatston score, a new method was proposed by Callister et al., the so-called *volume score*:

$$V = \sum_{i=1}^{n} N_i * v \quad , \tag{1.4}$$

where i is the lesion index, N the number of segmented voxels and v is the volume of the voxel.

The volume score does not measure the actual composition of the calcium plaque but the relative volume. An absolute scoring method was proposed by Hong et al. based on the hydroxyapatite density of the calcium lesion. This measure was called the *mass score* and is defined as:

$$M = \sum_{i=1}^{n} \overline{CT}_i * v_i * C \quad , \tag{1.5}$$

where $\overline{CT}_i$ is the mean intensity of the calcium lesion, v_i the volume of the lesion and C is the calibration factor for hydroxyapatite.

The main challenge for calcium quantification is the ability to distinguish true lesions from noise. Since the calcium scoring CT protocol uses a very low radiation dose, the images obtained are noisy. It is also difficult to distinguish the coronary arteries from the surrounding tissue. This makes it more difficult to assign the detected calcium lesion to a particular artery. An example is presented in Figure 1.9.

Epicardial fat is the adipose tissue found between the myocardium and the visceral layer of the pericardium. This fat tissue directly surrounds the entire heart and the coronary arteries. Increasing evidence suggests that the epicardial fat tissue surrounding the coronary arteries contribute to the local production of inflammatory factors, which in turn increases the risk of atherosclerosis (Cheng et al., 2007; Iacobellis et al., 2005). Adipose tissue can be quantified on a CT scan, fat tissue voxels appear on the scans with an attenuation value in the range between -200HU to -30HU (Yoshizumi et al., 1999) (see Figure 1.6). A typical Cardiac CT scan has three types of fat tissue within its FOV: Visceral fat (located around the abdomen), Inter-thoracic fat (located between the chest wall and pericardium) and epicardial fat (contained within the pericardium). Figure 1.10 shows an example of the different fat tissues on an axial slice. The volume of epicardial fat voxels can be quantified by first delineating the heart from the surrounding structures.

The main challenge lying in the quantification of epicardial fat is the ability to accurately delineate the pericardium. The pericardium appears as a very thin membrane around the heart. The scans used for epicardial fat quantification are the same as those used for calcium scoring. Hence, we have to deal with the issues regarding image noise and the absence of intravenous contrast material. Both issues make it difficult to distinguish between the different cardiac structures.

Lumen narrowing or stenosis is caused due to the buildup of plaque as explained in Section 1.2 (see Figure 1.3). It is important to accurately quantify the degree of stenosis. The degree of stenosis indicates the presence of obstructive CAD.

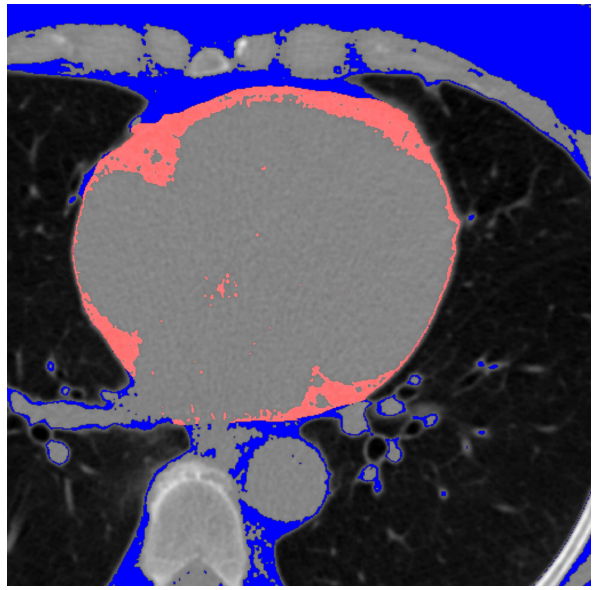

Figure 1.10: Adipose tissues overlaid on the CT scan. The red region indicates epicardial fat tissue; The blue region represents the visceral and inter-thoracic fat tissue. Due to partial volume effects some noise in the lung nodules is also picked up as fat.

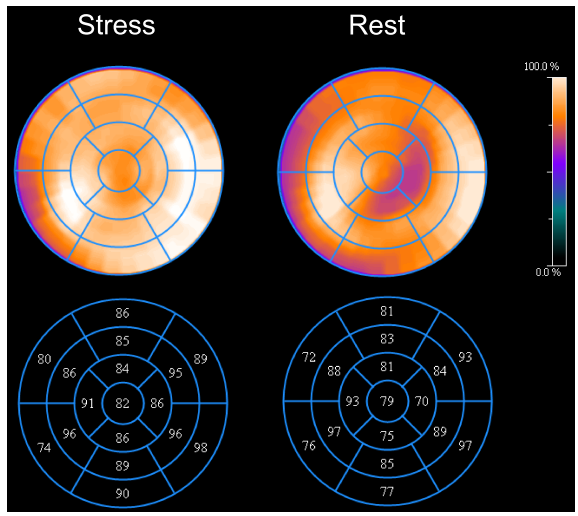

Figure 1.11: Example of the 17-segment model with stress and rest polar maps used for interpretation.

Obstructive CAD is directly associated with myocardial infarction. Hence, it is of utmost importance to be able to accurately quantify the amount of luminal narrowing, such that further preventive measures can be taken. Stenosis degree is measured using the CCA scan which is considered to be the gold standard. The degree of stenosis can also be quantified on a CTA scan. Additional information such as the plaque composition can also be derived from the CTA scan. The presence of contrast material within the coronary arteries makes it easier to visualize and quantify the lumen morphology. Figure 1.12 shows a curved multi-planar reformatted image of a coronary artery with a few stenoses.

The main challenge in quantifying the degree of stenosis is the ability to distinguish between obstructive and non-obstructive luminal narrowing. A stenosis is said to be obstructive when the lumen is more that 50% occluded. The radius of the lumen is computed by segmenting the lumen. In order to compute the degree of stenosis of a diseased vessel segment, the estimated radius of the healthy lumen is calculated from the true radius by applying a regression approach.

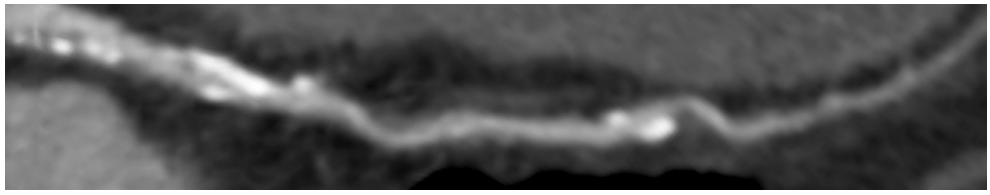

Figure 1.12: A curved multi-planar reformatted image of a LAD coronary artery. It can be observed that the presence of calcium lesions within the coronary artery causes luminal narrowing.

Myocardial Perfusion is used to assess the function of the heart muscle (myocardium). If the myocardium receives less blood supply due to an obstructive stenosis caused by CAD, the myocardium is said to be diseased (myocardial ischemia). The presence and extent of myocardial ischemia can be evaluated using Myocardial Perfusion Imaging (MPI). The basic principle behind MPI is that when the myocardium is under stress, less blood is supplied to the myocardium, hence small amounts of the injected radionuclide is absorbed by the myocardium. Diagnosis is made by comparing images obtained during rest and those obtained during stress.

The challenge in interpreting Myocardial Perfusion Imaging is being able to associate the myocardial ischemia to a particular obstructive stenosis in a coronary artery. In practice MPI is interpreted by mapping the information into a 17-segment model called a bulls-eye plot, each one of this segment is associated to a particular coronary artery (see Figure 1.11. Using the standardized 17-segment model does not always correspond to the correct coronary artery, because the coronary anatomy is not the same across the population. Thus, there is a need to develop a patient specific model, by combining anatomical information obtained from CTA scans and the functional information from MPI scans.

1.5 Thesis outline

The work presented in this thesis belongs to the "*Heart in 3D*" project, a public-private collaboration between three universities (TU Delft, Erasmus MC and LUMC) and a consortium of companies (Medis Medical Imaging bv, Cardialysis bv, BioClinica, Oldelft Ultrasound). The general aim of the project was to develop novel algorithms and quantitative analysis tools on multimodal images, to support diagnosis and disease staging in CVD. The Heart in 3D project involved three PhD students (Rahil Shahzad, Hortense Kirişli and Vikas Gupta). Hortense Kirişli was mainly responsible for the development and evaluation of a 3D cardiac chamber segmentation method, the fusion of cardiac multi-modal images and the development of an evaluation framework for (semi-) automatic stenosis detection and quantification. Vikas Gupta was responsible for registration and segmentation methods in MR perfusion images, quantification in SPECT perfusion images, and selection of SPECT, CT/CTA, and CCA data for the validation of SMARTVis tool. The main focus of this thesis is to develop methods to automatically quantify the cardiovascular imaging biomarkers mentioned in the previous section, as well as to evaluate the accuracy of these methods in clinical practise. The main contribution of the author, Rahil Shahzad are the design, implementation and evaluation of: 1) an atlas based 'Coronary Density Estimate', 2) a pattern recognition based method for detecting and labelling coronary artery calcium lesions, 3) an atlas based method for quantification of epicardial fat volume 4) an automatic stenosis detection and quantification method by integrating and improving pre-existing methods such as a new calcium suppression step, 5) investigating the association of epicardial fat on 2370 subjects. Each of these contributions have been presented in separate chapters.

In Chapter 2 a new atlas based method is presented that enables us to estimate the locations of the coronary arteries on a cardiac CT scan. We call this feature 'Coronary Density Estimate'. It is derived by determining the anatomical variations of the coronary arteries from a random population of 85 subjects.

In Chapter 3 a method for automatic calcium scoring is presented. The method uses a pattern recognition approach in order to identify the true calcium objects from the image noise. The method also assigns the identified calcium objects to the corresponding artery using the 'Coronary Density Estimate' feature described in **Chapter 2**.

In Chapter 4 an atlas based segmentation approach for epicardial fat quantification is presented. The method uses CTA atlas images in order to segment the subject's pericardium on CT scans. The method has been evaluated by comparing the performance of the method with two manual observers.

In Chapter 5 we present a method for detection, quantification and segmentation of stenosis. The method is based on centerline extraction, lumen segmentation and a regression approach in order to estimate the healthy lumen diameter. The performance of the method was evaluated using the *Coronary Artery Stenosis Detection and Quantification Evaluation Framework*.

In Chapter 6 we present the Synchronized Multimodal heART Visualization (SMARTVis) system to integrate perfusion information from SPECT-MPI and the

coronary artery anatomy information from CTA. We investigated the additional diagnostic value of fused CTA/SPECT-MPI analysis as compared to side-by-side analysis, in patients with suspected coronary artery disease (CAD).

In Chapter 7 we investigate the association of epicardial fat volume with atherosclerosis at multiple locations and assessed its risk factors in a large sample of community-dwelling elderly. The epicardial fat volume was quantified automatically using the method describe in **Chapter 4**. 2370 subjects were included in the study, along with the epicardial fat volume, calcifications in the aorta, coronary and carotid arteries were also quantified.

In Chapter 8 we conclude the thesis by providing the summary and general discussion.

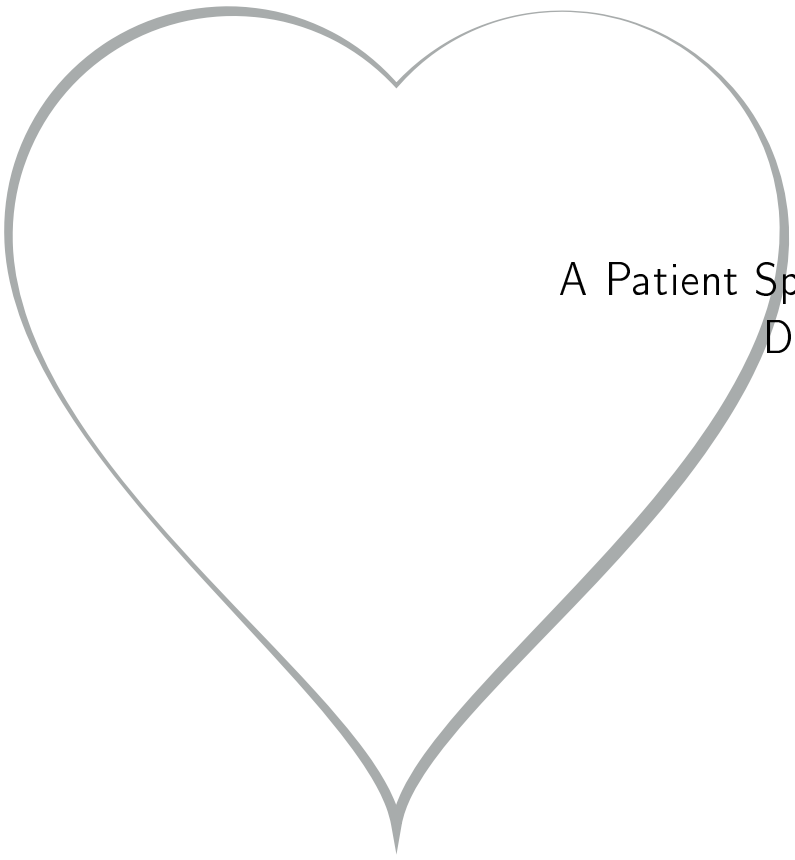

2

A Patient Specific Coronary Density Estimate

This chapter is based on the manuscript:
A Patient Specific Coronary Density Estimate,
R. Shahzad, M. Schaap, T. van Walsum, S. Klein, A.C. Weustink, L.J. van Vliet, and W.J. Niessen,
IEEE International Symposium on Biomedical Imaging: From Nano to Macro, 9–12, 2010.

Abstract

Purpose A reliable density estimate for the position of the coronary arteries in Computed Tomography (CT) data is beneficial for many coronary image processing applications, such as vessel tracking, lumen segmentations, and calcium scoring.

Methods We present a method for obtaining an estimate of the coronary artery location in CT and CT angiography (CTA). The proposed method constructs a patient-specific coronary density estimate using CTA atlas registration. The method is evaluated by quantifying the overlap of the obtained density estimate with 24 manually annotated centrelines of the lumen. Furthermore, the method is quantitatively evaluated when applied in automatic calcium scoring of the coronary arteries, which is an important risk predictor of coronary artery disease. The obtained results were compared to manual annotations on 170 CT datasets.

Results On the 24 CTA datasets it was observed that on average 82% of all the centerline points in the RCA, 91% of the LAD centerline points and 58% of the LCX centerline points lie within the respective patient-specific coronary artery density estimates. With respect to the calcium scores obtained on the 170 CT data using the density estimates, a Pearson's correlation coefficient R of 0.93 was obtained.

Conclusions We present a method that allows construction of patient-specific coronary artery estimates. The application of these estimates for the purpose of calcium scoring has been demonstrated.

2.1 Introduction

Cardiovascular disease (CVD) is the number one cause of death worldwide. It is estimated that by 2030 around 23.6 million people will die from CVD (WHO, 2012). Detection and quantification of atherosclerosis is essential for risk assessment of the coronary artery disease (CAD).

The imaging modalities of choice for non-invasive quantification of atherosclerosis in the coronary arteries are Computed Tomography (CT) and Computed Tomography Angiography (CTA). Obtaining a strong position estimate of the coronary arteries in CT and CTA data can be beneficial for several coronary image processing applications, such as vessel tracking, lumen segmentations, and the quantification of the amount of calcium, viz. Calcium Scoring (CS).

This chapter presents a method for obtaining a density estimate for the position of the main coronary arteries, namely: right coronary artery (RCA), left anterior ascending (LAD) and left circumflex (LCX), in CT and CTA data. The method is quantitatively evaluated on CT images by using the density estimate for automatic calcium scoring. Studies have shown that the amount of calcified plaque is directly related to further coronary related events and are also a predictor for CAD (Wayhs et al., 2002; Elkeles, 2008). A normal scanning protocol for the assessment of atherosclerosis consist of a low resolution non contrast-enhanced native CT scan and a high resolution contrast-enhanced CTA scan. The native scan is used for calcium scoring whereas the CTA scan is used to visualize the morphology of the coronary lumen and possibly neighbouring soft plaque.

The applicability of the method in CTA is evaluated by quantifying the overlap of the obtained density estimate with 24 manually annotated lumen centrelines. The method is evaluated quantitatively by comparing the results of automatic calcium scoring to manual annotations in 170 CT datasets.

In the remainder of this chapter we discuss the construction of the atlas density images and the application of these atlases for building patient-specific coronary density estimates. We conclude with the evaluation results of the proposed method on CTA and CT datasets.

2.2 Method

In an off-line stage, we build a number of CTA atlases with coronary density fields. The steps towards building these atlases, atlas selection, centreline mapping, density field generation and tuning the density fields inside the aorta, are detailed in section 2.2.1. The application specific details for using the density estimates for calcium scoring are described in Section 2.2.4.

2.2.1 Selection of atlases and density estimation

Atlas selection **-** From a training set of CTA datasets of 95 patients, a total of 10 CTA atlases were selected. We chose CTA datasets to build the atlases, because in CTA images the coronaries are clearly visible due to the presence of contrast agent. The

contrast within these images gives a clear depiction of the heart chambers and the main coronary vessels. The selection criteria for the atlases were based on the quality of the images (no blurring and minimal noise), the anatomy of the heart (shape and size) and field of view (large and small). The atlas images that were selected are shown in Figure 2.1.

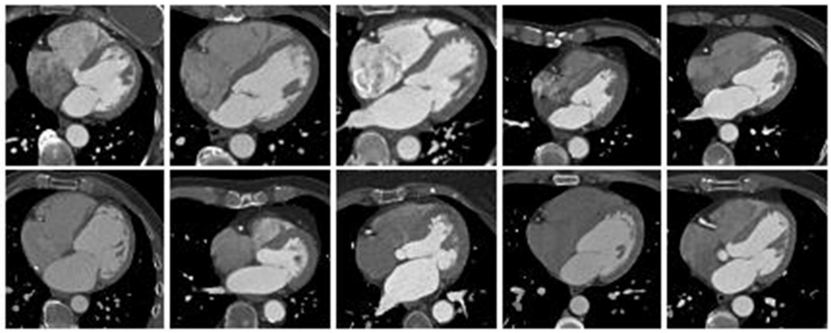

Figure 2.1: Axial slices of the 10 chosen atlases. The slices were selected approximately at the centre of the heart.

Centerline mapping **-** Lumen centrelines in the three main coronary arteries (RCA, LAD and LCX) were manually annotated in the remaining 85 CTA datasets (Figure 2.2). Each of the three manually annotated centrelines (85) were transformed to each of the CTA atlases (10). The transformations (85×10) were obtained by non-rigid registration of the atlases to the CTA images. The 85 CTA data sets were used as fixed images and the 10 atlases as the moving images. After the registration, each of the 10 atlases had 255 centrelines (85×3) mapped onto them.

Atlas centerline density estimation **-** The coronary density estimate for each voxel of the atlases was determined in the following way. First for every voxel, the closest point on each of the 85 centrelines for each of the three main arteries was determined. Subsequently, Mean Shift (Comaniciu and Meer, 2002) was applied to these points. The iterative Mean Shift algorithm is represented as:

$$\mathrm{x}^{\tau+1} = \sum_{m=1}^{M} \frac{G_\sigma(\left|\mathrm{x}^\tau - \mu_m\right|)}{\sum_{m'=1}^{M} G_\sigma(\left|\mathrm{x}^\tau - \mu_{m'}\right|)} \mu_m \ , \tag{2.1}$$

where μ_m represents the m^{th} data point, G_σ a Gaussian kernel with bandwidth σ and x^τ being the mean shifted position at iteration τ. As the stopping criteria we used $\mathrm{x}(^{\tau+1} - \mathrm{x}^\tau < \epsilon$. Once all the points had converged to their local mode, the shifted points were clustered based on their mode. In this way, the cluster for each point and the number of clusters was determined.

Next, for each of the clusters the covariance of the points in that mode was determined, and the density at the voxel of interest was calculated by summing

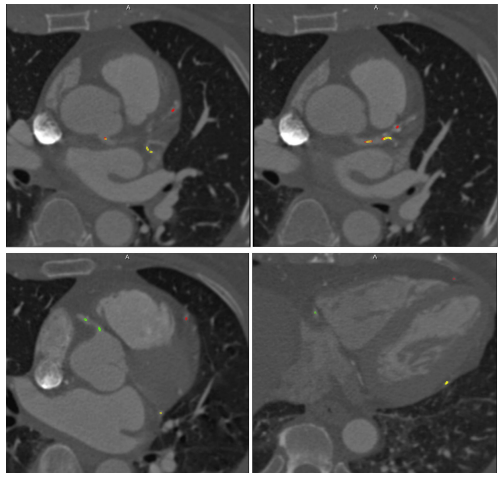

Figure 2.2: A Random CTA dataset with manually annotated centerlines. Different colors of the dots represent centerlines from different coronary arteries

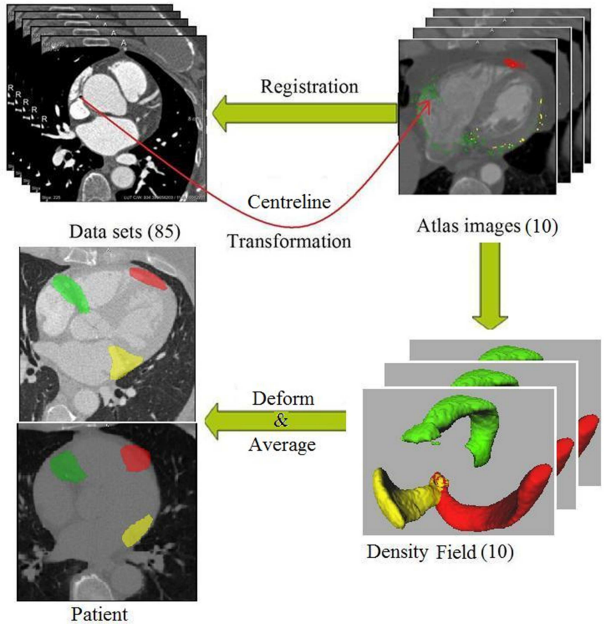

Figure 2.3: Schematic representation of the method. Top left: CTA data sets with manual centreline annotation. Top right: Atlas images with mapped centrelines for all 85 datasets. Bottom right: generation of the density field. Green, red and yellow represent the RCA, LAD and LCX respectively. Bottom left: using the density estimate on a patient CTA or CT image.

the contributions of each of the clusters, where each cluster is represented by a multivariate Gaussian:

$$d(x) = \sum_m P_m \frac{1}{(2\pi)^{N/2} \left|\Sigma_m\right|^{1/2}} \exp\left(-\frac{1}{2}(x - M_m)^T \Sigma_m^{-1} (x - M_m)\right) , \qquad (2.2)$$

with d(x) the density for position x, P_m the number of points in the mode m, N the dimension (in our case 3), Σ_m is the covariance matrix of all points in mode m and M_m the mean of the mode.

Finally, the obtained density estimates lying within the aorta were reset to zero. The aim of this work is to obtain an automatic density estimate for the location of the arteries. However, due to anatomical variations between patients, the locations of the start of the arteries at the aorta are not always the same. Furthermore, during annotation the observers did not start the annotation exactly at the coronary's ostium. This causes some of the mapped arteries to lie partly in the aorta of the atlas, thereby causing the density estimate to give a high value within the aorta. Therefore, we included a separate automatic aorta segmentation step in our off-line calculation of the density estimates, by updating the density field such that it is zero inside the aorta. The automatic aorta segmentation is based on a multi-atlas based registration approach, which is explained in detail in work of Kirişli et al. (Kirişli et al., 2010). The aorta is detected and segmented in all the 10 atlases and the density field is set to zero inside the segmented aorta region.

2.2.2 Patient specific coronary artery density estimation

In order to obtain a patient specific coronary artery density estimation, the density fields obtained from the atlases are mapped onto either a CTA or CT image. This is achieved by a non-rigid registration of the atlas images to the CT/CTA images, transforming the density fields accordingly, and combining the density fields by averaging them.

2.2.3 Implementation

All image registrations were performed using Elastix, a publicly available medical image registration software package (Klein et al., 2010). We used a multi-stage registration approach. Initially a multi-resolution coarse-to-fine affine registration was performed in three steps. For each resolution level we applied 256 iterations of a stochastic gradient descent optimizer (Klein et al., 2009). As cost function, the Mean Square Difference (MSD) was calculated using 1028 image samples randomly chosen in each iteration. The results of the affine registrations were used to initialize a B-spline registration. A four step coarse-to-fine strategy was used, with 1024 iterations of a stochastic gradient descent optimizer in each step. A B-spline grid was defined by control points with 20 mm separation. The Mutual Information (MI) cost function was calculated using 2048 randomly chosen image samples in each iteration.

For the centreline density estimation, the Approximate Nearest Neighbour (Arya et al., 1998) was used to determine the closest point on each centreline. To speed up the processing, voxels for which all centrelines further away than 10 mm received a density value of zero. In the Mean Shift clustering ϵ was set to 0.01 and the bandwidth for the Gaussian kernel G_σ was set to 1 mm. A small offset of 0.6 mm was added to the diagonal elements of the covariance matrix to guarantee invertability of this matrix. For the calcium score calculation, to avoid noise being detected as a false calcification, the connected components having a volume of less than 0.02 ml were removed.

2.2.4 Calcium scoring

In conventional calcium scoring, first candidate calcifications are selected by thresholding (130 HU) followed by manual removal of false positives.

For our fully automated implementation of the automatic calcium scoring, first a pre-processing step was performed on the CT images. Dense bony structures (ribs, sternum and vertebra) were identified as objects having an intensity above 130 HU and a volume exceeding 1 ml, the intensity of these objects were set to zero. This step was performed to make the method more robust. The density field failed (for one patient) to spatially differentiate the ribs lying very close to the coronaries (especially LAD), thus intersecting the density field. The pre-processing step helped in removing the rib being detected as coronary calcification.

Subsequently, a ROI was obtained for the vessels by averaging the density fields from the 10 atlases, a threshold value of 0.01 was used. This threshold value was empirically found by visual inspection on a separate set of CT datasets. Subsequently, the CT image was thresholded at 130 HU to obtain all the calcifications. Calcium scoring can be performed with several different methods. To evaluate the automatic calcium scoring method on the CT dataset we use the most widely used method, the Agatston score (Agatston et al., 1990). It is calculated as:

$$AS = \sum_{i=1}^{n} A_i w_i \ , \tag{2.3}$$

where i is object's slice number, A_i is the area of the lesion on the respective slice and w_i the weighting factor of the lesion on slice i. The value of w_i is defined by:

$$w = \begin{cases} 1 & 130HU \leq I_i < 200HU \\ 2 & 200HU \leq I_i < 300HU \\ 3 & 300HU \leq I_i < 400HU \\ 4 & 400HU \leq I_i. \end{cases} \tag{2.4}$$

where I_i is the maximum intensity value of the calcification.

The Agatston scores of all the calcifications are summed to obtain the final Agatston score. In the standardized Agatston score, CT images are resampled in the z-direction to produce a slice thickness of 3 mm.

2.3 Experiments

2.3.1 Data acquisition and manual annotations

All datasets used in this study were acquired at the Erasmus MC, Rotterdam, The Netherlands. The scans were acquired on two different CT scanners (Somatom Definition and Somatom Sensation, Siemens Medical Solutions, Forchheim, Germany). A tube voltage of 120 kV was used for both scanners. The CTA images were acquired with ECG dose pulsing (Weustink et al., 2008) and reconstructed with B30f (medium to smooth) or B46f (sharp) convolution kernels. The CTA datasets have an image dimension of approximately $512 \times 512 \times 350$ voxels and a voxel size of approximately $0.35 \times 0.35 \times 0.4$ mm^3. A total of 95 CTA images (10 atlas images and 85 centreline images) and 24 additional CTA images were used for the quantitative evaluation of our method. The manual annotation in the 85 CTA images for the density atlases and 24 CTA images for the quantitative evaluation was performed by trained observers. Details about the manual annotation can be found in (Schaap et al., 2009a).

A total of 170 CT datasets were used for the evaluation on CT data. The datasets have an image dimension of approximately $512 \times 512 \times 87$ voxels and a voxel size of approximately $0.35 \times 0.35 \times 1.5$ mm^3. The kernel used for constructing the CT images was B35f (medium smooth).

2.3.2 CTA evaluation - Centerline detection

The averaged density fields were used on a set of 24 CTA images with manually annotated centrelines to estimate the accuracy of the manual centrelines lying within the obtained field. Statistical analysis was performed on these data sets to determine whether centrelines lie in the field, by using a mask (by thresholding the density field) for the ROI and determine the percentage of centreline in the ROI (Figure 2.5). The results show that (average $\pm$ SD) $82 \pm 31\%$ of RCA, $92 \pm 18\%$ of LAD and $58 \pm 44\%$ of LCX lie within the computed density fields.

2.3.3 CT evaluation - Calcium scoring

The automatically obtained Agatston scores for the 170 CT datasets were compared to the manually obtained Agatston scores. The scores were found to be linearly related with a Pearson regression coefficient R of 0.93. A scatter plot of the manual versus the automatic scores is shown in Figure 2.4.

2.4 Discussion and conclusions

A method for automatically obtaining patient-specific coronary artery estimates in CTA and CT has been proposed. The results show that the density estimates provide a reasonable estimate for the locations of the main arteries in both CTA and CT images. These estimates can be used for various cardiac image processing applications e.g. fully automated calcium scoring as presented in this chapter.

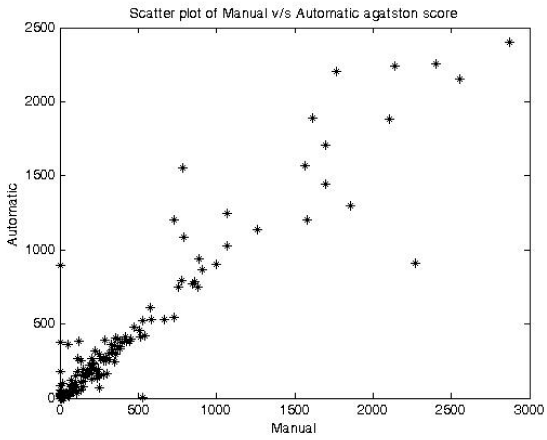

Figure 2.4: Scatter plot of the Manual versus the Automatic Agatston scores.

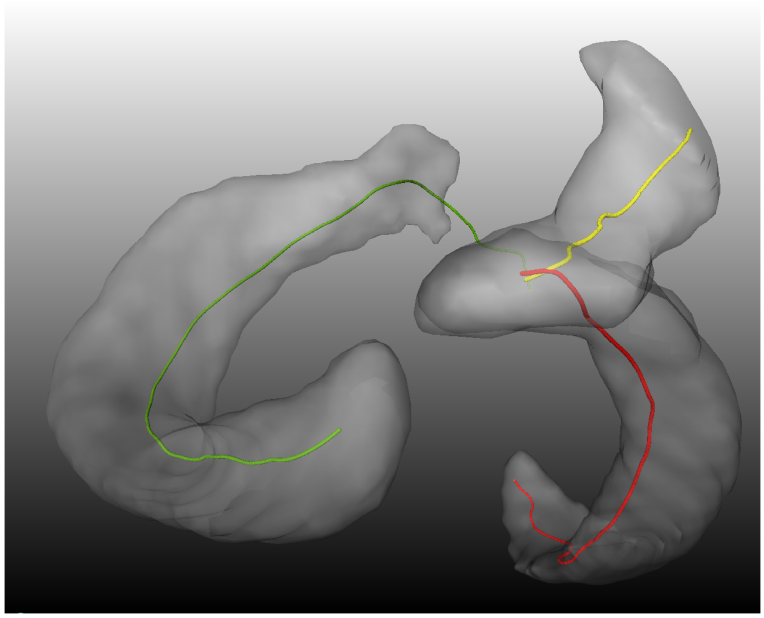

Figure 2.5: 3D image of the density fields with the manual centerline passing through it. Green: RCA, Red : LAD, Yellow: LCX

The calcium scoring results are currently still different from the manual quantification, but we believe the method can easily be made more accurate by incorporating a classification technique which could differentiate between a calcium spot and noise by using a appearance feature as presented in (Isğum et al., 2004).

The elegance of the method used for calcium scoring is that it is possible to derive calcium scores per vessel. Reporting the three calcium scores separately is expected to give better insights about the calcified plaque. Other methods that could be used to increase the accuracy of the calcium scoring method would be to use a wider set of atlases, covering more anatomical variations. The density fields can be improved by increasing the number of centrelines being mapped onto the atlases. The application to CTA showed a good overlap of the density estimates with manual annotations.

When inspecting the cases where the automated approach was not very accurate, often the registration of some of the atlases to the patient data had failed. We intend to address this issue by a further tuning of the registration, and by incorporating additional atlases and possibly an atlas selection scheme. We conclude that we presented a method that allows construction of a patient-specific coronary vessel estimate, and showed the application of this estimate in calcium scoring.

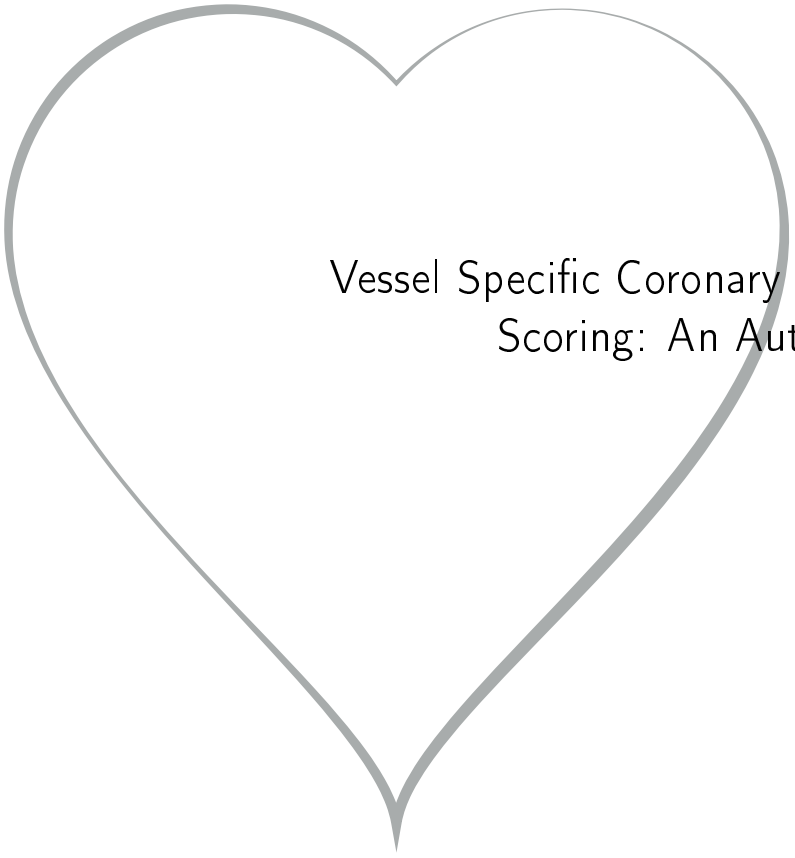

3

Vessel Specific Coronary Artery Calcium Scoring: An Automatic System

This chapter is based on the manuscript:
Vessel Specific Coronary Artery Calcium Scoring: An Automatic System,
R. Shahzad, T. van Walsum, M. Schaap, A. Rossi, S. Klein, A.C. Weustink, P.J. de Feyter, L. van Vliet and W.J. Niessen, *Academic Radiology*, 20(1):1–9, 2013.

Abstract

Purpose The aim of this study is to automatically detect and quantify calcium lesions for the whole heart as well as per coronary artery on non-contrast-enhanced cardiac computed tomographic images.

Methods Imaging data from 366 patients were randomly selected from patients who underwent computed tomographic calcium scoring assessments between July 2004 and May 2009 at Erasmum MC, Rotterdam. These data included data sets with 1.5 mm and 3.0 mm slice spacing reconstructions and were acquired using four different scanners. The scores of manual observers, who annotated the data using commercially available software, served as ground truth. An automatic method for detecting and quantifying calcifications for each of the four main coronary arteries and the whole heart was trained on 209 data sets and tested on 157 data sets. Statistical testing included determining Pearson's correlation coefficients and Bland-Altman analysis to compare performance between the system and ground truth. Wilcoxon's signed rank test was used to compare the interobserver variability to the system's performance.

Results Automatic detection of calcified objects was achieved with sensitivity of 81.2% per calcified object in the 1.5 mm data set and sensitivity of 86.6% per calcified object in the 3.0 mm data set. The system made an average of 2.5 errors per patient in the 1.5 mm data set and 2.2 errors in the 3.0 mm data set. Pearson's correlation coefficients of 0.97 ($P < .001$) for both 1.5 mm and 3.0 mm scans with respect to the calcium volume score of the whole heart were found. The average R values over Agatston, mass, and volume scores for each of the arteries (left circumflex coronary artery, right coronary artery, and left main + left anterior descending coronary arteries) were 0.93, 0.96, and 0.99, respectively, for the 1.5 mm scans. Similarly, for 3.0 mm scans, R values were 0.94, 0.94, and 0.99, respectively. Risk category assignment was correct in 95% and 89% of the data sets in the 1.5 mm and 3 mm scans.

Conclusions An automatic vessel-specific coronary artery calcium scoring system was developed, and its feasibility for calcium scoring in individual vessels and risk category classification has been demonstrated.

3.1 Introduction

Coronary artery disease (CAD) is one of the leading causes of mortality worldwide (WHO, 2012). Many clinical studies have shown that the amount of calcium in coronary artery plaques correlates with the risk of future cardiovascular events (Budoff and Gul, 2008; Kondos et al., 2003; Raggi, 2002; Vliegenthart et al., 2005; Elias-Smale et al., 2010; Detrano et al., 2008).

Calcium scoring is routinely performed on low-dose, non contrast-enhanced computed tomography (CT) scans by manually annotating all calcium objects present in the main vessels of the coronary artery tree viz. left main (LM), left circumflex (LCX), left anterior descending (LAD) and right coronary artery (RCA). Subsequently, based on all selected objects per patient, the Agatston (Agatston et al., 1990), mass (Callister et al., 1998) or volume (Hong et al., 2002) scores are determined. Recently, it has been suggested that vessel-specific calcium scoring or rather risk assessment based on individual vessels is more informative compared to whole heart calcium scoring (Qian et al., 2010). Similar findings were reported in other large population studies, Williams et al. (Williams et al., 2008) observed that the mortality rate of the patients they followed increased proportionally with the rise in the number of calcified lesions and they also observed that all the patients who had an Agatston score of ≥ 1000 in the LM died during the follow up. Mohlenkamp et al. (Möhlenkamp et al., 2003) observed that LM disease was an independent predictor of hard events. Vessel-specific scores also facilitate in better understanding calcium progression in longitudinal studies. Budoff et al. (Budoff et al., 2007) found that calcium approximately increases by 20%–30% each year. The MESA study (Rosen et al., 2009) investigated the relationship between calcium scores at baseline and stenosis in individual vessels. They reported a positive correlation between calcium scores and vessel-specific scores in the individual artery beds.

Manual scoring is a time consuming task because it consists of drawing contours to obtain the region of interest or clicking inside all calcium objects. Isgum et al. (Isğum et al., 2004) have demonstrated the feasibility of automating this task, but the feasibility of automatic per-vessel calcium scoring has not been demonstrated yet.

The purpose of our work is to develop and evaluate an automatic calcium scoring system for ECG gated, non contrast-enhanced cardiac CT scans that yields scores for the whole heart as well as for the individual coronary arteries. Our system uses an atlas based estimate of the coronary artery locations, which permits the system to assign calcium lesions to the correct coronary arteries (Shahzad et al., 2010), which has been explained in more detail in **Chapter 2**. The system uses a machine learning approach to discriminate true calcium objects from all detected candidate objects.

3.2 Materials and methods

3.2.1 Data description

We retrospectively selected a random subset of patients who underwent a cardiac non contrast-enhanced CT scan for calcium score evaluation between July 2004 and May

2009 at the Erasmus MC, and for whom the calcium scoring reports were electronically available along with the scans in the picture archiving and communication system (PACS). In total 366 scans (280 male and 86 female) were retrieved. The scans were acquired on four different generations of Siemens scanners (Definition Flash, Definition AS+, Sensation 64 and Definition, Siemens Medical Solutions, Forchheim, Germany). A detailed description of the data characteristics is provided in Table 3.1. A tube voltage of 120 kV was used for all scans. Two different slice spacings were used in tomographic reconstruction: 234 scans have 1.5 mm slice spacing and 132 scans have 3.0 mm slice spacing, henceforth referred to as the 1.5 mm and 3.0 mm scans respectively. Both types of scans have a slice thickness of 3.0 mm and a field of view (FOV) of approximately 180 mm. The in-plane resolution was 0.35×0.35 mm^2 on average. Both the 1.5 mm and 3.0 mm scans were randomly divided into different sets for designing, training, and testing of the calcium scoring system, as shown in Figure 3.1. The age distribution of male and female patients over the datasets was similar.

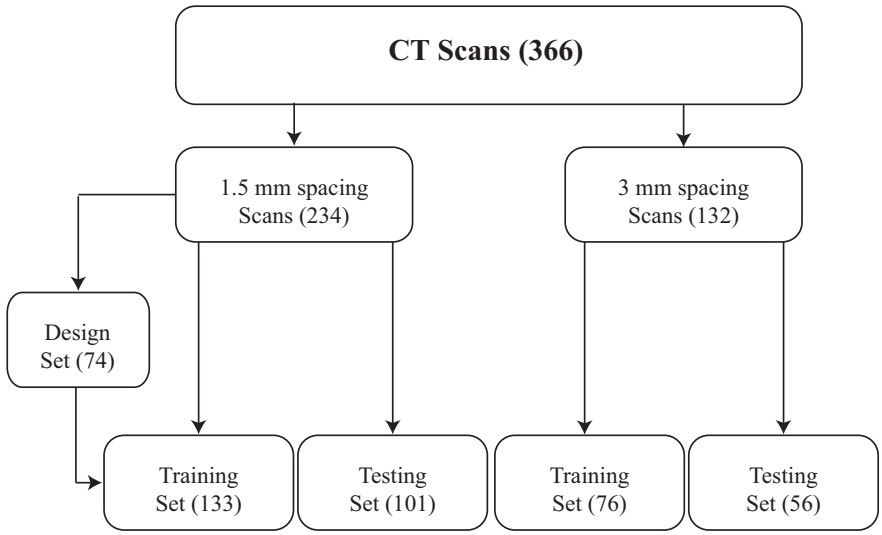

Figure 3.1: Schematic diagram showing the distribution of data sets used for designing, training, and testing of the calcium scoring system.

3.2.2 System overview

The complete calcium scoring system consists of the following stages. First, candidate calcium objects are determined from the CT scan. Subsequently, a classifier that uses local image features is applied to determine which of the detected candidate

Table 3.1: Details of the Data Sets. Data are expressed as number (percentage) or as mean (range).

Variable	Value
Data Sets	
Total	366
Women	86 (23.5%)
Men	280 (76.5%)
Age, women (y)	57 (28-83)
Age, men (y)	57 (21-84)
Scanner type	
Definition (3.0 mm scans)	132 (36.1%)
Sensation 64	205 (56%)
Definition Flash	16 (4.4%)
Definition AS+	13 (3.5%)

objects are coronary artery calcifications. Finally, a coronary artery location estimate is being used to assign the calcifications to one of the main coronary arteries. These calcifications are used to compute the calcium scores. The following paragraphs describe the candidate detection, the design of the classifier, including how it was trained and which features are being used, and how the final calcium scores are computed and presented. The workflow of our system including the calcified object labelling is shown in Figure 3.2.

3.2.3 Candidate detection

Candidate calcium objects were obtained from the CT scans by thresholding at 130 HU and discarding all objects with a size larger than 1500 mm^3 and also those smaller than 1.5 mm^3 which are assumed to correspond to bone and noise respectively (Callister et al., 1998). The candidate objects consist of true calcified objects, including arterial calcifications, aortic calcifications as well as calcifications in the valves and false objects due to noise and imaging artefacts.

3.2.4 Classifier

We develop a classifier for the candidate objects that differentiates between arterial calcium and the rest, based on local image information (features). The classifier is trained using manually annotated CT data (the training set). We used the design set to experimentally determine the optimal classifier and feature set. The image features that were investigated, classifier selection and feature selection are presented in the sections below. We built and trained two classifiers, one for the 1.5 mm data and one for 3.0 mm data. The 1.5 mm training data had a total of 366,876 candidate calcium objects out of which 1155 were true calcium objects. The 3.0 mm training

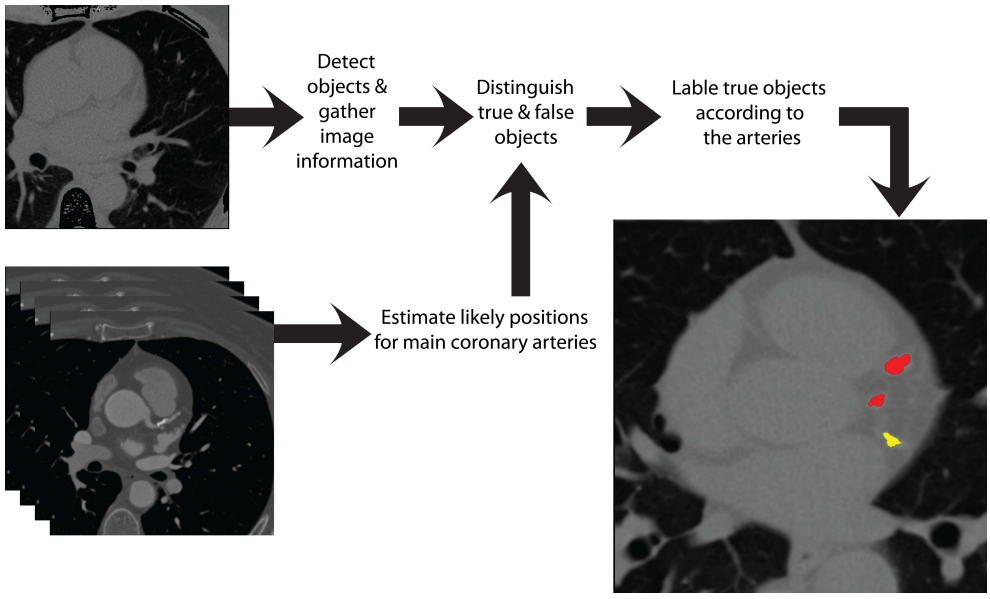

Figure 3.2: An illustration showing the work flow of the system. (Top left) Non-contrast enhanced computed tomographic (CT) image of a patient that needs to be analysed. (Bottom left) Ten contrast-enhanced CT angiographic images used as atlases to compute the coronary artery position estimate features. Using a registration step, the CT angiographic atlas features are mapped onto the CT image. The detected calcium objects are then labelled using the position estimates as shown by the image on the right (red objects are assigned to the left anterior descending coronary artery and the yellow object to the left circumflex coronary artery).

data had a total of 112,302 candidate calcium objects out of which 439 were true calcium objects. The system automatically determines the slice spacing of the dataset to be analysed and applies the appropriate classifier.

3.2.5 Features

A feature based classification (Theodoridis S, 2009) approach was adopted for classifying candidate objects. In total 62 features were considered which are listed in Table 3.2, and explained below.

Object based features - Five different types of object based features were computed: volume of the candidate object, maximum and average intensity of the object, and two shape features, blob likeness and plate likeness (Frangi et al., 1998).

Multi scale image derivatives - The intensity of the object at the maximum intensity point after Gaussian image derivatives were computed at five different scales (Gaussian standard deviation in-slice between 0.3 mm to 4.8 mm with one sample per octave; between slices from 1.5 mm to 24 mm with one sample per octave) up to the second order.

Coronary artery location estimate - An atlas based method (Pham et al., 2000) was used to determine a location estimate for the coronary artery locations. Coronary artery locations from 85 different CT Angiographic (CTA) scans were used to build ten atlases encoding the distribution of coronary arteries across the population. These atlases were registered to the CT scan to obtain the patient-specific coronary artery location estimate for each individual artery. The selection criteria of the 10 atlas scans and the exact procedure to compute the artery location estimates are described in detail in **Chapter 2.** (Shahzad et al., 2010). The artery location feature is used both for the classification of candidate objects and for the calculation of calcium score per artery.

Position based features - Positions (x, y, z) in actual image space and in a standardized coordinate space were used. We introduced the standardized space to account for the varying position of the heart in CT scans. This standardized space is constructed by pair-wise registration of 10 atlas images (the same ten atlases that were used for creating the coronary artery location estimates). Registration was performed in two stages: an initial affine registration followed by a non-rigid registration using ElastiX, a publicly available registration package (Klein et al., 2010). The standardized space is then obtained by averaging the resulting deformations. The midpoint between the right and left coronary ostium is defined as the origin in the standardized space. A CT scan of a new patient is mapped into this standardized space, such that relative positions in this standardized coordinate system can be used.

Table 3.2: Feature Description.

Feature Description	**Number of features**
Volume of object mm^3	1
Intensity of object: maximum and average	2
Position: x, y and z cordinates in image space and mean space	6
Intensity of voxel at the maximum intensity point after gaussian filtering at five different scales	5
Intensity of voxel at the maximum intensity point after first-order gaussian derivatives in x, y and z directions at five different scales	15
Intensity of voxel at the maximum intensity point after second-order gaussian derivatives in xx, yy, zz, xy, yz and zx directions at five different scales	30
Coronary artery position likelihood estimate	1
Shape	2

3.2.6 Feature selection and classifier selection

On the design set, feature selection was performed to determine the set of features that gives optimal performance in detecting calcified objects in the coronary arteries. In our case, since the training set is limited (on average, there were only seven calcium objects per dataset), it is also important to reduce the number of features to avoid the curse of dimensionality i.e. having too few training samples in a high dimensional feature space (Theodoridis S, 2009). Twenty one features were selected based on a forward feature selection step. We also applied a backward feature selection algorithm and observed that the selected feature set was identical.

We investigated the performance of the k-NN (k-Nearest Neighbour) classifier for different number of neighbours k ranging from 1-15 (odd values), with forward feature selection. We found that the best classifier for this problem is a 9-NN classifier, as this classifier yielded the smallest classification error at the object level.

The set of 21 best features retained were: volume, maximum and average intensity, position-z in the image and mean space, coronary artery position estimate, Gaussian filter with scale 1, 2, 4 and 8, 1st order Gaussian derivative with scale 1, 8 and 16 in z direction. 2nd order Gaussian derivative; with scale 1, 2 and 4 in the x direction and also same scales in the y direction, z direction with scale 1 and 2. The unit of the scale is 0.3 mm in the x and y direction and 1.5 mm in the z direction (corresponding to size of a voxel in the 1.5 mm dataset).

3.2.7 Calcium scores

The system calculates Agatston, mass and volume scores for the detected calcium objects (Ohnesorge et al., 2000). The system presents the scores for the whole heart as well as the individual arteries. The assignment of the calcium object to one of the arteries is achieved by using the coronary artery location estimate feature. Since we use population based information from the atlases to compute the location estimates of the coronary arteries and owing to the large anatomical variation in the length of the LM artery we decided to label LM and LAD as one single vessel. The other two vessels are labelled as LCX and RCA.

3.2.8 Risk categorization

Patients are assigned to different risk categories based on the whole heart Agatston scores (Oudkerk et al., 2008; Polonsky et al., 2010). Hoff et al. studied the distribution of calcium lesions on 35,246 patients with respect to age and gender and showed that the calcium score distribution depends on the age and sex of the patient. They proposed to present calcium scores as 10th, 25th, 50th, 75th and 90th percentile rank groups (Hoff et al., 2001). Our system assigns the patients to the appropriate risk category using this method, hence accounting for age and sex.

3.2.9 Reference standard

The reference standard calcium scores were obtained from the calcium scoring reports that were stored in the PACS along with the patient scans. Calcium scoring for

generating the reports was performed manually using the Syngo Calcium Scoring tool (Siemens Medical Solutions, Forchheim, Germany). We reproduced the set of calcium objects in the scans using the reports.

3.2.10 Statistical analysis

We report the system's sensitivity and specificity with respect to object detection. To evaluate the scores per patient, the Pearson correlation coefficient (R) was calculated and Bland-Altman plots (Martin Bland and Altman, 1986) were created for the entire heart as well as for individual arteries. The analysis was performed using MATLAB 7.9.0. (Natick, Massachusetts). A confusion matrix was used to report errors in automatic risk categorization from the whole heart calcium scores. The accuracy of the automatic method for calcium scoring was compared to inter-observer variability on a subset of 50 patients; differences in total calcium scores (for Agatston, mass, and volume scores) were analyzed by Wilcoxon signed rank test for which we report the Z-statistic value to indicate the significance.

3.3 Results

3.3.1 Overall performance of the system for calcium object detection

1.5 mm scans **-** The system was tested on 101 datasets comprising 281,138 candidate objects out of which 787 were true calcium objects. The system yields a per object sensitivity of 81.2% and a specificity of 99.6%.
3 mm scans **-** The system was tested on 56 datasets comprising 64,555 candidate objects out of which 300 were true calcium objects. The system has a per object sensitivity of 86.7% and a specificity of 97.4%.

3.3.2 Performance of the system on the patient calcium scores

1.5 mm scans **-** On average the system made 1 false positive error and 1.5 false negative errors per patient. We obtained a Pearson correlation $R = 0.97$, 0.95 and 0.97 ($P < 0.001$) between automatic and manual scoring on the whole heart with respect to the Agatston, mass and volume scores. The corresponding correlation coefficients for each of the arteries are shown in Table 3.3. Out of the 101 patients, five were assigned to a different risk category; Two of them were off by two categories while the others were off by one category. Note that cases close to a boundary can easily move to the neighbouring category. The confusion matrix is shown in Table 3.4; 95% of the scans were assigned to the correct risk percentile.
3 mm scans **-** On average the system made 1.5 false positive errors and 0.7 false negative errors per patient. The correlation coefficients between automatic and manual scoring with respect to the Agatston, mass and volume scores were all equal to $R = 0.96$ ($P < 0.001$). The corresponding correlation coefficients for each of the arteries are shown in Table 3.3. Out of the 56 patients, six were assigned to the wrong risk category; Only one scan was off by two categories. The confusion matrix is shown in Table 3.4; 89.3% of the scans were assigned to the correct risk percentile.

The whole heart volume score correlations between the system and the manual observers are presented in Figure 3.3 along with the explanation of the few classification errors. The vessel-specific correlation curves on the 1.5 mm datasets are shown in Figure 3.4, the corresponding correlation values for the 3.0 mm scans are presented in Table 3.3. A few examples of misclassified objects are shown in Figure 3.5.

Table 3.3: Results of Bland-Altman Analysis of Agatston, Mass, and Volume scores for the Individual Arteries and Correlation between Automatic and Manual Scores for Each of the Arteries after Discarding the Outliers (as Depicted in Figure 3.4).

Calcium Quantification (score)	**Bias**	**95% Limits of Agreement**	**Correlation (R)**
	3.0 mm scans		
LCX			
Agatston	14	-93 to 122	0.94
Mass	3	-18 to 24	0.94
Volume (mm^3)	10	-84 to 104	0.93
RCA			
Agatston	-14	-211 to 184	0.93
Mass	-3	-45 to 39	0.94
Volume (mm^3)	-14	-272 to 143	0.93
LM+ LAD			
Agatston	11	-56 to 78	0.99
Mass	3	-12 to 17	0.99
Volume (mm^3)	1	-41 to 39	0.99
	1.5 mm scans		
LCX			
Agatston	-8	-243 to 227	0.96
Mass	-2	-60 to 56	0.93
Volume (mm^3)	-6	-187 to 175	0.96
RCA			
Agatston	-4	-175 to 167	0.98
Mass	-1	-43 to 42	0.96
Volume (mm^3)	-4	-137 to 128	0.98
LM + LAD			
Agatston	-5	-113 to 103	0.99
Mass	-1	-23 to 21	0.99
Volume (mm^3)	-6	-89 to 77	0.99

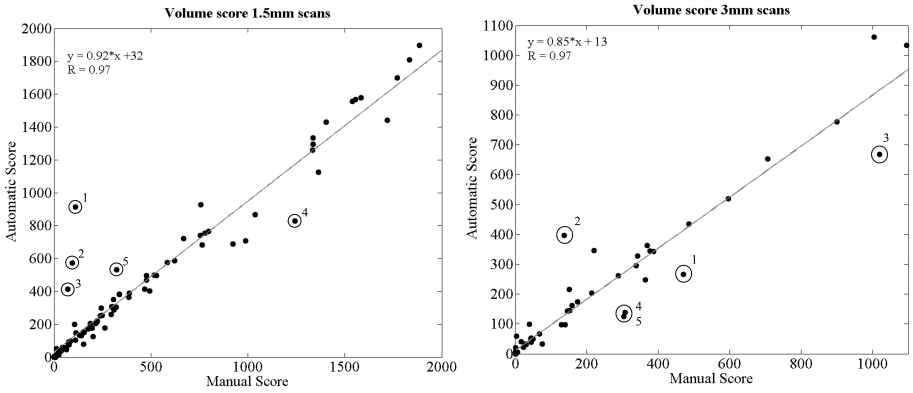

(a) (b)

Figure 3.3: Scatter plot of calcium volume obtained with automatic and manual methods. The largest errors are labelled and described below. (a) For 1.5 mm scans, (1) and (3) denote calcified mitral valves that were mistaken for calcium in the left circumflex coronary artery (LCX), (2) denotes an aortic calcification at the ostium which was mistaken for calcium in the right coronary artery (RCA), (4) denotes a calcium object at the distal part of the RCA that was missed, and (5) denotes an aortic calcification at the ostium that was mistaken for calcium in the left main coronary artery (LM). (b) For 3.0 mm scans, (1) a few calcium objects in the RCA were missed, (2) a calcified mitral valve was mistaken for calcium in the LCX, (3) a calcified object in the distal part of the RCA was missed, and (4) and (5) indicate a few objects that were missed in the LCX.

3.3.3 Method performance on left dominant and balanced subjects

We performed an additional experiment to estimate the mislabelling errors made by our method when quantifying calcium in left dominant and balanced subjects. We randomly selected 100 subjects from our dataset and selected all the calcium objects that are in the region that could possibly be supplied by the three different side branches resulting from the different dominant systems. We could accurately regionalize this area by using information from our standardized coordinate space. We found 26 calcium lesions belonging to 20 subjects in this region, the total volume of the lesions was found out to be 687.7 mm^3. Using the knowledge that on average 13% of a population is not right dominant (Cademartiri et al., 2008), and assuming a similar distribution over our subjects, we would make a total of 3.3 mislabelling errors over the 100 subjects. The average mislabelling error made was 0.26 objects and the volumetric error per left or balanced subject would thus be 6.8 mm^3, which is negligible compared to the average volumetric calcium score present in the main branch.

3.3.4 Inter-observer variability

The correlation coefficients R between the observers was 0.98 for all three scoring methods, for the automatic method with respect to each of the observers the mean value of R for the three scores was 0.97 and 0.95 (P<0.001). Table 3.5 describes the Median values, Z-statistic value (based on the Wilcoxon signed ranks test) and the Bland-Altman limits of agreement. From the Z-statistics it can be observed that the system does not make a statistically significant error compared to each of the observer.

Table 3.4: Confusion Matrix for Assigning a Risk Percentile by the Automatic and Manual Scores for 3.0 mm and 1.5 mm Scans.

3.0 mm Slice spacing Scans					
Automatic\Manual	10%	25%	50%	75%	90%
10%	**17**	0	0	0	0
25%	1	**5**	0	0	0
50%	1	0	**9**	1	0
75%	0	0	1	**8**	1
90%	0	0	0	1	**11**
1.5 mm Slice spacing Scans					
Automatic\Manual	10%	25%	50%	75%	90%
10%	**15**	0	0	0	0
25%	0	**13**	0	0	0
50%	1	0	**22**	1	0
75%	0	1	1	**22**	0
90%	0	0	0	1	**24**

3.4 Discussion

Our automatic system obtained a good sensitivity and a high specificity in detecting calcified objects. We also found that the agreement between the automatic and manual scores is very close to the inter observer agreement. Isgum et al. (Isğum et al., 2004) reported a sensitivity of 73.8% with respect to object detection, obtained by automatic whole heart calcium scoring on a cohort of only female patients, which where sampled to obtain a slice spacing of 3.0 mm. This sensitivity is less than the sensitivity obtained by our system which is 83.9% on the entire dataset. When we compare the results of only female patients from our test set (42 in total), we obtain a sensitivity of 82.2%.

The main advantage of our method is the automatic artery specific calcium scoring, permitting large scale epidemiology or long term prognostic evaluation studies (Budoff et al., 2007; Rosen et al., 2009) to better investigate the value of individual artery calcium scoring as a risk predictor (Qian et al., 2010).

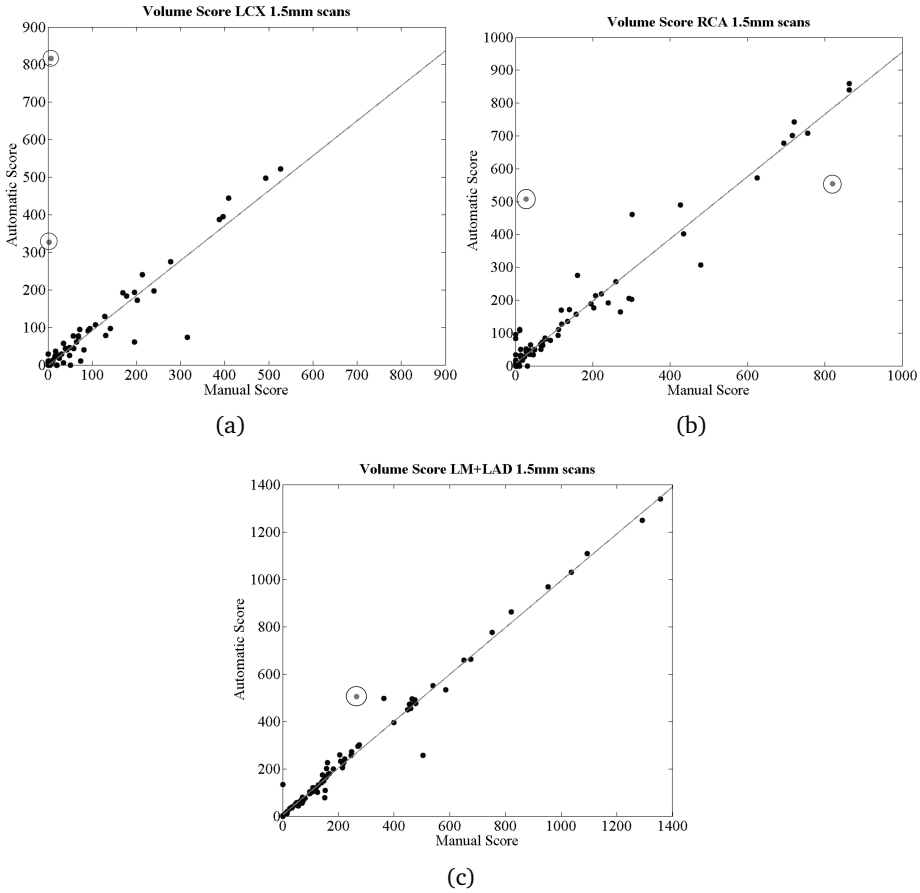

Figure 3.4: Scatter plot of automatic and manual volume scores for each of the arteries on the 1.5-mm scans: (a) left circumflex coronary artery (LCX), (b) right coronary artery (RCA), and (c) left main coronary artery (LM) and left anterior descending coronary artery (LAD). We discarded five outliers (circled) in computing the correlation for assessing the accuracy of the automatic vessel labelling.

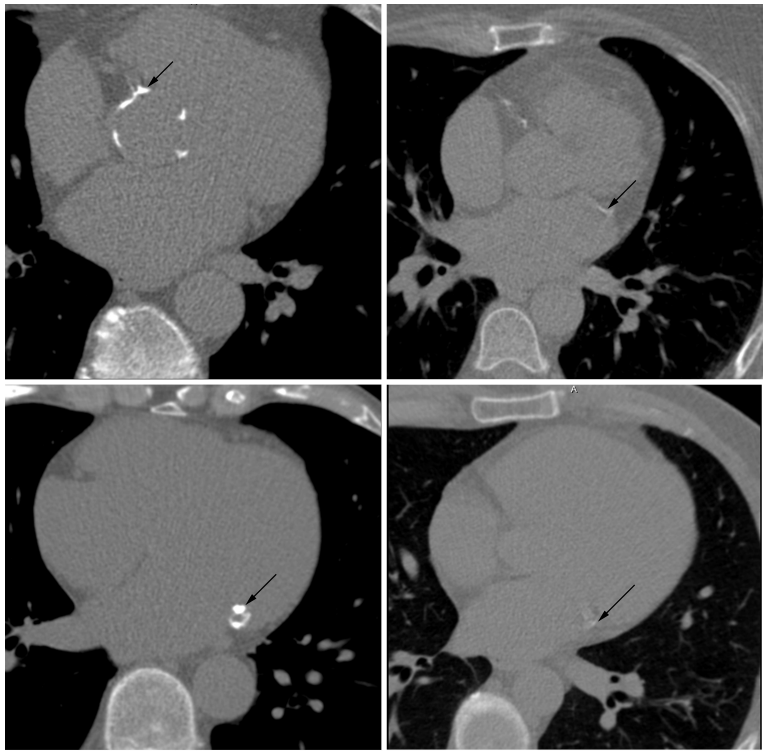

Figure 3.5: Axial slices showing cases in which the automatic method misclassified calcium objects: false-positives (left) and false-negatives (right). (Top left) A 1.5 mm scan from an 84-year-old man with an aortic calcification at the ostium. (Bottom left) A 1.5 mm scan from a 57-year-old man with a calcified valve. (Top right) A 3.0 mm scan from a 46-year-old woman with a lesion in the left circumflex coronary artery (LCX). (Bottom right) A 3.0 mm scan from a 50 year-old man with a lesion in the LCX very close to the mitral valve.

The atlases used for estimating in which coronary artery calcifications are located, were derived from a random population of 85 subjects. We calculated the overall spatial distribution of the individual coronary arteries and their branches over this population. Thus we do not differentiate between left-dominant and right-dominant subjects. Since the majority of the subjects in a given population are right dominant (Cademartiri et al., 2008), our atlases will label the posterior descending artery (PDA) as belonging to the RCA. This mislabelling of the vessels for the left dominant and balanced subjects does have a negligible effect on the correlation graphs between the automatic method and the ground truth, due to the small size of the calcium lesions found in the smaller vessels. Hence we conclude that mislabelling error in the left and balanced subjects by our method will not have a huge impact on vessel specific calcium scoring.

The automatic artery specific scores generated by our system correlate very well with those obtained manually. The bias, obtained from the Bland-Altman analysis, suggests that the system slightly underestimates the scores on 1.5 mm scans while the scores are slightly overestimated on 3.0 mm scans. Most errors in the vessel labelling were caused by incorrect object classification. The exceptions are some errors in the LM and the proximal part of the LAD. Variability in LM and LAD anatomy hampers the use of global information for separating the LM from the LAD, which is why we present the scores for LM and LAD combined. The correlation coefficients for respectively LM and LAD are 0.83 and 0.98 on 1.5 mm scans and 0.57 and 0.97 on 3.0 mm scans. The errors made while distinguishing the LM from LAD can be resolved if we would use image information from a corresponding contrast enhanced CT scan of the same patient, where the arteries are clearly distinguishable. However, in our study we assume that only non contrast-enhanced CT scans are available. Even though our system made two errors per patient, this did not have adverse effects in categorizing the patients into risk percentiles; only three patients were assigned to a risk percentile which was off by two categories. Also, there were 27 patients in total who had a zero calcium score. Our system correctly assigned a zero score to 18 patients, and the average error made in the remaining scans was a score of 2.8 (Agatston). None of these 27 patients were assigned to a different risk percentile.

The system is completely automatic. It can automatically provide the calcium scores when viewing the image, provided that the reconstruction phase of the scan was completed. The user may want to glance through the scan and correct for the misclassified objects which on average is limited to two objects per scan. The process of correcting the false positives, which generally occur around the aorta and the mitral valve, can be made easier by assigning a separate colour to the suspicious objects.

A limitation of our study is that the patient scans were acquired on equipment from only one vendor, Siemens. We did not investigate the performance of our system with data acquired using scanners from other vendors. However, as our method learns from example datasets we presume it can be adapted to data from other vendors or protocols, provided that a set of training data is available for the learning step.

3.5 Conclusions

We developed an automatic vessel-specific coronary artery calcium scoring system and demonstrated the feasibility of calcium scoring and risk category classification using this system.

Table 3.5: Coronary artery calcium score of the system and the observers O1 and O2 (Median); Pearson correlation coefficient (R), Z-statistic value using the Wilcoxon signed ranks test (Z) and the Bland-Altman limits of agreement for the inter observer and the system with respect to the observers(B-A). *P<0.001

	Median (range)			**R***			**Z Statistics**			**Bland-Altman**		
Score	*A*	*O1*	*O2*	*Inter-O*	*A-O1*	*A-O2*	*Inter-O*	*A-O1*	*A-O2*	*Inter-O*	*A-O1*	*A-O2*
Volume	204(0–1700)	214(0–1769)	224(0–1727)	0.98	0.97	0.95	-4.4	-1.7	-2.1	-157–145	-220–198	-247–217
Mass	38(0–378)	39(0–389)	41(0–382)	0.98	0.96	0.94	-3.9	-1.0	-1.8	-36–37	-48–49	-59–58
Agatston	216(0–2117)	215(0–2177)	217(0–2136)	0.98	0.97	0.96	-3.5	-1.2	-1.7	-194–202	-243–237	-274–277

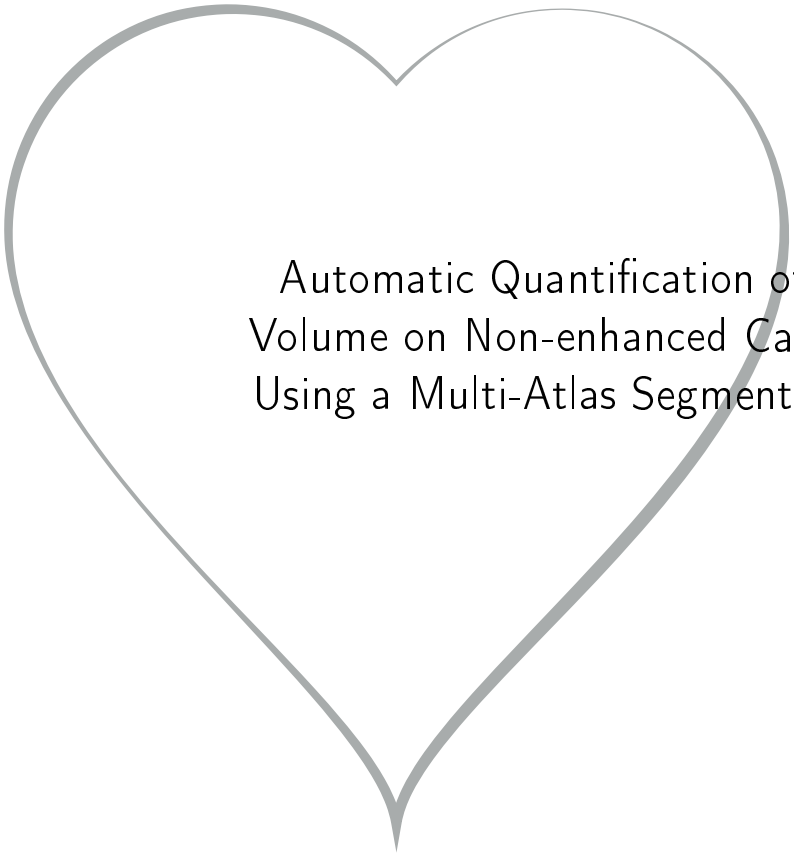

4

Automatic Quantification of Epicardial Fat Volume on Non-enhanced Cardiac CT Scans Using a Multi-Atlas Segmentation Approach

This chapter is based on the manuscript:
Automatic Quantification of Epicardial Fat Volume on Non-enhanced Cardiac CT Scans Using a Multi-Atlas Segmentation Approach,
R. Shahzad, D. Bos, C. Metz, A. Rossi, H.A. Kirişli, A. van der Lugt, S. Klein, J.C. Witteman, P.J. de Feyter, W.J. Niessen, L. van Vliet and T. van Walsum, *Medical Physics*, 40(9):*in press*, 2013.

Abstract

Purpose There is increasing evidence that epicardial fat (i.e. adipose tissue contained within the pericardium) plays an important role in the development of cardiovascular disease. Obtaining the epicardial fat volume from routinely performed non-enhanced cardiac CT scans is therefore of clinical interest. The purpose of this work is to investigate the feasibility of automatic pericardium segmentation and subsequent quantification of epicardial fat on non-enhanced cardiac CT scans.

Methods Imaging data of 98 randomly selected subjects belonging to a larger cohort of subjects who underwent a cardiac CT scan at our medical center were retrieved. The data were acquired on two different scanners. Automatic multi-atlas based method for segmenting the pericardium and calculating the epicardial fat volume has been developed. The performance of the method was assessed by 1) comparing the automatically segmented pericardium to a manually annotated reference standard, 2) comparing the automatically obtained epicardial fat volumes to those obtained manually, and 3) comparing the accuracy of the automatic results to the inter-observer variability.

Results Automatic segmentation of the pericardium was achieved with a Dice similarity index of 89.1 ± 2.6% with respect to Observer 1 and 89.2 ± 1.9% with respect to Observer 2. The correlation between the automatic method and the manual observers with respect to the epicardial fat volume computed as the Pearson's correlation coefficient (R) was 0.91 ($P< 0.001$) for both observers. The inter-observer study resulted in a Dice similarity index of 89.0 ± 2.4% for segmenting the pericardium and a Pearson's correlation coefficient of 0.92 ($P<0.001$) for computation of the epicardial fat volume.

Conclusions We developed a fully automatic method that is capable of segmenting the pericardium and quantifying epicardial fat on non-enhanced cardiac CT scans. We demonstrated the feasibility of using this method to replace manual annotations by showing that the automatic method performs as good as manual annotation on a large dataset.

4.1 Introduction

Cardiovascular disease (CVD) is one of the leading causes of death worldwide. (WHO, 2012) Epicardial fat is the adipose tissue which is found between the myocardium and the visceral layer of the pericardium, and thus directly surrounds the entire heart as well as the coronary arteries. Increasing evidence implicates epicardial fat in the etiology of CVD (Cheng et al., 2007; Iacobellis et al., 2005; Kortelainen, 2002). It is thought that through local production of inflammatory factors it may directly contribute to the formation of coronary atherosclerosis (Mahabadi et al., 2010; Bettencourt et al., 2011; Alexopoulos et al., 2010). Few studies have found that epicardial fat is associated with cardiovascular risk factors (Rosito et al., 2008; de Vos et al., 2008). Other studies have shown that epicardial fat is a dominant factor in case of coronary artery disease (Sarin et al., 2008; Mahabadi et al., 2009; Harada et al., 2011). A few population based studies have also been performed. Ding et al. (Ding et al., 2009) investigated whether epicardial fat is an independent predictor of future heart disease events as compared to conventional risk factors on 998 individuals from the MESA study. Mahabadi et al. (Mahabadi et al., 2013) quantified epicardial fat volume on 4093 subjects in order to determine if epicardial fat predicts coronary events in the general population.

Several methods for epicardial fat quantification have recently been developed. Most of these methods are completely manual, which is a tedious procedure to perform. The manual methods are also prone to inter and intra-observer variability. The objective of our study is to develop and evaluate a fully automatic method, which can accurately and robustly segment the pericardium and quantify the amount of adipose tissue contained within. To the best of our knowledge this is the first fully automatic method presented in the literature. Hence, it has the potential to be applied to large scale clinical or population based studies.

Most of the methods described previously require manual delineation of the pericardium, which is subsequently used to quantify the volume of fat. Taguchi et al. (Taguchi et al., 2001) traced the epicardial, subcutaneous and visceral fat. Wheeler et al. (Wheeler et al., 2005) used landmark points to initialize the heart segmentation. Rosito et al. (Rosito et al., 2008) traced the pericardium to delineate the heart from the surrounding structures. Ding et al. (Ding et al., 2008) used a few landmark points around the heart to enclose it in an envelope, similar to the method proposed by Wheeler et al. (Wheeler et al., 2005).

More recently, a semi-automatic method was proposed by Dey et al. (Dey et al., 2008, 2010). Their method needs two interactions. Firstly, the user needs to select the top and the bottom slice in between which the heart is contained. Once this is done, the method uses region growing and anatomical information to segment the heart. Secondly, the user needs to select 5 to 7 control points on the axial slices to pinpoint the location of the pericardium. The degree of interaction of this method is still substantial. Population and clinical studies, as well as clinical workflow, would greatly benefit from a precise and fully automatic method for epicardial fat quantification. Ultimately, findings from such studies could further establish the role of epicardial fat in the development of CVD.

In this chapter, we present a method which is capable of automatically segmenting the pericardium on non-enhanced cardiac CT scans and subsequently quantifying the epicardial fat volume within the pericardium. Our method uses an atlas-based segmentation approach in order to segment the pericardium. The atlas-based segmentation approach is an adaptation of our previous work, where atlas-based segmentation was evaluated with respect to segmenting the heart and its chambers in a multi-center, multi-vendor contrast-enhanced CT (CTA) study. (Kirişli et al., 2010) Our method was evaluated on 98 CT scans with respect to 1) the accuracy of pericardium segmentation 2) the accuracy of epicardial fat quantification and 3) accuracy of the results with respect to the inter-observer variability. The evaluation was conducted by comparing the performance of our method to two independent manual observers.

The remaining of the chapter is organized as follows. Section 4.2 gives details about the imaging data, overview of our method and the experiments we performed. We present our results in Section 4.3, discussion and future work in Section 4.4 and finally the conclusion is provided in Section 4.5.

4.2 Material and methods

4.2.1 Study population and imaging protocol

For this study, we randomly selected 98 subjects from the population-based Rotterdam Study (Hofman et al., 2011), who underwent a multi-detector computed tomography (MDCT) scan of the heart. This study was part of a larger MDCT-project involving calcium-scoring in multiple vessel beds (Elias-Smale et al., 2011). The participants were scanned on two different generations of Siemens scanners (Sensation 16 (n = 55) or Sensation 64 (n = 43), Siemens Medical Solutions, Forchheim, Germany). The cardiac scan ranged from the apex of the heart to the tracheal bifurcation. The Rotterdam Study was approved by the Institutional Review Board with additional specific approval of the CT study. All participants gave written informed consent for the CT examination.

Subject characteristics are provided in Table 4.1. Scan settings were as follows. The scan reached from the apex of the heart to the tracheal bifurcation, no contrast material was used. On the 16-slice MSCT scanner, consecutive non-overlapping 3.0 mm thick slices were acquired within a single breath hold. The collimation was 12 × 1.5 mm, the tube voltage was 120 kV, the effective tube current 30 mAs, and prospective ECG triggering at 50% of the cardiac cycle was used. For the 64-slice scanner, all parameters except the collimation and tube current changed. Collimation was set to 32 × 0.6 mm and the tube current was adopted with respect to the body weight (CARE DOSE, Siemens, Forcheim, Germany) with a reference value of 50, 100 and 190 mAs. The images from both scanners were reconstructed with a 3.0 mm increment and an average field of view (FOV) of 180 mm. The images were reconstructed with a matrix of 512 × 512 using a b35f (medium sharp) kernel, and contained on average 52 slices.

Table 4.1: Characteristics of the subjects (n = 98). Values are mean ± stdev for continuous variables and numbers (%) for dichotomous variables.

Variable	Value
Women	46 (46.9%)
Age (years)	69.4 ± 5.6
BMI (kg/m^2)	27.4 ± 3.9
Systolic blood pressure (mmHg)	147.8 ± 22.3
Diastolic blood pressure (mmHg)	82.2 ± 11.1
Smoking (ever)	69 (70.4%)
Diabetes	7 (7.1%)
Total cholesterol (mmol/L)	5.8 ± 0.9

4.2.2 Method overview

The quantification method consists of two steps: 1) pericardium segmentation, and 2) epicardial fat volume quantification. For pericardium segmentation, we used a multi-atlas segmentation approach, as described in the work of Kirişli et al. (Kirişli et al., 2010). In this approach, manually segmented CTA scans (atlases) are registered to the subject's CT scan. The segmentations of these atlases are mapped onto the subject's scan to be analyzed. The mapped segmentations from each of the atlases are fused to obtain the final pericardium segmentation. This whole procedure is fully automatic. The epicardial fat is subsequently quantified by applying a threshold of -200 to -30 HU (Yoshizumi et al., 1999) to the segmented pericardium, followed by connected component analysis. Details with respect to the atlases used, the registration approach, and the fat quantification are presented in the subsequent sections. Figure 4.1 shows an overview of all the steps involved in the automatic method.

4.2.3 Atlas selection and surface computation

CTA scans were used as atlas images because of their higher resolution and the better visibility of the cardiac chambers (due to the presence of contrast material). This enables the observers to accurately delineate the pericardium manually. Eight previously acquired CTA scans from different subjects were included in as the atlas scans. Readers are referred to (Kirişli et al., 2010) for detailed information on atlas selection.

The manually obtained contours of the atlas scans were converted to 3D surfaces. Figure 4.2 shows the resulting heart surfaces for the eight atlas scans.

4.2.4 Multi-atlas based segmentation

Multi-atlas segmentation (Rohlfing et al., 2005) is a process in which multiple atlas images with corresponding manually annotated label images are individually

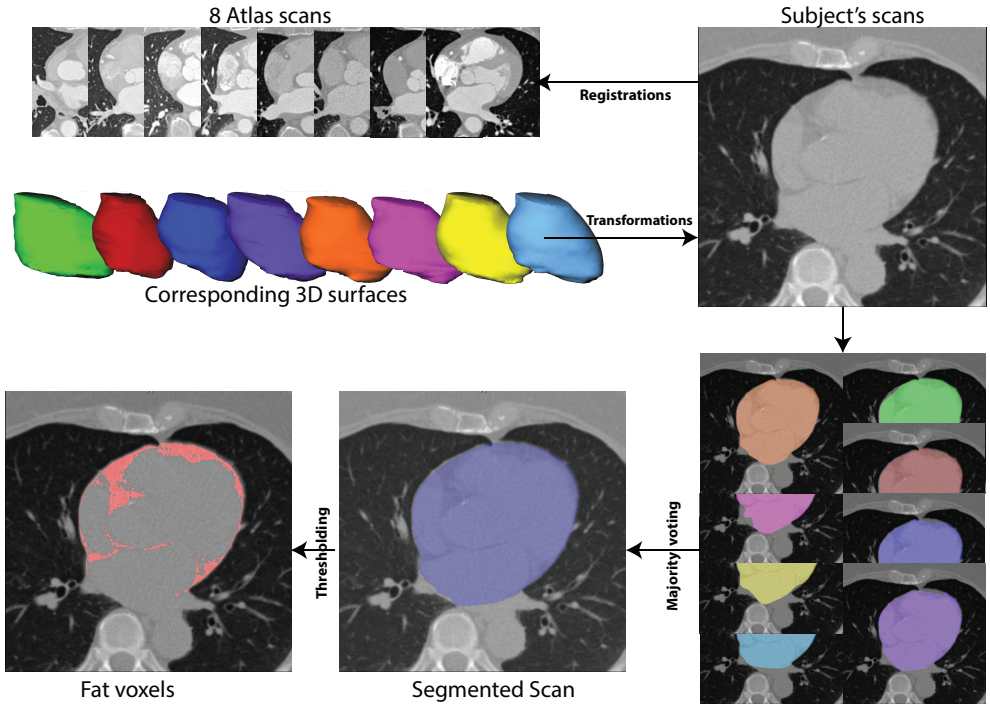

Figure 4.1: Overview of the segmentation process. Top left: Eight CTA atlas scans and the corresponding manually segmented 3D surfaces. Top right: CT scan to be segmented. The atlas scans are registered and the 3D surfaces are transformed to match the subject scan. Bottom right: The 3D surfaces are combined using majority voting; the resulting segmentation is overlaid in blue. Bottom left: Resulting fat voxels, obtained after thresholding and connected component analysis.

registered to the subject scans. The segmentation of the subject scans is then obtained by fusing all the resulting transformed label images (Rohlfing et al., 2004). In this work we use majority voting to fuse the label images.

Image registration (Maintz and Viergever, 1998) is used to spatially align the atlas scans and the subjects scan. In the registration procedure, the transformation parameters T that minimizes the cost function $C(T; I_f, I_m)$ between the fixed image (I_f) and the a moving image (I_m) are determined. The optimization problem can be mathematically represented as:

$$\hat{T} = \arg\min_{T} C\left(T; I_f, I_m\right) \ . \tag{4.1}$$

Detailed information on registration is provided elsewhere (Bankman, 2000; Suri et al., 2005). The registration strategy used in our approach involves a two-stage registration approach, where in the first stage I_m and I_f are roughly aligned using an affine transformation and in the second stage a B-spline non-rigid transformation is

applied. In both cases a multi-resolution strategy is used. The registration steps and the parameters are explained in more detail in Section 4.2.8, where we also compare the performance of registration with and without masking certain areas of the image.

The resulting transformations from the registration steps are used to map each of the eight atlas surfaces onto the subject's scan. Once this is done, the 3D surface intensities are converted to binary masks and majority voting is applied to obtain the final pericardium segmentation (See Figure 4.1 for a visual representation).

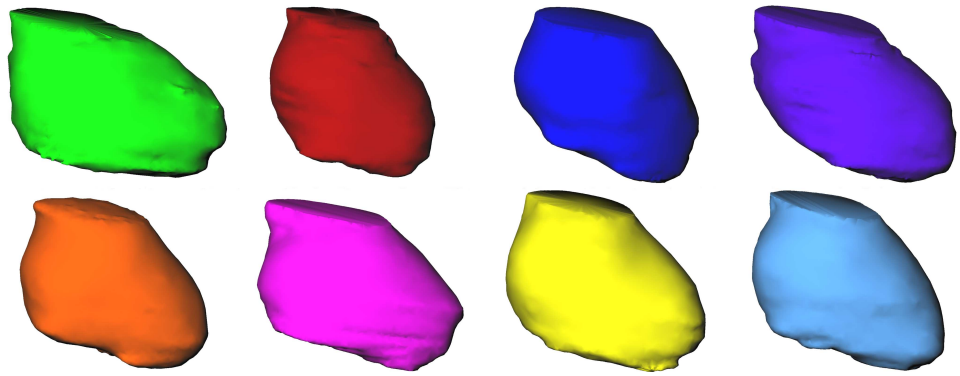

Figure 4.2: The eight pericardium atlas surfaces used for atlas-based segmentation illustrating the encountered shape and size variations in the atlas images.

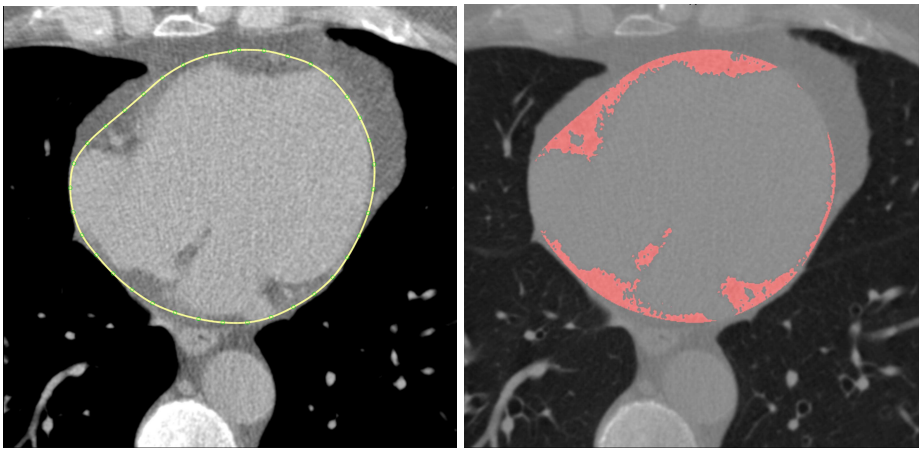

(a) (b)

Figure 4.3: (a) A random axial slice showing the result of a manually obtained whole heart segmentation (with adjusted windowing level, for better visibility). (b) Corresponding slice showing the voxels containing epicardial fat.

4.2.5 Epicardial fat quantification

The automatically obtained pericardium segmentation is used as a region of interest (ROI) to quantify the adipose tissue voxels. A threshold window of -200 to -30 HU is applied to obtain the adipose tissue. A connected-component analysis (Samet and Tamminen, 1988) is subsequently applied to all adipose tissue voxels using an 18-neighbourhood rule, in order to remove regions smaller than 10 voxels (2.8 mm^3) in size, which we consider to be noise.

4.2.6 Reference standard

Two experienced observers (D.B. and A.R.), blinded to the patient information as well as to the results of each other, manually traced the pericardium in each of the CT scans, as shown in Figure 4.3a. A dedicated tool implemented in MeVisLab (`http://www.mevislab.de`) was used by the observers for manual annotations. Once the pericardium was delineated, a threshold window of -200 to -30 HU was applied to the segmented region (Yoshizumi et al., 1999). Adipose tissue voxels were then automatically extracted using connected-component analysis and the volume of fat in milliliters (ml) was computed. The reference standard obtained this way contains both pericardium segmentations and epicardial fat volume quantifications (Figure 4.3b).

4.2.7 Statistical analysis

We report the Dice similarity index and the mean surface distance error between the pericardial heart segmentation by the automatic method and each of the manually obtained segmentations. To evaluate the performance of the fat quantification method per patient, Pearson's correlation coefficient (R) was calculated, linear regression was performed, and Bland-Altman plots were created. Furthermore, the accuracy of the method was compared to the inter-observer variability. The analyses were performed using MATLAB version 7.9.0. (The MathWorks, Natick, MA) and IBM SPSS Statistics version 20 (IBM Corp, Armonk, NY).

4.2.8 Experiments

Our method consists of segmenting non-enhanced CT scans with the help of contrast-enhanced CT atlas scans. The registration problem we face here is that the fixed image (I_f) and moving image (I_m) have different characteristics, both in terms of contrast and resolution. The CT scans in which we aim to quantify the epicardial fat has an average in-plane resolution of 0.35 × 0.35 mm^2 and a slice thickness of 3.0 mm, whereas the CTA atlases have an average in-plane resolution of 0.32 × 0.32 mm^2 and a slice thickness of 0.4 mm. In order to obtain the optimal parameters to register the CTA atlases and the CT subjects, we performed pilot experiments on a subset of 35 randomly selected CT datasets. Two registration strategies were investigated and the segmentation results were compared to the results of one of the observers. In both

Table 4.2: Table representing the results of the Registration Strategy. Values represent mean ± stdev.

	Strategy 1	**Strategy 2**
Dice Similarity Index %	90.0 ± 3.2	89.6 ± 1.9
Mean Surface Distance mm	3.4 ± 1.3	3.5 ± 0.8

strategies, the CTA atlas was used as the fixed image (I_f) and the subjects CT scan was used as the moving image (I_m).

Strategy one: The similarity metric was computed by randomly sampling intensity values from the whole image.

Strategy two: The similarity metric was computed by randomly sampling intensity values within the heart region only (by using a fixed heart mask).

As mentioned previously, a two-stage registration approach was used. In the first stage an affine transformation was used. In the second stage, a non-rigid registration using a B-spline transformation (Rueckert et al., 1999) was employed while using the results of the affine transformation to initialize the registration. Mutual Information (Mattes et al., 2003) was used as similarity measure for the cost function C in Eq. 4.1. Optimization was performed using Adaptive Stochastic Gradient Descent, the number of voxels sampled in each iteration was set to 2048 (Klein et al., 2009), and the number of iterations were set to 512 for the affine transformation and 2048 for the B-spline transformation. For further details about parameter selection and optimizations readers are referred to our previous study (Kirişli et al., 2010). All registrations were performed using Elastix (Klein et al., 2010), a publicly available software package (`http://elastix.isi.uu.nl`).

The heart mask was used in both stages of the registration approach. The main purpose of using the fixed mask was to prevent the registration to be affected by tissues surrounding the heart, such as the lungs, rib cage and the vertebra. Figure 4.4 shows a random axial slice of one of the fixed masks used for the registration optimization. The mask was created by dilating the original manually annotated pericardium by 1 cm. The masks were created once, only for the atlas scans and not the subject scans. Hence, called the fixed mask. Table 4.2 shows the results obtained for both the strategies. It can be observed that the average accuracy of both strategies was very similar in terms of the mean, but using the mask resulted in a smaller standard deviation. It was also confirmed visually that the accuracy of finding the pericardium using strategy two was better than when using strategy one. Further experiments on the entire dataset were thus performed using the registration with the mask.

4.3 Results

4.3.1 Agreement between the automatic method and the observers

A visual check showed that 95 out of 98 segmentations were successful. Three segmentations failed due to registration errors caused by anatomical and FOV

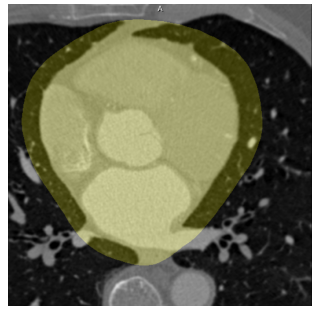

Figure 4.4: Random axial slice with the yellow overlay representing the fixed mask used for the registration.

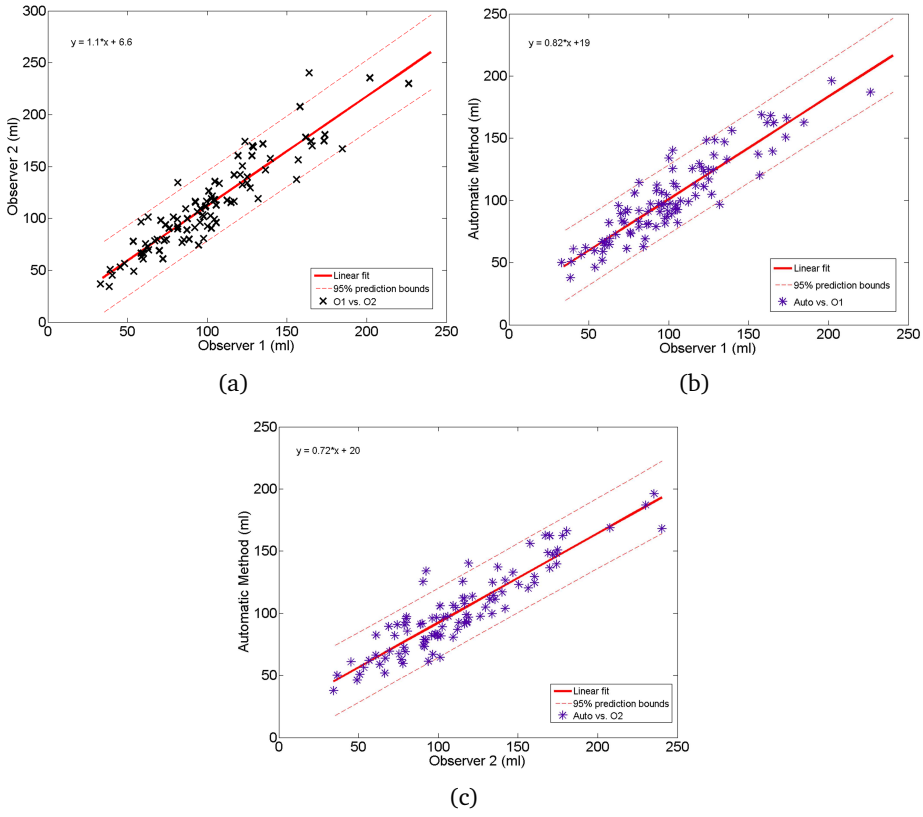

Figure 4.5: Scatter plots of automatic versus manual fat quantification methods and results from linear regression: (a) Correlation between the two observers. (b) Correlation between observer 1 and the automatic method. (c) Correlation between observer 2 and the automatic method.

variations. These scans were excluded from further analysis.

The subjects had an average fat volume of 101 ± 38 ml according to Observer 1 and 113 ± 43 ml according to Observer 2. The automatic method found the average fat volume to be 102 ± 34 ml. A Dice similarity index of 89.1% and 89.2% was obtained between the automatic segmentation and each of the manual segmentations, respectively. The mean surface distance between the automatically derived cardiac surface and the observer segmentations was 3.8 ± 1.1 mm and 3.5 ± 0.7 mm, respectively. A Pearson correlation R of 0.91 ($P < 0.001$) was obtained for fat quantification results between the automatic segmentation and each of the manual segmentations. The mean absolute difference between the automatic method and each of the manual segmentations with respect to the amount of quantified fat was 11.6 ml and 16.6 ml, respectively. The linear regression plots are shown in Figure 4.5. The numbers obtained from the Bland-Altman analysis and the confidence intervals of the linear regression are shown in Table 4.3 with a graphical representation in Figure 4.6. It can be noted that the bias from the Bland-Altman analysis with respect to observer 1 is almost zero and the automatic method slightly underestimates the volume of epicardial fat as compared to observer 2.

4.3.2 Inter-observer agreement

An average Dice similarity coefficient of 88.9% was found between the segmentations of the observers. The mean surface distance between the two observers was 4.3 ± 1.0 mm over all datasets. With respect to the amount of quantified epicardial fat, the mean absolute difference between the two observers was 15.6 ml, and the Pearson correlation coefficient was 0.92 ($P < 0.001$). A Bland-Altman analysis of the data showed that the limits of agreement were between -45.3 and 21.3 ml and a bias of -12.1. Figure 4.5 and Figure 4.6 show the correlation graph and the Bland-Altman analysis.

4.4 Discussion

In this study, we presented a fully automatic method for epicardial fat quantification. The method is based on automatic pericardium segmentation. A good correlation with manual quantification was observed, with differences very similar to the inter-observer variability.

The Dice similarity index (overlap area) between the automatic pericardium segmentation and each of the manual annotations was slightly better than the inter-observer Dice similarity coefficient. The mean surface distance error between the automatic and manual segmentations corresponds to 1.5 voxels in the slice direction, which can be considered small. When the actual amount of fat volume quantified using our method was compared to each of the observers, it resulted in a mean absolute difference of 11.6 ml and 16.6 ml respectively. This difference in volume is very close to the inter-observer agreement, which was 15.6 ml. The same conclusion can be drawn from the correlation coefficient R obtained with respect to the quantified fat volume of the automatic method and the manual observers.

Table 4.3: Performance of the whole heart segmentation; comparing the automatic method to each of the observers and the observers to each other.

	Automatic Vs Observer 1	**Automatic Vs Observer 2**	**Observer 1 Vs Observer 2**
	Segmentation Measures		
Dice Similarity Index (mean ± stdev)%	89.1 ± 2.6	89.2 ± 1.9	88.9 ± 2.5
Mean Surface Distance (mean ± stdev)mm	3.8 ± 1.1	3.5 ± 0.7	4.3 ± 1.0
	Quantification Measures		
Correlation R	0.91	0.91	0.92
Linear Regression (CI for β)	0.75 to 0.90	0.65 to 0.79	0.96 to 1.15
Bland-Altman Bias (95% CI)	0.8 (31 to -29)	-11.3 (25 to -47)	-12.1 (21 to -45)

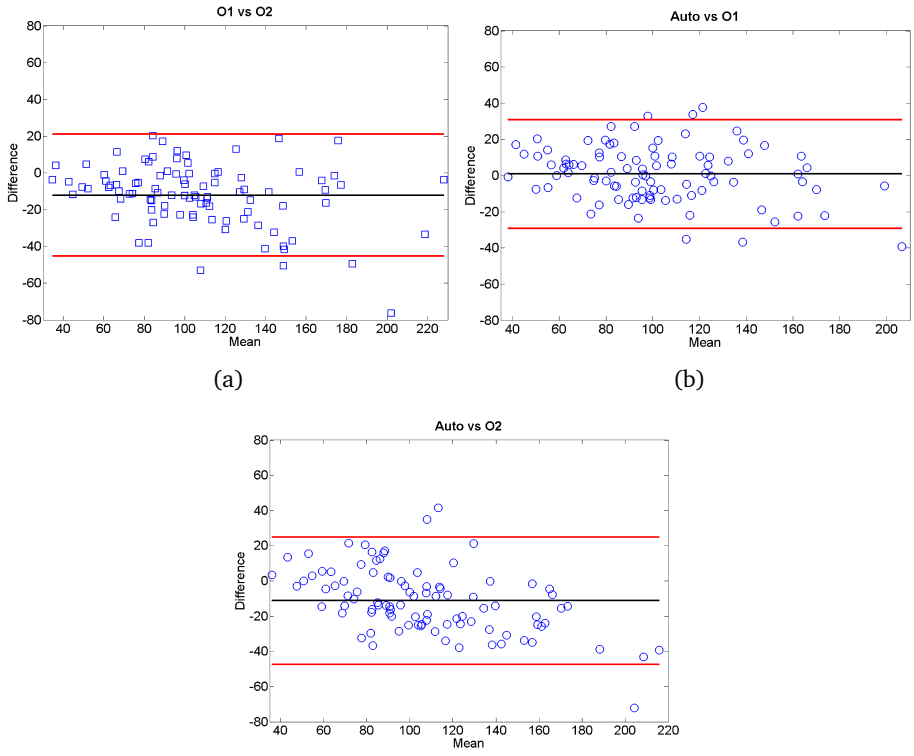

Figure 4.6: Bland-Altman analysis: (a) Between observers. (b) Between automatic method and observer 1. (c) Between automatic method and observer 2.

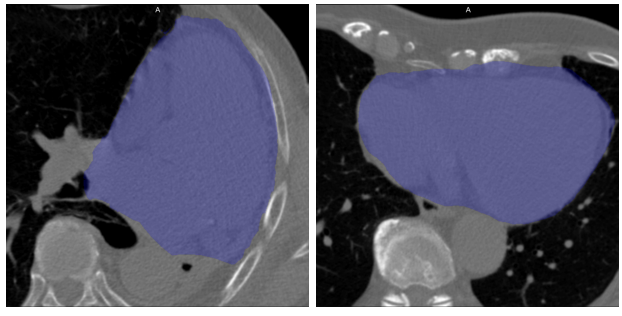

Figure 4.7: Excluded subjects (a) Subject with lung removed (b) Segmentation leaking into the ribcage due to rare anatomical variation in heart shape.

Compared to the existing quantification methods, our method is the first that is fully automatic. The methods proposed in (Ding et al., 2008, 2009; Mahabadi et al., 2013; Rosito et al., 2008; Taguchi et al., 2001; Wheeler et al., 2005) either use manual tracings of the different tissue types, or a manual approach to delineate the pericardium, before quantifying the adipose tissue voxels. This is a tedious and time-consuming task to perform. The semi-automatic method proposed in (Dey et al., 2008, 2010) needs two interactions, which could limit the use of the method in processing a large number of datasets in an epidemiologic setting.

The three subjects that were excluded from the analysis had the following issues: one subject underwent pneumonectomy (removal of a lung) causing a very unusual position of the heart (see Figure 4.7a), the other had a heart shape anatomically quite different from the others (see Figure 4.7b), the last one had a different field of view compared to the atlas scans used. The large difference between the atlas scan and the subject scan caused the registration to fail, which resulted in erroneous segmentation of the pericardium.

There has been some confusion in the literature between the nomenclatures of the adipose tissue contained within the pericardium (Thomas et al., 2010); some studies call it epicardial fat tissue, whereas others call it pericardial fat tissue. Based on the definition provided here (Iacobellis, 2012) we decided to denote the adipose tissue contained within the pericardium as epicardial fat. In short, in this definition epicardial fat is the adipose tissue between the myocardium and the visceral layer of the pericardium.

We did not investigate to what extent the method can be used on multiple scanner types; in this study, we only demonstrated the feasibility of using the method on two generations of Siemens scanners. However, as our method is based on multi-atlas segmentation, we are confident that the same approach would work on other scanner types, as long as the subject scans and the atlas scans have a similar field of view. It has been demonstrated in our previous study (Kirişli et al., 2010), that atlas-based segmentation of the pericardium was performed with a similar accuracy with respect to multi-vendor/multi-center CTA datasets. If required, the method could utilize atlas scans from the same scanner.

In the current setup, visual inspection was still required to check the accuracy of the pericardium segmentation, which resulted in discarding the three scans on which the segmentation failed. Instead of discarding these scans, or in case of small failures, manual correction before fat quantification is an option. We did not integrate this in our protocol, as the results were sufficiently accurate without adaptation.

4.5 Conclusions

We developed and evaluated an automatic method for pericardium segmentation and subsequent epicardial fat quantification. We demonstrated that our automatic approach achieved good correlation to manual quantifications. The automatic method described in this paper could potentially be used on large clinical or population studies in order to investigate the relationship between epicardial fat volume and CVD.

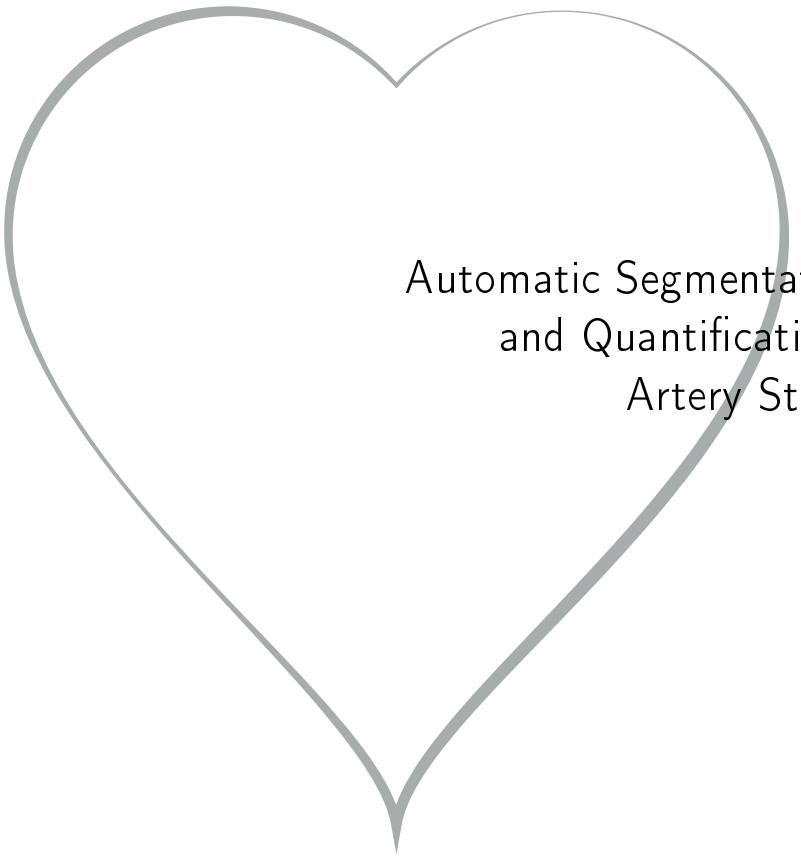

5

Automatic Segmentation, Detection and Quantification of Coronary Artery Stenoses on CTA

This chapter is based on the manuscript:
Automatic Segmentation, Detection and Quantification of Coronary Artery Stenoses on CTA, **R. Shahzad***, H.A. Kirişli*, *(* both authors contributed equally to this research)* C. Metz, H. Tang, M. Schaap, W.J. Niessen, L. van Vliet and T. van Walsum, *The International Journal of Cardiovascular Imaging, in press*, 2013.

Abstract

Purpose Accurate detection and quantification of coronary artery stenoses is an essential requirement for treatment planning of patients with suspected coronary artery disease. We present a method to automatically detect and quantify coronary artery stenoses in CTA.

Methods First, centerlines are extracted using a two-point minimum cost path approach and a subsequent refinement step. The resulting centerlines are used as an initialization for lumen segmentation, performed using graph cuts. Then, the expected diameter of the healthy lumen is estimated by applying robust kernel regression to the coronary artery lumen diameter profile. Finally, stenoses are detected and quantified by computing the difference between estimated and expected diameter profiles. We evaluated our method using the data provided in the *Coronary Artery Stenoses Detection and Quantification Evaluation Framework*.

Results Using 30 testing datasets, the method achieved a detection sensitivity of 29% and a PPV of 24% as compared to QCA, and a sensitivity of 21% and a PPV of 23% as compared to manual assessment based on consensus reading of CTA by 3 observers. The stenoses degree was estimated with an absolute average difference of 31%, a root mean square difference of 39.3% when compared to QCA, and a weighted kappa value of 0.29 when compared to CTA. A Dice of 68% and 65% was reported for lumen segmentation of healthy and diseased vessel segments respectively. According to the ranking of the evaluation framework, our method finished fourth for stenosis detection, second for stenosis quantification and second for lumen segmentation.

Conclusions Coronary artery lumen can be automatically segmented with a precision similar to the expert's, but detection and quantification of coronary artery stenosis is still an unsolved problem; discrimination between significant and non-significant lesions remains a challenge.

5.1 Introduction

Coronary artery disease (CAD) is one of the leading causes of death worldwide (WHO, 2012; Roger et al., 2012). CAD induces plaque build-up in the coronary arteries, which may cause luminal narrowing also known as *stenosis*. Stenoses may induce myocardial infarction; it is therefore crucial to detect CAD at an early stage.

Many diagnostic tests are available for detection of CAD (Fayad and Fuster, 2001). At present, invasive coronary angiography (ICA) is the reference standard imaging technique for diagnosing CAD and quantitative coronary angiography (QCA) is used to quantify the degree of stenosis. However, ICA is an invasive procedure and is limited by its projective nature. Computed tomography coronary angiography (CTA) on the other hand, is increasingly used to assess CAD and has the advantage over ICA of being non-invasive. Furthermore, it provides high resolution three-dimensional (3D) images of the coronary arteries. In addition to the detection and quantification of coronary artery stenoses, CTA can also provide additional information regarding the type of plaque (calcified, mixed or soft) (Weustink and de Feyter, 2011). It has been shown that CTA scans can be used to accurately identify the presence and severity of the stenoses in comparison to ICA in (Miller et al., 2008). However, interpreting CTA images for the purpose of stenosis detection and quantification requires considerable experience to prevent underestimating or overestimating obstructive plaque lesions (Pugliese et al., 2009), and is therefore a tedious task. Whereas we are focusing on stenosis grading, similar approaches may be relevant for CT fractional flow reserve (FFR) as well, where the combination of computational flow models and accurate segmentations may predict the hemodynamic significance of a lesion (Melchionna et al., 2013; Min et al., 2012).

Consequently, the number of publications presenting and/or evaluating (semi-) automatic coronary artery stenosis detection and quantification methods on cardiac CTA have increased in recent years. An algorithm evaluation framework dedicated to this problem has been introduced in 2012 (`http://coronary.bigr.nl/stenoses`) (Kirişli et al., 2013).

Different approaches have been proposed to address the challenge of (semi-) automatically detecting and quantifying stenoses. These methods can be categorised into two groups: 1) methods that depend on accurate lumen segmentation to compute/estimate healthy and diseased lumen diameters in order to quantify stenoses (Arnoldi et al., 2010; Halpern and Halpern, 2011; Khan et al., 2006; Kelm et al., 2011; Wesarg et al., 2006; Xu et al., 2012) and 2) methods that use image features or pattern recognition approaches to detect stenoses (Saur et al., 2008; Tessmann et al., 2009; Zuluaga et al., 2011).

In this chapter, we present an automatic method for coronary artery lumen segmentation, stenosis detection and quantification. The method aims at facilitating and supporting the interpretation of cardiovascular CTA data by radiologists. The method has been evaluated through the *Coronary Artery Stenoses Detection and Quantification Evaluation Framework* (Kirişli et al., 2013).

The remainder of this chapter is organized as follows. In Section 5.2, we describe the data used, our method and the parameter values selection. Section 5.3 is

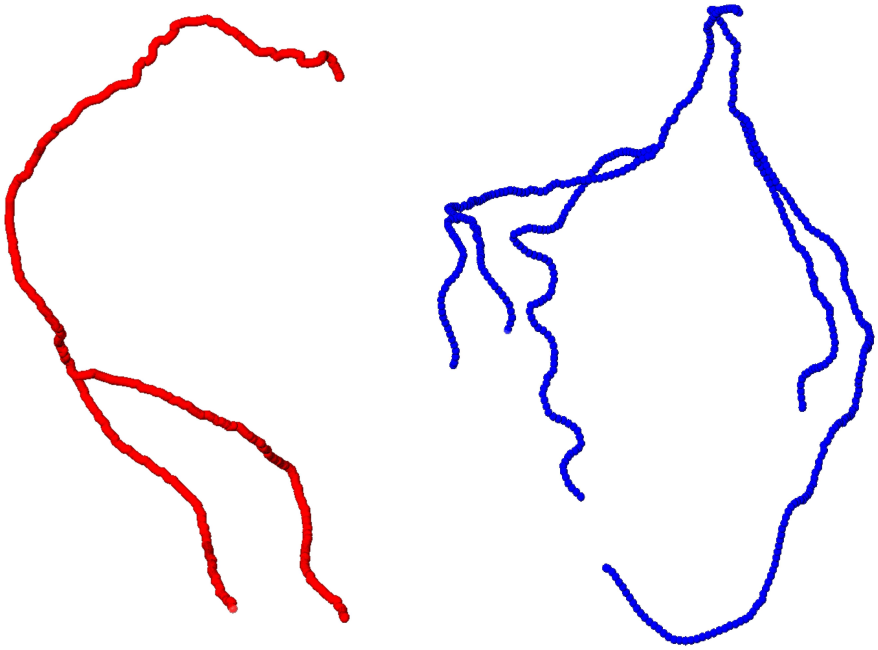

(a) right coronary artery branch (b) left coronary artery branch

Figure 5.1: Extracted initial centerlines for one of the datasets.

dedicated to the evaluation of our approach. Results of our approach are discussed in Section 5.4, as well as the limitations and possibilities for future studies. Conclusions are given in Section 5.5.

5.2 Materials and method

5.2.1 Imaging data

The data used for this study was obtained from the publicly available Coronary Artery Stenoses Detection and Quantification Evaluation Framework (`http://coronary.bigr.nl/stenoses`). The datasets provided by this framework were retrospectively acquired in three university medical centers (Erasmus MC, University Medical Center, Rotterdam, the Netherlands; University Medical Center Utrecht, Utrecht, the Netherlands; and Leiden University Medical Center, Leiden, the Netherlands). The patients underwent both CTA and QCA examinations. Below, we provide information about the image acquisition, data selection and reference standards. Additional information can be found on the website (`http://coronary.bigr.nl/stenoses/about.php`).

The CTA data was acquired on : 1) a dual-source CT scanner (Somatom Definition, Siemens, Forchheim, Germany) at the EMC, 2) a 64-slice CT scanner (Brillance 64, Philips Medical Systems, Best, the Netherlands) at the UMCU, and 3) a 320-slice CT scanner (Aquilion ONE 320, Toshiba Medical Systems, Tokyo, Japan) at the LUMC. A non-enhanced CT scan was performed before the CTA; the total calcium score for each patient was calculated using a dedicated software in each center.

A single image volume per patient was used, reconstructed at the mid-to-end diastolic phase (350 ms before the next R-wave or at 65% to 70% of the R-R interval), with either retrospective (Siemens and Philips data) or prospective (Toshiba data) ECG gating.

Sixteen patients, distributed over five calcium categories in order to have a representative population that undergoes CTA examination, were selected in each of the three centers, resulting in 48 datasets. The calcium categories (Agatston et al., 1990) are defined as follows : no calcium (11 patients, 23%), between 0.1 and 10 (6 patients, 10%), between 11 and 100 (14 patients, 31%), between 101 and 400 (11 patients, 23%), and above 400 Agatston score (6 patients, 12%). The population has a mean age of 58.76 ± 8.71 (41-80) years old and consists of 30 males (63%).

Eighteen of the 48 CTA images, together with the CTA and QCA reference standards, were made available for training; the remaining 30 datasets were used for testing the algorithms. For testing, only the CTA images were made available. The distribution of patients over the two sets is explained in detail in recent work of Kirisli et al. (Kirişli et al., 2013).

Three independent experienced observers from Erasmus MC, University Medical Center Rotterdam, analysed the CTA datasets and provided the ground truth via consensus reading. A dedicated tool implemented in MeVisLab (`http://www.mevislab.de`) was used by the observers for the annotations. QCA analysis was performed by an independent observer blinded to the CTA results. The ground truth data consists of quantification and stenosis detection on both the CTA and ICA datasets, as well as lumen segmentation on the CTA dataset.

5.2.2 Method

The method described in this chapter consists of the following steps: 1) centerlines are extracted using predefined start and end points in the arteries, 2) bifurcation points of the extracted vascular tree are detected and the centerlines are subsequently divided into segments 3) coronary artery lumen segmentation is performed using the centerline segments as initialization, and 4) stenoses are detected and quantified using an area based approach.

Centerline extraction

The centerlines of the coronary artery tree are extracted as follows.

First, for each branch of the coronary artery tree, an initial centerline is obtained, by applying the minimum cost path extraction method presented in (Metz et al., 2009). A 3D path with minimum cost is found between two manually placed seed

points in the coronary arteries, located at the ostium and at the distal end of each coronary artery. The cost image $C_v(x)$, (with x a location in the image) used for centerline extraction is based on a multi-scale vesselness measure $V(x)$ (Frangi et al., 1998) and a sigmoid like intensity threshold function $T(x)$ (Metz et al., 2009), and is defined as:

$$C_v(x) = \frac{1}{V(x)T(x) + \epsilon} \quad , \tag{5.1}$$

where ϵ is a small positive value introduced to avoid singularities (See Section 5.2.3, for parameter values).

However, the initial centerlines obtained are inaccurate at the bifurcations and at calcified locations, where the centerline is attracted towards the calcified part of the vessel due to relatively low cost values inside the calcifications. Therefore, the centerlines are refined in a subsequent step.

In this second step, calcium lesions within the artery are suppressed, based on the intensity profile of the contrast material along the initially extracted centerline. In the ideal case, i.e. a healthy vessel presenting no calcified plaque, the intensity profile is a smooth curve with a gradual decrease in intensity along the artery (see Fig 5.2(a)) (Rybicki et al., 2008; Steigner et al., 2010). But, in the case that a centerline passes through a calcified plaque, the intensity profile presents a spike, indicating the presence of a high intensity object along the centerline path. In the case where the contrast material is not evenly distributed throughout the artery, intensity variations not corresponding to calcified plaques may also appear in the intensity profile. In order 1) to differentiate true calcium objects from noise, and 2) to estimate the intensity value of the contrast material within the coronary artery, we apply a cubic fit to the intensity profile of the initially extracted centerline. Fig 5.2 shows examples of intensity profiles along different artery segments.

Given an intensity profile for centerline points $x \in X$, where X is the set of centerline points, point x is assigned as belonging to a calcium object if it obeys the condition:

$$I(x) - F(x)|_{x \in X} \geq T_{ca} \quad , \tag{5.2}$$

where $I(x)$ is the CTA image intensity at position x along the centerline, $F(x)$ is the value at position x based on a fitted cubic polynomial and T_{ca} is a predefined threshold value (See Section 5.2.3).

All the centerline points x which satisfy Eq. 5.2 are treated as seedpoints to initialize a region growing segmentation with a 3D 6-neighbourhood relation. If a connected voxel has an intensity greater than equal to $max_{x \in X}(F(x))$, it is classified as belonging to a calcium object. The segmented calcium object is suppressed by setting its intensity value to 1024 grayscale value (GV) (1024 GV = 0 Hounsfield unit). Fig 5.3 shows an example where a calcium lesion is suppressed.

Subsequently, to move the centerlines running close to the border of the lumen towards the vessel center, we generate a stack of multi-planar reformatted (MPR) images, i.e. a stack of images perpendicular to the initial centerline. We then apply a minimum cost path approach to this image stack, as proposed by Tang et

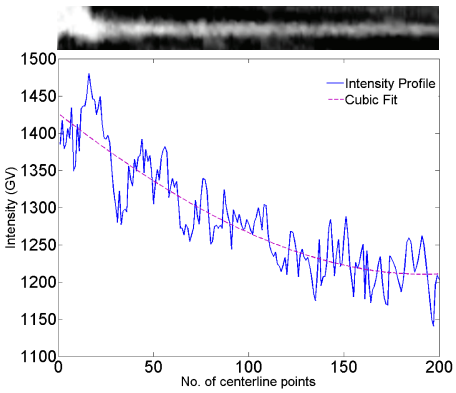

(a) segment without calcium objects

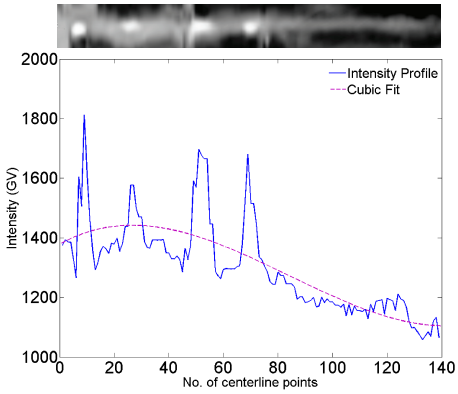

(b) segment with multiple calcium objects

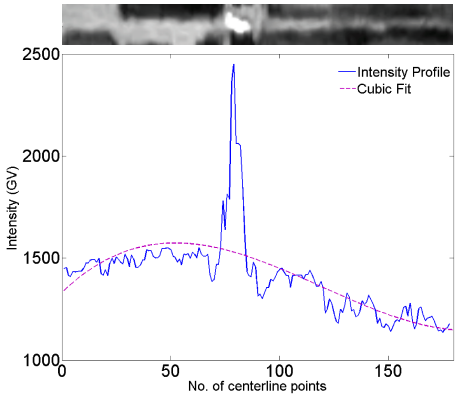

(c) segment with a high density calcium object

Figure 5.2: Plot of the intensity (in GV) as a function of position along the centerline and the corresponding CMPR images for three coronary artery segments

al. (Tang et al., 2012). Using a modified cost image $C_{mv}(x)$ based on both $V(x)$ and a medialness measure $M(x)$ (Gülsün and Tek, 2008), defined as:

$$C_{mv}(x) = \frac{1}{V(x)M(x) + \epsilon} \quad . \tag{5.3}$$

Fig 5.4 shows an example of an MPR image generated using the refined centerlines.

From centerlines to segments

To extract the lumen centerlines, a unique starting point (located in the ostium) and multiple end points are used. As a consequence, the extracted centerlines present

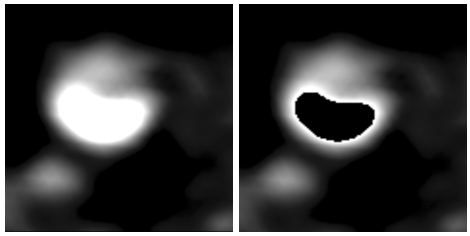

(a) (b)

Figure 5.3: A random cross-sectional image slice through a calcium lesion. (a) before calcium suppression (b) after calcium suppression.

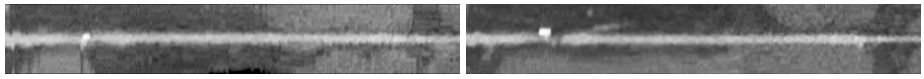

(a) (b)

Figure 5.4: (a) CMPR image before calcium object suppression and centerline refinement (b) CMPR image after calcium object suppression and centerline refinement. It can be observed from image (b) that the calcium object is much better separated from the lumen.

multiple overlapping paths. At locations where a vessel bifurcates, a sudden drop in the vessel diameter occurs. This influences the stenoses detection and quantification step which is based on cross-sectional vessel area. In order to facilitate further processing, we first filter the centerline points using Mean Shift filtering (Carreira-Perpinan, 2007), such that matching co-linear centerlines are closer to each other. Subsequently, we can merge centerlines representing the same segment, and detect bifurcations at locations where centerlines are diverging.

For the filtering, each centerline $S_{i=1\ldots m}$ (with m the total number of centerline segments) is equidistantly resampled to a set of spatial points $\{\mathbf{x}_1 \ldots \mathbf{x}_{n_i}\}$ with n_i the number of points of the centerline S_i. We then filter the centerlines using the approach proposed by van Walsum et al. (van Walsum et al., 2008), and subsequently build a graph from these filtered centerlines representing the coronary tree structure.

The Mean Shift filtering algorithm used is represented as follows:

$$\mathrm{x}_{kl}^{\tau+1} = \sum_{ij} \frac{c_{kl,ij}\ \phi_{kl,ij}\ G_s\big(\left|\mathrm{x}_{kl}^{\tau} - \mathrm{x}_{ij}\right|\big)}{\sum_{i'j'} c_{kl,i'j'}\ \phi_{kl,i'j'}\ G_s\big(\left|\mathrm{x}_{kl}^{\tau} - \mathrm{x}_{i'j'}\right|\big)}\ \mathrm{x}_{ij}\ , \tag{5.4}$$

which states that in each iteration, point x is replaced with a weighted average of the points of all centerlines. The subscripts ij, kl represent the j^{th} point on the i^{th} centerline and the l^{th} point on the k^{th} centerline. Convergence is reached if the distance between x^{τ} and $\mathrm{x}^{\tau+1}$ is less then a small threshold (δ).

The weights in Eq. 5.4 have three components. $c_{kl,ij}$ is a correspondence term, based on connectivities between points of different centerlines. It uses Dijkstra graph search algorithm (Dijkstra, 1959) to determine the set of connections $D_{ki} = \{d_{kl,ij}\}$ between centerlines S_k and S_i, with $d_{kl,ij}$ a connection between $\mathbf{x}_{kl}$ and $\mathbf{x}_{ij}$. $c_{kl,ij}$ is defined as:

$$c_{kl,ij} = \begin{cases} 0 & \text{if } d_{kl,ij} \notin D_{ki} \\ \left|\{d_{kl,ij'}\}\right|^{-1} & \text{if } d_{kl,ij} \in D_{ki} \end{cases} \tag{5.5}$$

with $|\cdot|$ the cardinality of the set.

$\phi_{kl,ij}$ decreases the weights for points with differently oriented tangents, and prevents averaging over bifurcations. It is defined as:

$$\phi_{kl,ij} = G_\phi\big(\text{acos}\left(\mathbf{t}_{kl} \cdot \mathbf{t}_{ij}\right)\big) \ , \tag{5.6}$$

with G_ϕ the Gaussian kernel with standard deviation σ_ϕ and $\mathbf{t}_{ij}$ the (normalized) tangent vector at $\mathbf{x}_{ij}$. This orientation factor is 1 when the tangents are parallel, and less then 1 when the tangents diverge.

G_s is the Gaussian weighted distance with a standard deviation of σ_s to decrease the influence of points far away.

Application of Eq. 5.4 to all points x_{ij} of all centerlines S_i yields shifted centerlines S_i'. The shifting process is followed by combining these shifted centerlines into a directed graph representation. To this end, all centerlines are added to a graph consecutively, where the initial graph is empty. For each centerline to be added, the overlapping parts with the existing graph are determined, and the overlapping parts are merged in the graph's data structure. For each of the non-overlapping parts, new edges are created in the graph. After merging all the centerlines into the graph, each path and node (bifurcation point) of the graph structure contains references to the corresponding parts of the (shifted) centerlines. Fig 5.5 shows an example of a segmented and labelled coronary artery tree, where different colors indicate different segments and the white balls represent the bifurcation points, start points and the end points.

Lumen segmentation

The coronary lumen is segmented using a method combining graph-cuts and robust kernel regression (Schaap et al., 2009b). The method is applied segment wise and uses the refined centerline as initialization. The segmentation process is performed on the MPR image stack.

The graph-cuts method uses an application specific unary term based on the image intensities of the centerlines (voxel likelihood) and a binary term based on the image gradient magnitude (edge term). Essentially, the voxel likelihood term assigns high foreground weights and low background weights to voxels with similar intensities as the centerline intensities, and vice versa for voxels that have dissimilar intensity values. The voxel likelihood term is defined as:

(a) Resulting right coronary artery tree (b) Resulting left coronary artery tree

Figure 5.5: Result of automatic bifurcation detection in which different colors represent different segments.

$$Pr(I_x|f_x = 1) = -0.5\left(0.75 - 0.25\ \mathrm{erf}\left(\frac{D_x - T_{in}}{\sigma_i}\right)\right) \left(\mathrm{erf}\left(\frac{D_x - T_{out}}{\sigma_i}\right) - 1\right) \tag{5.7}$$

with $D_x = |I_x - \hat{I}_{x'}|$ the absolute difference between the intensity of the voxel (I_x) and the local intensity estimate($\hat{I}_{x'}$), T_{in} the threshold parameter for intensities within the lumen, $T_{out} = \lambda$(Mean(I) - I_o) the difference between the mean intensity I along the centerline and the intensity outside I_o, i.e the threshold parameter for intensities outside the lumen. Fig 5.6b shows an axial slice after the application of Eq 5.7.

The edge term uses the gradient magnitude at the boundary of two voxels. A higher value corresponds to a high probability of the voxel label being switched. The weight of a label switch between voxel x and y is defined as:

$$w_{x,y} = -log\left(1 - exp\left(\frac{-|\nabla I|^2(x,y)}{2\sigma_g^2}\right)\right) , \tag{5.8}$$

After the graph-cut segmentation each voxel is assigned to the lumen or non-lumen (see Fig 5.6c). Because this segmentation is discrete and because it can contain

outliers, the segmentation is smoothed and outliers are removed with a robust kernel regression approach. The graph-cut lumen boundary is first described in a cylindrical coordinate system by finding, in each cross-section, the intersection between rays, sampled at fixed angles from the centerline. This representation is subsequently smoothed with a robust kernel regression approach, ensuring that both outliers are removed and a smooth boundary representation is obtained (see Fig 5.6d).

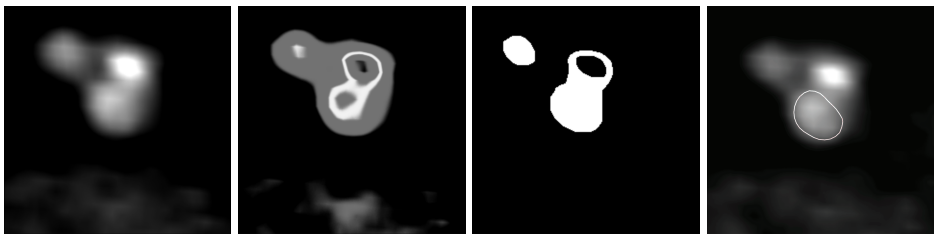

(a) (b) (c) (d)

Figure 5.6: A cross-sectional image of a randomly selected coronary artery, presenting a calcium lesion and a side branch. (a) Input image, (b) resulting image after applying a lumen likelihood function, (c) binarized image after lumen segmentation using graph cuts (lumen bright, background black), (d) the resulting lumen segmentation (in white) after kernel regression.

Stenosis detection and quantification

From the coronary artery lumen segmentation (per segment of the coronary artery tree), the cross-sectional area A_i of the vessel is computed at every position i along the vessel centerline, $i \in [1, n]$ with n being the number of positions along the centerline. The radius is then derived as $r_i = \sqrt{A_i/\pi}$.

To compute the degree of stenosis, the radius of a healthy vessel is needed as a reference. We estimated the radius $\hat{r}$ of the healthy vessel by applying a robust weighted Gaussian kernel regression (Debruyne et al., 2008) to the 1D function r describing the vessel radius along the centerline:

$$\hat{r}_i = \frac{\sum_{i'=1}^{n} N(i'|i, \sigma_i) w_{i'} r_{i'}}{\sum_{i'=1}^{n} N(i'|i, \sigma_i) w_{i'}} \quad , \tag{5.9}$$

where,

$$\begin{cases} w_i = N(r_i | r_i^{max}, \sigma_r) \\ r_i^{max} = \dfrac{\sum_{i'=1}^{n} N(i'|i, \sigma_{max}) r_{i'}}{\sum_{i'=1}^{n} N(i'|i, \sigma_{max})} \\ N(i'|i, \sigma) = \frac{1}{\sigma\sqrt{2\pi}} e^{-\frac{(i'-i)^2}{2\sigma^2}} \end{cases} \tag{5.10}$$

5.2.3 Parameter selection

Some of the parameters used in our method were optimized using the training datasets provided by the framework. For others, the values were chosen identical to our previous works the lower and upper scales for the multi-scale vesselness measure (V_x) used in Eq. 5.1 and in Eq. 5.3 were set to 0.8 mm and 2 mm, with 3 intermediate scales. The other parameters α, β, c (used in V_x), w_1, w_2, w_3, a_s and b_s (used in T_x) from Eq. 5.1 were taken from (Metz et al., 2009) and are presented in Table 5.1. The minimum and maximum scales for the medialness measure (M_x) used in Eq. 5.3 were set to 0.5 mm and 2 mm, the number of intermediate scale steps to 8 and the number of angles to 24. The value of ϵ in both equations was set to 0.0001. The value of T_{ca} in Eq. 5.2 was set to 200 GV. The CMPR images were generated at 0.5 mm slice spacing and with a cross-sectional area of 10×10 mm^2, and a voxel size of $0.1 \times 0.1 \times 0.5$ mm^3. The parameters used for lumen segmentation in Section 5.2.2 were taken from (Schaap et al., 2009b). The value of σ_s and δ in Eq. 5.4 were set to 0.5 and 0.01 respectively, σ_ϕ in Eq. 5.6 was set to 0.1. In Eqs. 5.9 and 5.10 of the stenoses detection/quantification, the parameter σ_x (corresponding to centerline longitudinal distance) was set to 8, σ_r (corresponding to radius) to 0.25, and σ_{max} to 200.

Table 5.1: Parameters used in computing the vesselness measure V_x and the threshold function T_x

α	β	c	w_1	w_2	w_3	a_s	b_s
0.5	0.4	230	0.99	0.10	0.10	1028 GV	965 GV

As QCA is the reference standard, it was observed from the training experiments that the CTA derived measure slightly overestimates the degree of stenosis in the mild stenotic regions. This is probably due to the fact that QCA measurements are made in 2D and our method quantifies the stenoses in 3D on the CTA image. Therefore, we investigated the possibility to improve the quantification measure, correcting for this bias. We performed a few pilot experiments and found out that improved stenoses quantification matching between CTA and QCA can be achieved by applying an off-set

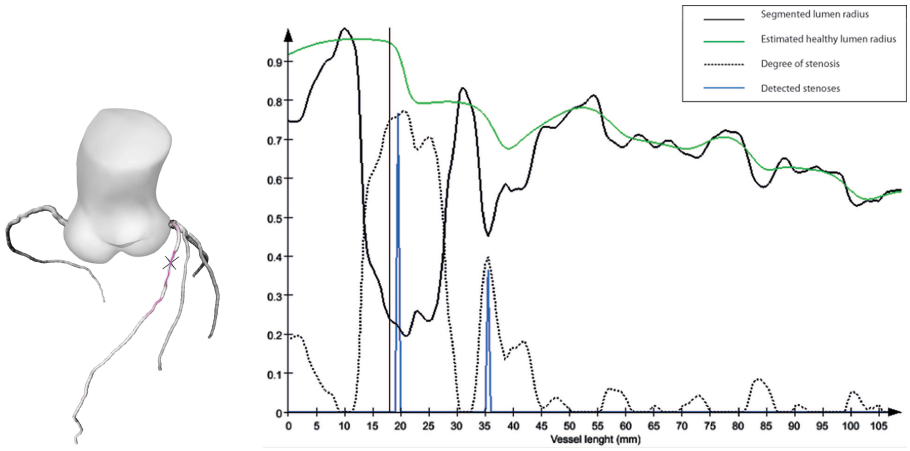

(a) (b)

Figure 5.7: Stenoses detection and quantification. (a) Shows the reconstructed lumen tree of a patient in which the red shade highlights narrowing of the lumen. (b) Various curves as a function of centerline position showing: the true radius (black), estimated radius (green), detected stenoses (blue) and the stenoses degree (black dotted). The cross on the stenosis in (a) corresponds to the vertical line at the 18 mm mark in (b). It can also be observed that two stenoses were detected and one of them was significant.

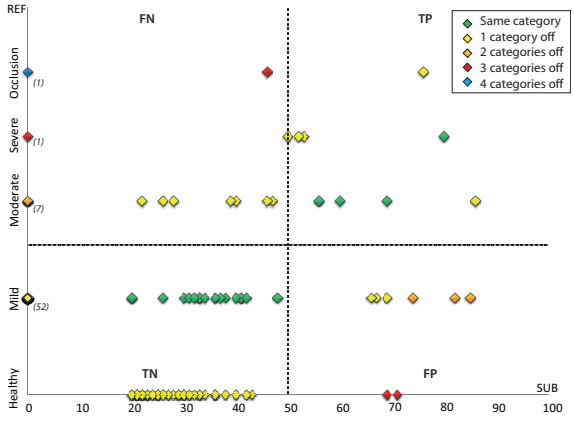

Figure 5.8: Stenoses detection and quantification. X-axis: our submission (SUB), y-axis: the reference data (REF) - Results obtained on the 18 training datasets after optimization of the parameters: 90% of the stenoses detected with our new method are quantified either in the correct risk category or in the adjacent risk category (yellow and green detections).

value of −20 (represented as %) to all lesions detected on CTA with a degree between 20% and 50%.

Our method also overestimates the degree of stenosis on CTA in case of highly calcified lesions, due to the blooming effect. We corrected the stenoses grade for due to blooming as follows:

$$\begin{cases} G'_{CTA} = G_{CTA} - 10, & \text{if } I(x) - F(x) \geq 500 \\ & \& \; G_{CTA} \geq 70\% \\ G'_{CTA} = G_{CTA}, & \text{otherwise} \end{cases}$$

where G'_{CTA} is the refined CTA degree of stenosis, G_{CTA} the initial one, and the condition selects severe stenosis close to dense calcified objects. The values used in the equation were obtained from the pilot experiments.

Using the above parameters, 90% of the training lesions detected by our method on CTA images were estimated in the correct or adjacent class (Fig 5.8).

5.3 Results

Table 5.2, 5.3 and 5.4 present the training and testing results of our method with respect to the performance of the three observers. The training set consists of 18 datasets and the testing set of 30 datasets.

Table 5.2: Detection - Our method's performances compared with the three observers; Sensitivity (Sens.), positive predictive value (PPV).

(%)	**Training**				**Testing**			
Method	**QCA**		**CTA**		**QCA**		**CTA**	
	Sens.	*PPV*	*Sens.*	*PPV*	*Sens.*	*PPV*	*Sens.*	*PPV*
Observer 1	72	49	92	57	86	40	83	61
Observer 2	76	66	82	73	75	51	70	81
Observer 3	52	68	63	74	64	43	66	60
Our method	48	63	37	56	29	24	21	23

The ability of a method to discriminate significant stenoses (i.e. stenoses ≥ 50%) from non-significant ones was evaluated. Table 5.2 shows the average results of our method and three observers for stenosis detection measures: sensitivity (Sens.) and positive predictive value (PPV). The results show that on the testing datasets our method obtains a QCA sensitivity of 29% and a PPV of 24%. With respect to CTA we obtain a sensitivity of 21% and a PPV of 23%. In general, our results are not as good as the averaged observers' performance (sensitivity of 75%, PPV of 45% on QCA; sensitivity of 73%, PPV of 67% on CTA). The ability of our method to discriminate significant stenoses from non-significant ones remains very limited. However, as

Table 5.3: Quantification - Our method's performances compared with the three observers; Absolute difference (Abs Diff), root mean square difference (RMS Diff).

	Training			Testing		
Method	**QCA**		**CTA**	**QCA**		**CTA**
	Abs Diff (%)	*RMS diff (%)*	*Weighted* κ	*Abs Diff (%)*	*RMS diff (%)*	*Weighted* κ
Observer 1	29.7	35.1	0.71	30.1	35.2	0.74
Observer 2	25.5	31.8	0.84	31.1	36.5	0.77
Observer 3	29.1	35.1	0.73	30.6	36.9	0.73
Our method	26.3	34.8	0.37	31.0	39.3	0.29

Table 5.4: Segmentation - Our method's performances as compared with the observers; Diseased (D) / Healthy (H) segments, dice similarity index (Dice), mean surface distance (MSD), maximum surface distance (MAXD)

	Training						Testing					
Method	**Dice** (%)		**MSD** (mm)		**MAXSD** (mm)		**Dice** (%)		**MSD** (mm)		**MAXSD** (mm)	
	D	*H*	*D*	*H*	*D*	*H*	*D*	*H*	*D*	*H*	*D*	*H*
Observer 1	74	79	0.26	0.26	3.29	3.61	76	77	0.24	0.24	2.87	3.47
Observer 2	66	73	0.31	0.25	2.70	3.00	64	72	0.34	0.27	2.82	3.26
Observer 3	76	80	0.24	0.19	3.07	3.25	79	81	0.23	0.21	3.00	3.45
Our method	66	70	0.37	0.32	2.49	3.04	65	68	0.39	0.41	2.73	3.20

compared to the current state-of-the art algorithms, our method ranks fourth out of 12 submissions on the test set.

Table 5.3 shows the average results of our method and three observers for stenosis quantification measures. Despite the poor performance of our method to discriminate the non-significant stenoses from significant ones (hard threshold at 50%), our method was able to quantify the degree of stenosis as compared to the QCA with an accuracy comparable to the experts. The quantification agreement obtained with the proposed approach as compared to the CTA reference was fair. It should be pointed out that, on the training set ($\kappa = 0.37$) 90% of the lesions were estimated in the correct or adjacent class. An averaged absolute difference of 31%, an RMS difference of 39%, and a weighted Kappa value $\kappa = 0.29$ were obtained on the test set. The manual observers (on average) achieved an averaged absolute difference of 31%, an RMS difference of 36% and $\kappa = 0.75$. Our method ranks second out of nine other submissions on the test set.

Table 5.4 shows the average results of our method and three observers for coronary artery lumen the similarity between our method and the observers were measured by the Dice similarity index (Dice). The distance between the segmentations was quantified by the root mean squared distance (RMSD) and maximum distance (MAXD). Overall, the Dice and RMSD values obtained on healthy vessel segments were better than the values obtained on diseased segments. The Dice and RMSD were worse than the averaged observers' performance, but the MAXD was better. Fig 5.9 present a few examples on longitudinal view of various coronary artery segments. In comparison to those obtained by one of the three manual observers and the one obtained using our previous approach (Shahzad et al., 2012a) (i.e. without the calcium suppression step), It can be seen that our segmentation results are very close to the ones obtained by the manual method. Our method ranks second out of six other submissions.

5.4 Discussion

5.4.1 Evaluated algorithm

Although the coronary artery lumen can be automatically segmented with a precision similar to the experts, there is still room for improvement for our stenoses detection/quantification approach. In the current approach, the stenoses are quantified solely based on the diameter profile of the segmented lumen. Therefore, in case of diffuse disease or long stenoses, the degree of luminal narrowing is generally underestimated. As the method does not detect a lot of false positives (41 FP's over 48 datasets), it could be used in clinical practice for triage or as a second reader to assist the radiologist.

The relatively low value of the Kappa statistic in the CTA stenoses quantification measure may either be caused by a high number of false positives/negatives or by a high number of lesions reported with more than one grade difference as compared to the CTA reference, or by the linear weights which heavily penalize misclassifications. On the training set, a weighted Kappa value of 0.37 was obtained, and only 10% of the

stenoses had a quantification error of more than one grade (Fig 5.8). This highlights that the linearly weighted Kappa is very sensitive to misclassification.

The majority of the stenoses detected with our approach were quantified with an error of only one grade, and most of the misclassifications occured between the mild (20-50%) and moderate (50-70%) grades. As 50% is the hard threshold used to discriminate between significant and non-significant lesions, accurate detection of significant stenoses remains a challenge. Considering that our method maybe used for triage of patients or as a second reader, the use of a third group "may be significant", in addition to the significant and non-significant group could be considered, to which all the borderline (40-60% for instance) detected stenoses are assigned. The radiologists would then have to inspect in more details those stenoses to make a final decision.

The results show that the additional centerline refinement step consisting of calcium suppression from the cost image improves the segmentations compared to our previous approach (Shahzad et al., 2012a). Previously, the centerline was attracted to the calcified plaque and therefore, the plaque rather than the vessel was segmented. A simple thresholding technique for removing calcium would not work very efficiently on CTA scans as the intensity of the contrast material between different patients and different vessels is quite dissimilar (Rybicki et al., 2008). Error in estimating a global threshold value for a patient would result in either completely missing medium/small calcium lesions or over segmenting the calcium lesion by including the surrounding contrast material. We chose fitting the intensity profile with a cubic polynomial based on the pilot experiments done on the training data set. Cubic polynomial fitting provided us with a good estimate for a threshold to differentiate between the background contrast intensity and the calcium objects. Higher order polynomials gave us a very smooth fit, making it difficult to estimate the threshold value to separate contrast material from calcium peaks.

The segmentations of the current approach are in better agreement with the observer's ones. The issue with calcified plaques is not completely solved. We were able to prevent the centerlines from running into calcified objects, but for highly calcified regions (Fig 5.9(d)(e), the method may have issues finding the correct lumen. In such cases, our refined centerline tends to run at the very outer border of the lumen, and the derived segmentation is of minimal radius size. However, in such extreme cases, it is not always clear how to manually segment the lumen either, and the inter-observer variability is therefore also high.

A limitation of our centerline extraction step is the need to initialize the start and the end points of the coronary arteries. *The Coronary Artery Stenoses Detection and Quantification Evaluation Framework* organizers provided the participants with the start and the end points of all the vessels that were of interest. For new datasets, the user has to annotate the start and the end point. The initialization process can be simplified by automatically defining the start point in the aorta using the method proposed by (Metz et al., 2009). Automatic processing can be further improved by finding the end points using information from an atlas-based coronary density estimate (Shahzad et al., 2010). However, our method can also be used in combination with centerlines that have been automatically obtained (Kitamura et al., 2012; Yang et al., 2012; Goldenberg et al., 2012; Zambal et al., 2008). The

automatically obtained centerline could be used as the initial centerline in our method and subsequently followed by calcium suppression, centerline refinement, lumen segmentation, and stenoses detection and quantification.

5.4.2 Comparison with other evaluated algorithms

Nine of the eleven other evaluated algorithms were developed following a workflow similar to ours, consisting of 1) the computation of lumen segmentation, either directly from the input CTA image or using previously extracted centerlines, and 2) the subsequent detection (and quantification) of coronary artery stenoses. Only one of the evaluated algorithms does not involve lumen segmentation, but is using features extracted from the CTA image to detect plaques (Duval et al., 2012).

To detect and quantify lesions, six out of the nine algorithms estimated a healthy lumen radius by applying various regression approaches to the segmented lumen radius profile (linear for the approaches of (Cetin and Unal, 2012; Broersen et al., 2012; Flórez-Valencia et al., 2012; Mohr et al., 2012; Öksüz et al., 2012), second-order for the approach of (Eslami et al., 2012), robust for the approach of (Shahzad et al., 2012a)). Only in the algorithm proposed by (Wang et al., 2012), the outer vessel wall was segmented from the CTA image. The remaining two proposed algorithms analyze intensity and geometry features (Lor and Chen, 2012; Melki et al., 2012).

Given an accurate lumen segmentations, our approach outperforms the algorithms proposed by (Broersen et al., 2012) and (Wang et al., 2012) in the quantification stage, and achieves the best (though fair) quantification agreement as compared to the CTA reference standard. The results thus suggest that robust regression is a good approach to quantify lesions following lumen segmentation. However, there is still room for improvement. Refinement of the stenosis grades using additional morphological and intensity features may lead to improvements in both the detection and quantification steps.

5.5 Conclusions

We presented a method to automatically detect and quantify coronary arteries stenoses, based on coronary artery lumen segmentation. The current results show that the coronary artery lumen can be automatically segmented with a precision similar to the experts. Quantification of the stenoses with respect to the QCA measure can also be performed close to those obtained by the observes. However, automatic discrimination between significant and non-significant lesions in CTA remains a challenge.

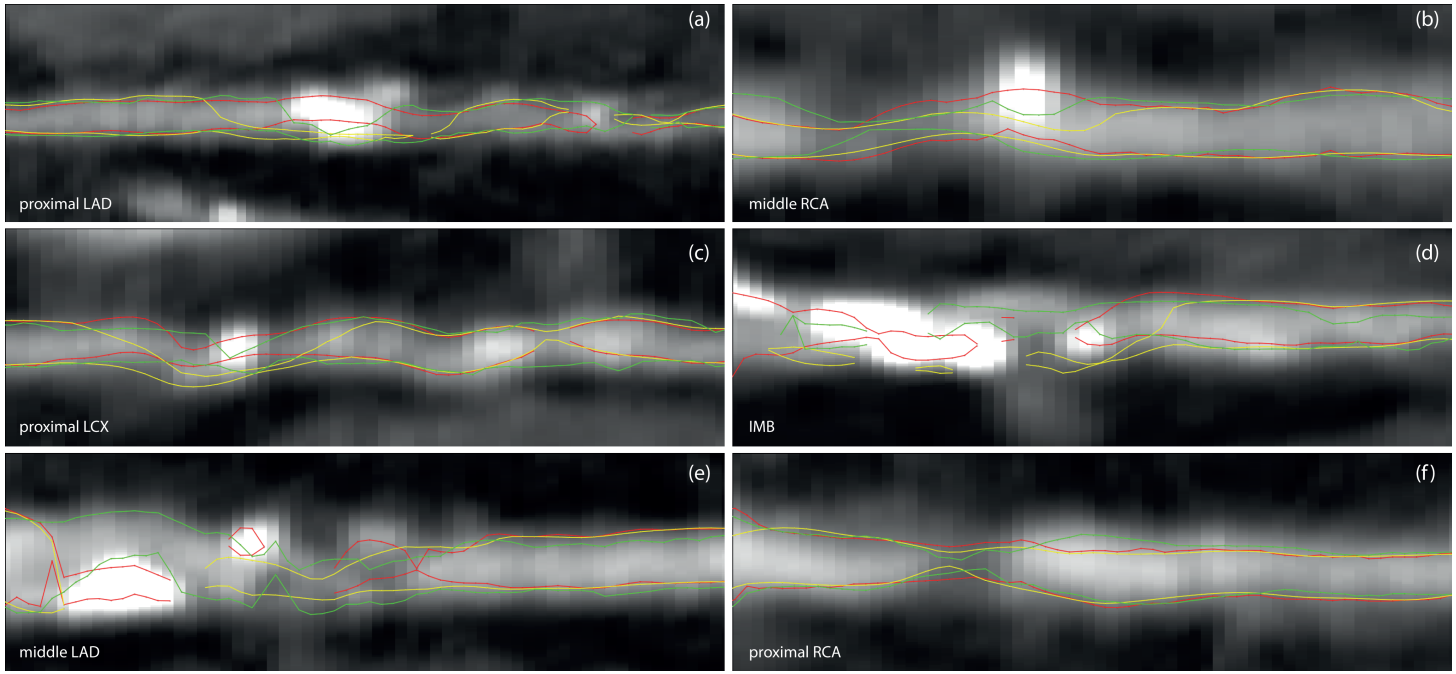

Figure 5.9: Coronary artery lumen segmentation examples in CMPR that are based on the manually annotated centerlines. Our previous method (method without the calcium suppression step in the centerline refinement) (red), proposed method (yellow), one of the observers (green). (a)(b)(c) Cases where our method (with the calcium suppression step in the centerline refinement) achieves segmentation similar to the observer. (d) Case where the method avoids the calcified plaque and the observer segmented the other side of the plaque. (e) Case where an issue with large calcified plaque remains. (f) Example of segmentation of a coronary segment presenting a soft plaque. Discontinuities in the segmentation, such as the segmentations in (d) and (e), are a visualization artefact: the segmentation runs out of the CMPR surface.

6

Additional diagnostic value of integrated analysis of cardiac CTA and SPECT/MPI using the SMARTVis system in patients with suspected coronary artery disease

This chapter is based on the manuscript:
Additional diagnostic value of integrated analysis of cardiac CTA and SPECT/MPI using the SMARTVis system in patients with suspected coronary artery disease,
H.A. Kirişli*, V. Gupta*, **R. Shahzad*** *(* shared first authorship)* I. Al Younis, A. Dharampal, R.J. van Geuns, A.J. Scholte, M.A. de Graaf, R.M.S. Joemai, K. Nieman, L. van Vliet, T. van Walsum, B.P.F. Lelieveldt and W.J. Niessen,
Journal of Nuclear Medicine, in press, 2013..

Abstract

Purpose CT angiography (CTA) and SPECT myocardial perfusion imaging (SPECT/MPI) are complementary imaging techniques to assess coronary artery disease (CAD). Spatial integration and combined visualization of SPECT/MPI and CTA data may facilitate correlation of myocardial perfusion defects and subtending coronary arteries, and thus offer additional diagnostic value over either stand-alone or side-by-side interpretation of the respective data sets from the two modalities. In this study, we investigate the additional diagnostic value of a software-based CTA/SPECT/MPI image fusion system, over conventional side-by-side analysis, in patients with suspected CAD.

Methods Seventeen symptomatic patients who underwent both CTA and SPECT/MPI examination within a 90-day period were included in our study; seven of them also underwent an invasive coronary angiography (ICA). The potential benefits of the Synchronized Multimodal heART Visualization (SMARTVis) system in assessing CAD were investigated through a case-study, involving four experts from two medical centers, where 1) a side-by-side analysis using structured CTA and SPECT reports, and 2) an integrated analysis using the SMARTVis system in addition to the reports, were performed.

Results The fused interpretation led to a more accurate diagnosis, reflected in an increase of the individual observers' sensitivity and specificity to correctly refer for invasive angiography eventually followed by revascularization. For each of the four observers, the sensitivity improved from (50%, 60%, 80%, 80%) to (70%, 80%, 100%, 100%), and the specificity from (100%, 94%, 83%, 83%) to (100%, 100%, 94%, 83%) respectively. Additionally, the inter-observer diagnosis agreement increased from 74% to 84%. The improvement was primarily found in patients presenting CAD in more vessels than the number of reported perfusion defects.

Conclusions Conclusions Integrated analysis of cardiac CTA and SPECT/MPI using the SMARTVis system results in an improved diagnostic performance.

6.1 Introduction

Coronary artery disease (CAD) is a major cause of death worldwide (Roger et al., 2012). Invasive coronary angiography (ICA) is regarded as the reference standard imaging technique for diagnosing CAD (Levine et al., 2011); it enables determining the location, the extent, and the severity of the vessel obstructions. Computed tomography coronary angiography (CTA) imaging is rapidly gaining clinical acceptance (Weustink and de Feyter, 2011); it non-invasively provides high-resolution images of the cardiac and coronary artery anatomy and allows assessment of the presence, extent and type of coronary stenoses. Still, neither CTA nor ICA provides information on the functional implications of detected stenoses; a functional test may therefore be required to evaluate presence and extent of myocardial ischemia. Single photon emission computed tomography myocardial perfusion imaging (SPECT/MPI) is widely used to noninvasively assess reversible myocardial ischemia. In conventional side-by-side analysis, integration of CTA and SPECT/MPI findings is mentally performed by using a standardized myocardial segmentation model that allocates each myocardial segment to one of the three main coronary arteries (Kalbfleisch and Hort, 1977; Cerqueira et al., 2002). However, individual coronary anatomy does not always correspond with the standardized myocardial distribution. In a study of 50 patients, Pereztol-Valdes et al. (Pereztol-Valdés et al., 2005) demonstrated that only nine of the 17 AHA-segments are fed by a single coronary artery, while the other eight segments may be fed by more than one coronary artery. Spatial integration and combined visualization of anatomical and functional data may facilitate correlation of myocardial perfusion defects and subtending coronary arteries, and thus offer additional diagnostic value over either stand-alone or side-by-side interpretation of the respective data sets (Peifer et al., 1990; Schindler et al., 1999; Nakaura et al., 2005; Bax et al., 2007; Gaemperli et al., 2007b,a, 2009; Santana et al., 2009; Slomka et al., 2009; Kaufmann, 2009; Sato et al., 2010). The concept of three-dimensional (3D) fusion imaging to improve the assignment of epicardial lesions to stress-induced ischemia originated from the study of Peifer et al. (Peifer et al., 1990), and subsequently by Schindler et al. (Schindler et al., 1999). In the latter, 3D models of the coronary artery tree generated from coronary angiograms were combined with 3D models of the epicardial surface generated from SPECT/MPI.

According to more recent studies (Nakaura et al., 2005; Bax et al., 2007; Gaemperli et al., 2007b,a, 2009; Santana et al., 2009; Slomka et al., 2009; Kaufmann, 2009; Sato et al., 2010), hybrid cardiac imaging systems, physically combining the CT and SPECT/PET acquisition, and software allowing fusion of images obtained separately, are promising non-invasive techniques to assess CAD. It is expected that such systems will gain in popularity in the future, to reduce the number of patients unnecessarily referred for ICA examination. Here, we present the software-based Synchronized Multimodal heART Visualization (SMARTVis) fusion system, which allows comprehensive analysis of cardiac multimodal imaging data for assessment of CAD. The aim of the present study is to investigate whether integrated analysis of cardiac CTA and SPECT/MPI with the SMARTVis system improves diagnostic performance, compared with side-by-side interpretation.

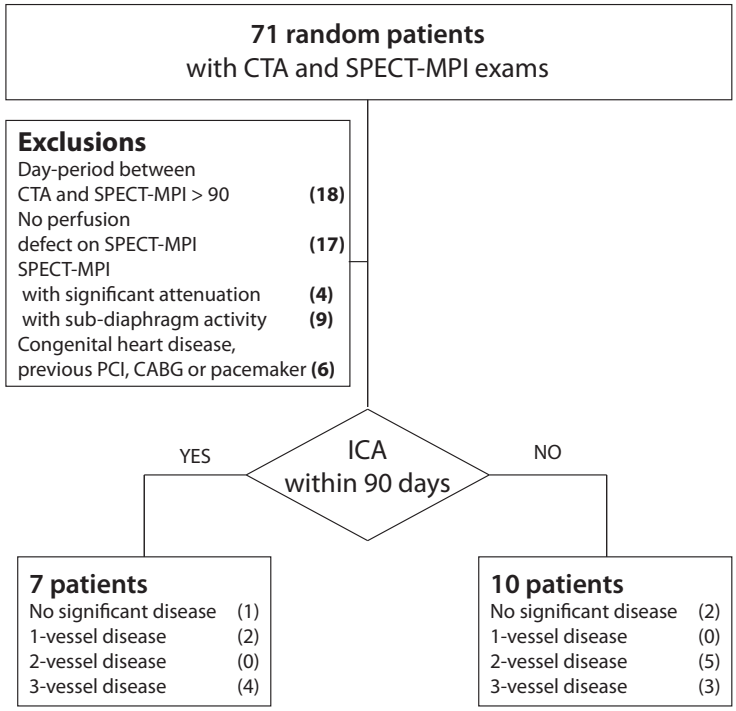

Figure 6.1: Patient's selection and exclusion criteria.

6.2 Materials and methods

6.2.1 Study population

Seventy-one patients who underwent cardiac CTA and SPECT/MPI at the Leiden University Medical Center (Leiden, The Netherlands) were randomly selected. After applying exclusion criteria (Figure 6.1), seventeen patients were included in our study; images from an invasive coronary angiography (ICA) procedure performed within a 90-day period were available for seven of them. Patient characteristics are presented in Table 6.1. The institutional review board approved this retrospective study and the requirement to obtain informed consent was waived.

6.2.2 SPECT/MPI

Image acquisition **-** SPECT/MPI was performed using a two-day protocol starting with the stress acquisition. The patients underwent bicycle ergometry or, when contraindications were present, adenosine or dobutamine infusion to induce stress. The radioisotope (500 MBq Tc-99m tetrofosmin) was injected either at peak exercise, three minutes after starting adenosine perfusion or at peak heart rate during dobutamine infusion. For both stress and rest scans, the images were acquired one

Table 6.1: Patient characteristics (N=17)

Characteristics	
Age (y)	61 ± 9
Males (N)	15 (90%)
Body Mass Index (kg/m^2)	22.8 ± 4.4
Calcium score (Agatston)	$494(IQR85-1319; range0-4797)$
Medical history *based on CTA*	**N (%)**
No significant disease	3(17)
1-vessel disease	2(12)
2-vessel disease	5 (29)
3-vessel disease	7 (42)
Cardiovascular risk factors	**N (%)**
Current smoker	7(42)
Hypertension	11(65)
Diabetes mellitus	14(82)
Hypercholesterolemia	12(70)
Family history of CVD	4(24)
Imaging	**mean ± std [min,max]**
Day-period between CTA and SPECT-MPI	$31 \pm 31[1, 79]$
Day-period between CTA and ICA (N=7)	$45 \pm 30[8, 85]$

hour after radioisotope injection. A triple-headed camera system (Toshiba CGA 9300, Tokyo, Japan) and a low-energy high-resolution collimator were used. ECG gating was performed at 16 frames per cardiac cycle, with a tolerance window of 50%. No attenuation or scatter correction was applied.

Image interpretation **-** An experienced nuclear physicist, blinded to both CTA and ICA results, analyzed the scans using the Corridor4DM software package (Version 6.1, INVIA Solutions, Ann Arbor, MI, USA) (Ficaro et al., 2007). SPECT/MPI images were interpreted using oblique slices, polar maps and quantitative/functional values. The SPECT/MPI interpretation was summarized into a report, following guidelines presented in (Folks, 2002) the observer graded each of the 19 myocardial segments as being normal (no perfusion defect) or abnormal (reversible or fixed defects), and indicated the extent of myocardial infarction or ischemia.

6.2.3 Computed Tomography Angiography

Image acquisition **-** Five patients were scanned using a 64-slice CT scanner (Aquilion 64, Toshiba Medical Systems Corporation, Otawara, Japan) and the remaining twelve patients were scanned using a 320-slice CT scanner (Aquilion ONE, Toshiba Medical Systems Corporation, Otawara, Japan). In case the heart rate was higher than 65 beats/min, additional oral β-blockers (metoprolol 50 mg, single dose, one hour before scan) were provided when tolerated. A prospectively triggered coronary calcium scan

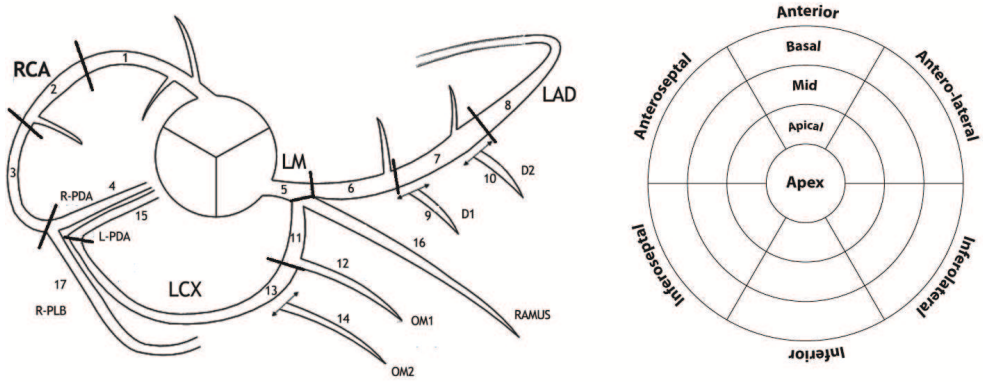

Figure 6.2: **(a)** Coronary segmentation diagram. Axial coronary anatomy definitions derived, adopted, and adjusted from Austen et al. (1975). Left main (LM), left anterior descending artery (LAD), right coronary artery (RCA), left circumflex artery (LCX), diagonal branch (D), obtuse marginal branch (OM), posterior descending artery (PDA), posterior lateral artery (PL) and intermediate branch (IMB). Proximal (p), middle (m), distal (d). 1: p-RCA, 2: m-RCA, 3: d-RCA, 4: PDA, 5: LM, 6: p-LAD, 7: m-LAD, 8:d-LAD, 9: D1, 10: D2, 11: p-LCX, 12: OM1, 13: m-LCX, 14: OM2, 15: d-LCX, 16: IMB, 17: PL. **(b)** 19 myocardial segments model used to interpret the SPECT-MPI.

(non-contrast CT scan) was performed before CTA acquisition. CTA images were acquired with a collimation of 64×0.5 mm (resp. 320×0.5 mm), a tube rotation time of 400 ms, and tube current of 300 mA at 120 kV for patients with normal posture (BMI ≤ 30 kg/m^2). If a patient had a higher body mass index, tube current was increased to 350 or 400 mA at 135 kV. The acquisition of imaging was prospectively triggered at 75% of the R-to-R interval. Between 80 and 110 ml non-ionic contrast material (Iomeron 400H, Bracco Atlanta Pharma, Konstanz, Germany) was administered with a flow rate of 5 ml/sec depending on the total scan time. The timing of the scan was determined using automated detection of peak enhancement in the aortic root. Acquisition was conducted during an inspiratory breath hold of approximately 10 s.
Image interpretation - A single experienced reader, blinded to both SPECT/MPI and ICA results, analyzed the scans using the syngo.via workstation (Siemens Healthcare, Erlangen, Germany). CTA images were interpreted using trans-axial image stacks and (curved) multi-planar reformatted images (MPR/cMPR). The CTA interpretation per coronary segment (AHA Model (Austen et al., 1975)) was summarized into a report, following guidelines presented in (Raff et al., 2009): the observer reported the stenosis location (origin, proximal, mid, distal, end), the stenosis severity (mild, moderate, severe, occluded), the stenosis plaque type (non-calcified, mixed, calcified).

6.2.4 Quantitative Coronary Angiography

ICA was performed accordingly to standard medical practice. One experienced cardiologist, unaware of the CTA and SPECT-MPI scoring results, performed quantitative coronary angiography (QCA) on the seven available angiograms. All coronary segments were identified and analyzed using the modified 17-segment AHA classification (Figure 6.2). Segments were visually classified as normal (smooth parallel or tapering borders, visually $\leq$ 20% narrowing) or as having coronary obstruction (visually $\geq$ 20% narrowing); the stenoses in these last segments were quantified by a validated QCA algorithm (Reiber et al., 1985) (CAAS, Pie Medical, Maastricht, The Netherlands). Stenoses were evaluated in the worst (available) angiographic view and classified as significant if the lumen diameter reduction exceeded 50%.

6.2.5 SMARTVis : a software-based CTA/SPECT-MPI fusion system

In this work, we extend the **S**ynchronized **M**ultimodal he**ART** **Vis**ualization (SMARTVis) system introduced in (Kirişli et al., 2012) to fuse CTA with SPECT-MPI nuclear myocardial perfusion imaging. An overview of the CTA and SPECT-MPI processing and fusion is given on Figure 6.3. The SMARTVis system provides comprehensive 2D and 3D fused visualizations of the anatomical and functional information for relating coronary stenoses and perfusion defect regions (Figure 6.4). The coronary artery tree extracted from CTA can be projected onto the 2D stress/rest polar map (PMAP), and, similarly, the perfusion information visualized on a 3D stress/rest PMAP can be fused with a 3D model of the heart and its coronary artery tree. Furthermore, the SMARTVis system provides a list of automatically detected and quantified coronary artery stenoses (Shahzad et al., 2012a). To further assist the user in assigning a culprit lesion to a specific perfusion defect, a (distance-based) estimation of the patient-specific coronary perfusion territories is provided. Last, the 2D and 3D PMAP viewers are synchronized with the CTA stenosis findings and images.

Beside the fused visualization, the SMARTVis system provides the opportunity to inspect 1) the non-contrast CT image and its automatically calculated per-vessel calcium scores (Shahzad et al., 2012b), 2) the CTA images and its automatically detected stenoses, and 3) the SPECT-MPI polar maps and left ventricular function curves. During the evaluation, only the fused visualizations were used by the observers.

6.2.6 Study design

The additional diagnostic value of the SMARTVis system to assess CAD was investigated through a case-study evaluation. An overview of the study design is presented in Figure 6.5.

First, structured reports were created for CTA and SPECT-MPI, according to the guidelines presented in Sections 6.2.3 and 6.2.2. Also, QCA analysis was performed for 7 patients. A treatment strategy (i.e. medical treatment or revascularization of specific coronary segment(s)) was further derived from QCA and SPECT-MPI findings

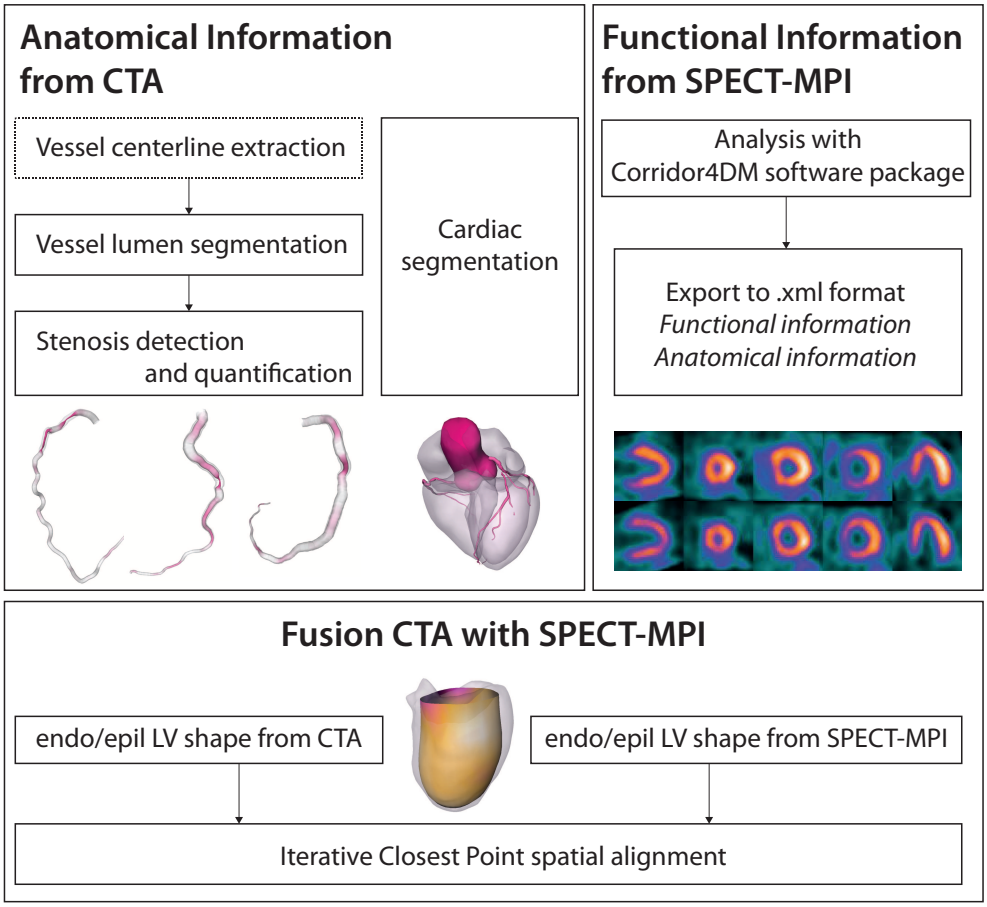

Figure 6.3: Overview of image processing performed on CTA and fusion of CTA/SPECT-MPI. The dashed box corresponds to semi-automatic process, while the solid boxes correspond to fully automatic processes. Coronary artery stenoses were detected and quantified on CTA using the method presented in (Shahzad et al., 2012a); cardiac chamber shapes were obtained from CTA by applying method presented in (Kirişli et al., 2010). The SPECT-MPI left ventricle shape was automatically provided by the Corridor4DM software, as well as landmark points indicating the septal and apical positions. LV shapes and landmark points were subsequently used to align CTA and SPECT-MPI data by applying iterative closest point algorithm.

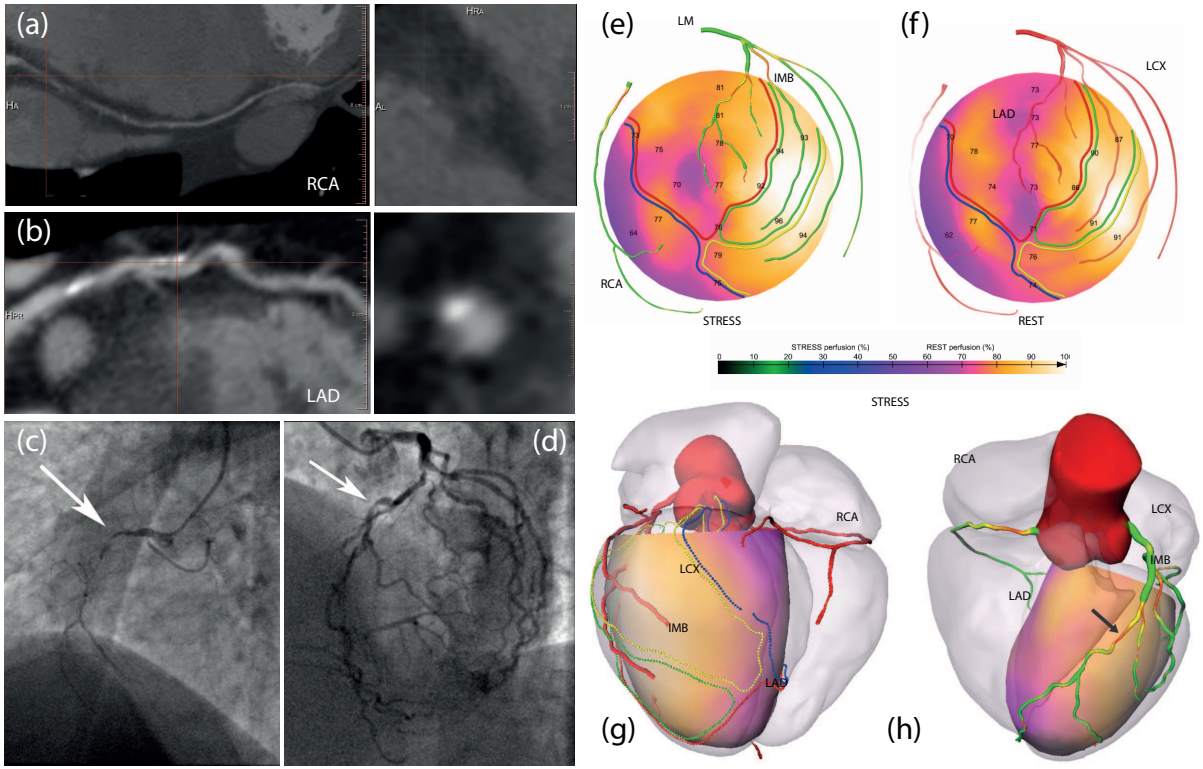

Figure 6.4: Example of patient 16 (male, 59 y.o.), who presents fixed perfusion defects in the inferior and anterior wall on SPECT-MPI and suspected triple-vessel disease on CTA. A complete occlusion was detected in the proximal RCA **(a)** and a moderate mixed plaque was detected in the middle LAD **(b)**. The QCA reveals a complete occlusion in proximal RCA **(c)** and a 50% stenosis in the middle LAD **(d)**. Comprehensive visualizations proposed in the SMARTVis system - **(e)(f)** 2D stress and rest polar maps (PMAP) fused with projection of the coronary tree extracted from CTA. On the stress PMAP **(e)**, coronary arteries are color coded with the degree of stenosis; on the rest PMAP **(f)**, coronary arteries are coded with the distance to the epicardium: the more transparent the artery, the further it is from the epicardium. Patient-specific perfusion territories are also projected: LAD in red, LCX in yellow, MO in green and RCA in blue. **(g)(h)** 3D model of the heart and coronary artery tree extracted from CTA fused with 3D stress PMAP.

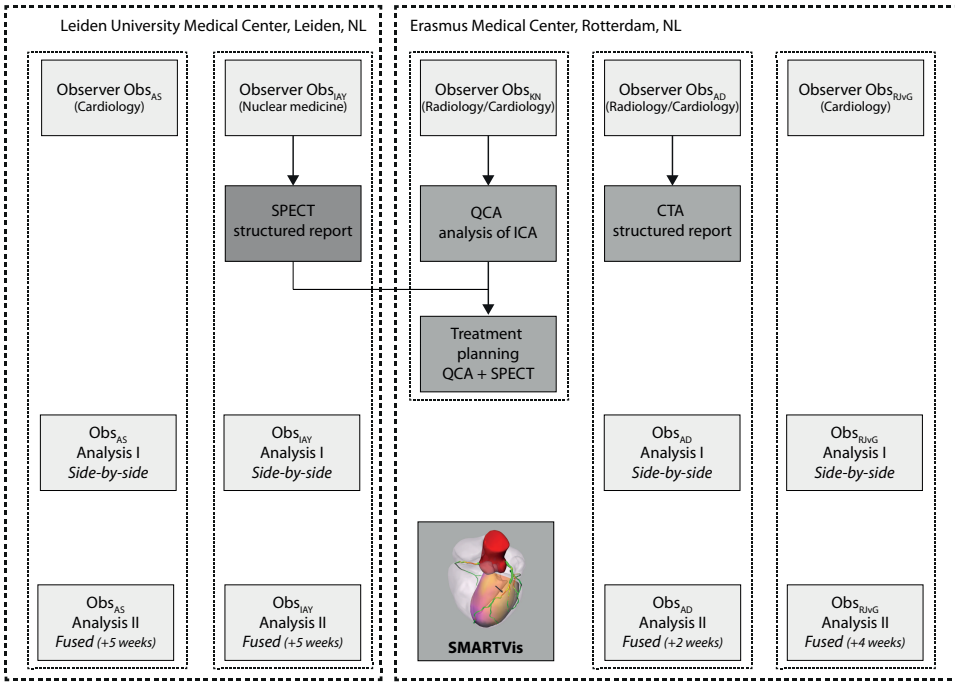

Figure 6.5: Overview of the evaluation study design. First, structured reports were created from CTA (ObsAD) and SPECT-MPI (ObsIAY), and QCA analysis was performed on the 7 available ICA. Treatment planning was performed for those 7 patients, based on QCA and SPECT-MPI findings. Second, four experts from two medical centers examined 17 patients with suspected CAD and performed 1) a side-by-side analysis, using structured CTA and SPECT-MPI reports, and 2) an integrated analysis, using the SMARTVis system in addition to the CTA and SPECT-MPI reports. Both analyses were performed with an interval of 2 to 5 weeks.

and served as reference standard. As the guidelines recommend proof of ischemia prior to revascularization of coronary stenoses (Levine et al., 2011), the expert considered medical therapy indicated for significant lesions detected on QCA which resulted in infarction and no further complaints.

Subsequently, four experts from two medical centers (Erasmus Medical Center, Rotterdam, The Netherlands; Leiden University Medical Center, Leiden, The Netherlands) took part in the study. All observers were experienced with both CTA and SPECT-MPI. During individual sessions, they examined the 17 selected patients and performed 1) a side-by-side analysis, using structured CTA and SPECT-MPI reports, and 2) an integrated analysis, using the SMARTVis system in addition to the CTA and SPECT-MPI reports. The side-by-side analysis was performed 2 to 5 weeks prior to the integrated analysis, and the patients were analyzed in a different order, to minimize

the chance of recalling patient cases. The SMARTVis system was introduced by the first author to the observers during individual training sessions, using images of one of the excluded patient datasets. The tool was then operated by the clinical expert during the evaluation, under the supervision of the first author.

For each of the 17 coronary artery segments that presented at least one $\geq$ 20% stenosis on CTA, the observer had first to indicate the correlation between stenoses and perfusion defects. The stenoses present in the considered coronary segment could either be related to a myocardial region presenting a perfusion defect on SPECT-MPI, or be considered as hemodynamically not significant (i.e. not inducing a perfusion defect). Subsequently, the observer had to indicate the most appropriate therapeutic decision: medical therapy or revascularization of specific coronary segment(s).

6.2.7 Analysis

The revascularization decision strategy and target vessel selection of each observer were compared with both the other observer's decisions and the reference decision, derived from interpretation of QCA and SPECT-MPI. The diagnostic performance of CTA, SPECT-MPI and their fusion were compared on a per-vessel basis to determine the therapeutic decision agreements, as well as the sensitivity and specificity.

For all 17 patients, an inter-observer therapeutic decision agreement percentage was computed per patient p as follows:

$$Agreement^{p}_{inter-observer} = \frac{1}{4} \times \sum_{v=1}^{4} \omega_v \text{ and } \omega_v = \begin{cases} 100 & \text{if all observers agree} \\ 50 & \text{if 3 observers agree} \\ 0 & \text{otherwise} \end{cases}$$

with v the main arteries (RCA, LAD, LCX, IMB) and ω_v the observer therapeutic agreement for vessel v.

For the subset of 7 patients who underwent ICA, a therapeutic decision agreement percentage with respect to the QCA/SPECT-MPI decision was computed per patient p as follows:

$$Agreement^{p}_{QCA} = \frac{1}{4} \times \frac{1}{4} \sum_{obs=1}^{4} \sum_{v=1}^{4} \omega_{obs,v} \text{ and } \omega_{obs,v} = \begin{cases} 100 & \text{if, for vessel v, obs agree with the QCA/SPECT/MPI decision} \\ 0 & \text{otherwise} \end{cases}$$

with the QCA/SPECT-MPI decision.
Also, the sensitivity and specificity for revascularization of a coronary artery were computed.

6.3 Results

First, the results of the mono-modality analyses are reported (Sections 6.3.1 to 6.3.3). Subsequently, we report on inter-observer agreement and agreement with the reference standard (combined QCA/SPECT-MPI) for the conventional side-by-side analysis (Section 6.3.4), and the integrated analysis (Section 6.3.5), respectively. Finally, we compare the performance of integrated analysis of fused CTA/SPECT-MPI with the side-by-side analysis (Section 6.3.6).

Table 6.2: Findings from CTA, SPECT-MPI and ICA for the 17 patients, and inter-observer agreement results (+:improvement, =:same, -:worse) when performing fused interpretation with the SMARTVis system in comparison of side-by-side interpretation.

Patient	Sex	Age	CTA findings		SPECT-MPI findings		QCA findings	CTA	SPECT-MPI	Inter-obs
			Agatston score	≥ 50% stenosis	Reversible	Fixed	≥ 20% stenosis	suspected	suspected	(+,=,-)
1	M	46	60.6	-		inferior	NA	no	single	=
2	M	55	9.9	-	Anterior-Anteroseptal mid	Inferior-Inferolateral mid-apical	-	no	double	=
3	M	63	15.6	-		Anterior + Anterolateral + Apex Inferior + Inferoseptal	NA	no	double	=
4	M	70	1932.5	8		Inferior + Inferolateral apical	8(100%)	single	single	=
5	M	53	0	6,14	Anteroseptal mid Inferolateral basal-mid		NA	double	double	+
6	M	59	1676.9	3,10,12,13,14	Anterior Antero/Infero-lateral	Inferior + Inferoseptal	NA	triple	triple	-
7	M	65	315.4	6,13,16	Anterior basal-mid Antero/Infero-lateral apical Antero/Infero-septal basal	Inferior	NA	double	triple	+
8	M	61	819.6	11	Anterior basal-mid Inferior mid-apical		5(38%),6(46%), 11(63%)	single	double	+
9	M	60	493.8	4,12,13,16	Antero/Infero-lateral apical		NA	double	single	=
10	F	81	NA	2,4,16,17		Anterior + Anteroseptal	NA	double	single	+
11	M	68	962.3	1,6,8,9	Anterolateral mid		NA	double	single	+
12	M	60	373.8	1,2,6,7,14		Inferior	1(52%) 5(26%), 7(41%) 12(38%), 14(58%)	triple	single	+
13	M	73	2840.5	1,2,3,7,8,9,10,11,12		Inferior mid-apical	NA	triple	single	=
14	F	49	109.3	4,7,8,9,13	Anterior apical		NA	triple	single	-
15	M	56	4797.4	3,4,8,9,11,12,13	Anterolateral basal	Inferior	3(53%), 12(51%), 13(70%)	triple	double	=
16	M	59	NA	1,2,6,7,9,12,16		Inferior + Inferoseptal Anterior + Anteroseptal	1(100%) 6(50%)	triple	double	+
17	M	58	727.8	4,7,8,9,11,13,16	Antero/Infero-lateral basal-mid	Inferior + Inferoseptal	1(40%), 2(76%) 7(46%) 13(70%), 16(58%)	triple	double	=

6.3.1 SPECT-MPI findings

Ten of the patients showed a reversible perfusion defect (58%), twelve had a fixed perfusion defect (70%), and five patients (30%) revealed a mixed perfusion defect. Eight patients (47%) showed a perfusion defect in a single coronary territory, seven (41%) in two of them, and two (12%) in all three of territories. The exact locations of the perfusion defects are listed in Table 6.3.

6.3.2 CTA findings

Image quality was excellent in 12 patients (70%) and moderate in 5 patients (30%). The median Agatston score was 494 (IQR 85-1319; range 0-4797); 4 patients (24%) had a calcium score above 1000. In total, 263 segments were evaluated and significant stenoses were present in 66 of them (25%). The remaining 197 segments (75%) were normal or contained only non-significant stenoses ($\leq$ 50%). Among all segments, eighteen coronary segments (7%) were qualified as blurred and six segments (2%) were severely calcified. Three patients did not show any signs of CAD. In two patients single-vessel disease was suspected, in five double-vessel disease and in seven triple-vessel disease. The calcium scores and significant stenosis locations are listed in Table 6.3.

6.3.3 QCA findings

In seven of the seventeen patients (41%), a conventional ICA was performed within 45 ± 30 days after the CTA study. In these 7 patients, 15 (resp. 26) of the 100 vessel segments had a stenosis of more than 50% (resp. 20%) on ICA. One patient did not show any CAD, one patient had single-vessel disease, three double-vessel disease and two triple-vessel disease. The artery segment presenting $\geq$ 20% stenosis and the QCA values are listed in Table 6.3. Based on the QCA and SPECT-MPI findings, revascularization was advised in segment(s) of ten coronary arteries.

6.3.4 Findings of side-by-side analysis

Detection of coronary lesions requiring revascularization - For the seven patients in whom QCA was available, there was on average 81% agreement with regard to the therapeutic decision between the observers and the QCA/SPECT-MPI reference standard. Over the 4 (vessels) x 7 (patients) = 28 therapeutic decisions, the four observers agreed in fourteen cases (50%) with the QCA/SPECT-MPI therapeutic decision and three observer agreed in nine cases (32%). For the remaining five cases (18%), there was no consensus. The vessel-based sensitivities of the four observers to correctly refer for revascularization were 80%, 80%, 50% and 60% respectively; the vessel-based specificities were 83%, 83%, 100% and 84% respectively.
Inter-observer agreement - Over all patients, the averaged inter-observer therapeutic decision agreement was 74%. Over the 4 (vessels) x 17 (patients) = 68 therapeutic decisions, the four observers agreed in 41 cases (60%) and one observer disagreed in 19 cases (28%). For the remaining 8 cases (12%), no consensus was reached.

6.3.5 Findings of fused analysis

Detection of coronary lesions requiring revascularization - For the seven patients in whom QCA was available, there was on average 91% agreement with regard to the therapeutic decision between the observers and the QCA/SPECT-MPI reference standard. Over the 4 (vessels) x 7 (patients) = 28 therapeutic decisions, the four observers agreed in 20 cases (72%) with the QCA/SPECT-MPI therapeutic decision and three observers agreed in 6 cases (21%). For the remaining two cases (7%), there was no consensus. The vessel-based sensitivities of the four observers to correctly refer for revascularization were 100%, 90%, 70% and 80% respectively; the vessel-based specificities were 94%, 83%, 100% and 100% respectively.
Inter-observer agreement - Over all patients, the averaged inter-observer therapeutic decision agreement was 84%. Over the 4 (vessels) x 17 (patients) = 68 therapeutic decisions, the four observers agreed in 53 cases (78%) and one of the observer disagreed in 8 cases (12%). For the remaining 7 cases (10%), no consensus could be reached.

6.3.6 Comparison of fused and side-by-side analysis

Table 6.3: Diagnostic performance for the side-by-side and fused CTA/SPECT-MPI analysis.

	Side-by-Side				**Fused CTA/SPECT-MPI**			
Patients with ICA (N=7)								
QCA/SPECT-MPI agreement	81%				91%			
Inter-observer agreement	66%				82%			
Sensitivity (4 observers)	50%	60%	80%	80%	70%	80%	100%	90%
Specificity (4 observers)	100%	94%	83%	83%	100%	100%	94%	83%
All patients (N=17)								
Inter-observer agreement	74%				84%			

Detection of coronary lesions requiring revascularization - By analyzing the integrated SPECT-MPI/CTA information using the SMARTVis system, the averaged therapeutic decision agreement improved in 4 cases (patients 08, 12, 15, 16) and remained the same in the remaining three cases (patients 02, 04, 17). For all observers, it resulted in an increase of their sensitivity and specificity to correctly refer for revascularization.

For example, the QCA analysis of patient 08 (61 y.o. male) revealed a borderline stenosis in the mid-LAD coronary segment (46%) and a significant stenosis in the proximal LCX segment (63%). The SPECT-MPI reports indicated two reversible perfusion defects located in the anterior basal-mid and inferior mid-apical walls (suspected double-vessel disease). Consequently, the expert cardiologist

recommended revascularizing both coronary artery segments. Also, the CTA report indicated one significant stenosis in p-LCX segment, and only mild (20-50%) stenoses in the LAD (suspected single-vessel disease). During the side-by-side analysis, only one observer conceded that a lesion in the mid-LAD was causing the hemodynamically significant perfusion defect in the anterior basal-mid wall, and two observers judged that the proximal LCX lesion was significant and that it required revascularization. During the integrated analysis, all four observers agreed that the perfusion defect in the anterior basal-mid wall was caused by a lesion requiring revascularization in mid-LAD, and three observers conceded that the lesion in proximal LCX was inducing a hemodynamically significant perfusion defect in the inferior mid-apical wall. This perfusion defect was first incorrectly assigned by one observer to a mild lesion in RCA during the side-by-side analysis. Here, the SMARTVis system primarily assisted the observers in their interpretation by indicating the presence of a 52% stenosis in the mid-LAD segment and by showing the patient-specific coronary territories. Figure 6.6 shows the stenoses detected on CTA and QCA, and Figure 6.7 presents some visualization of the SMARTVis system.

Inter-observer agreement **-** The inter-observer therapeutic decision agreement increased in eight of the cases (patients 05, 07, 08, 10, 11, 12, 15, 16), remained the same in seven of the cases (patients 01, 02, 03, 04, 09, 13, 17), and decreased in two cases (patients 06, 14). Over all patients, the inter-observer agreement rose from 74% during the side-by-side analysis to 84% during the integrated analysis using the SMARTVis system; over the 7 patients who underwent ICA, it increased from 66% to 82%, suggesting that increased observer agreement is also towards more correct therapeutic decisions using the SMARTVis system.

Territory disagreement **-** The disagreement in interpretation between side-by-side and fused analysis was the highest for the basal/mid inferior/infero-lateral myocardial regions (7 patients), which may be supplied by either the RCA or the LCX. Disagreement was also reported for the basal/mid antero-lateral myocardial region (2 patients), to which either the LAD, the LCX or the IMB may supply blood. Last, a small disagreement was noticed in the mid antero/infero-septal myocardial region (1 patient), supplied by either the LAD or the RCA.

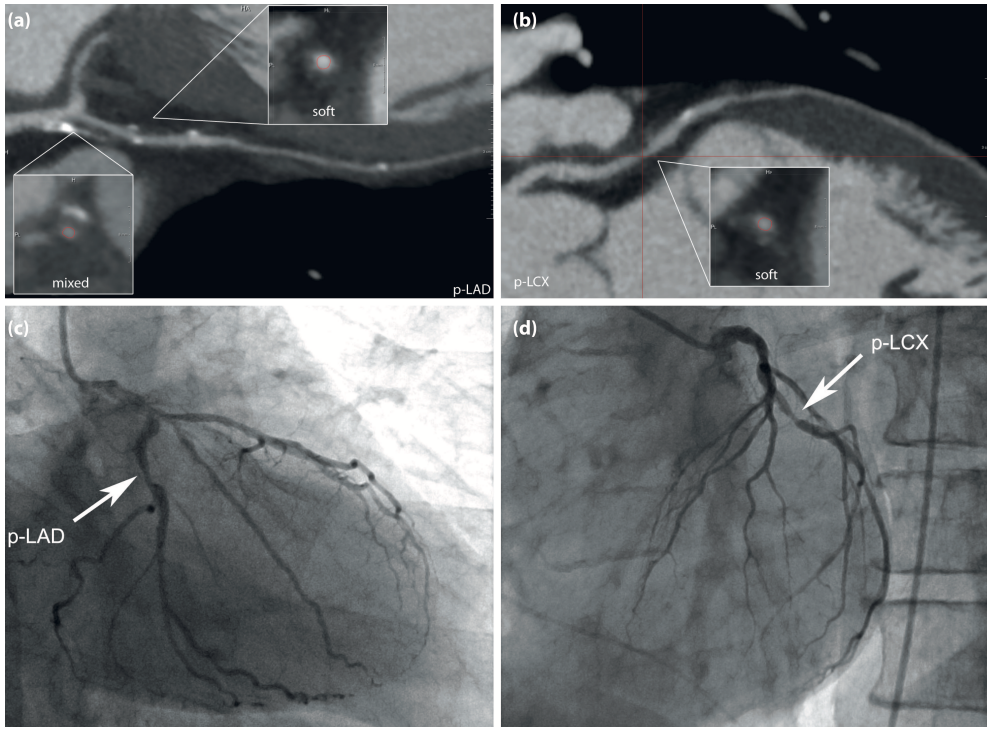

Figure 6.6: Example of patient 08 (61 y.o. male). The CTA report indicates only mild (20-50%) stenoses in the LAD **(a)** and one significant stenosis in p-LCX segment (suspected single-vessel disease) **(b)**. The QCA analysis reveals a 46% stenosis in the proximal LAD coronary segment **(c)** and a 63% stenosis in the proximal LCX segment **(d)**.

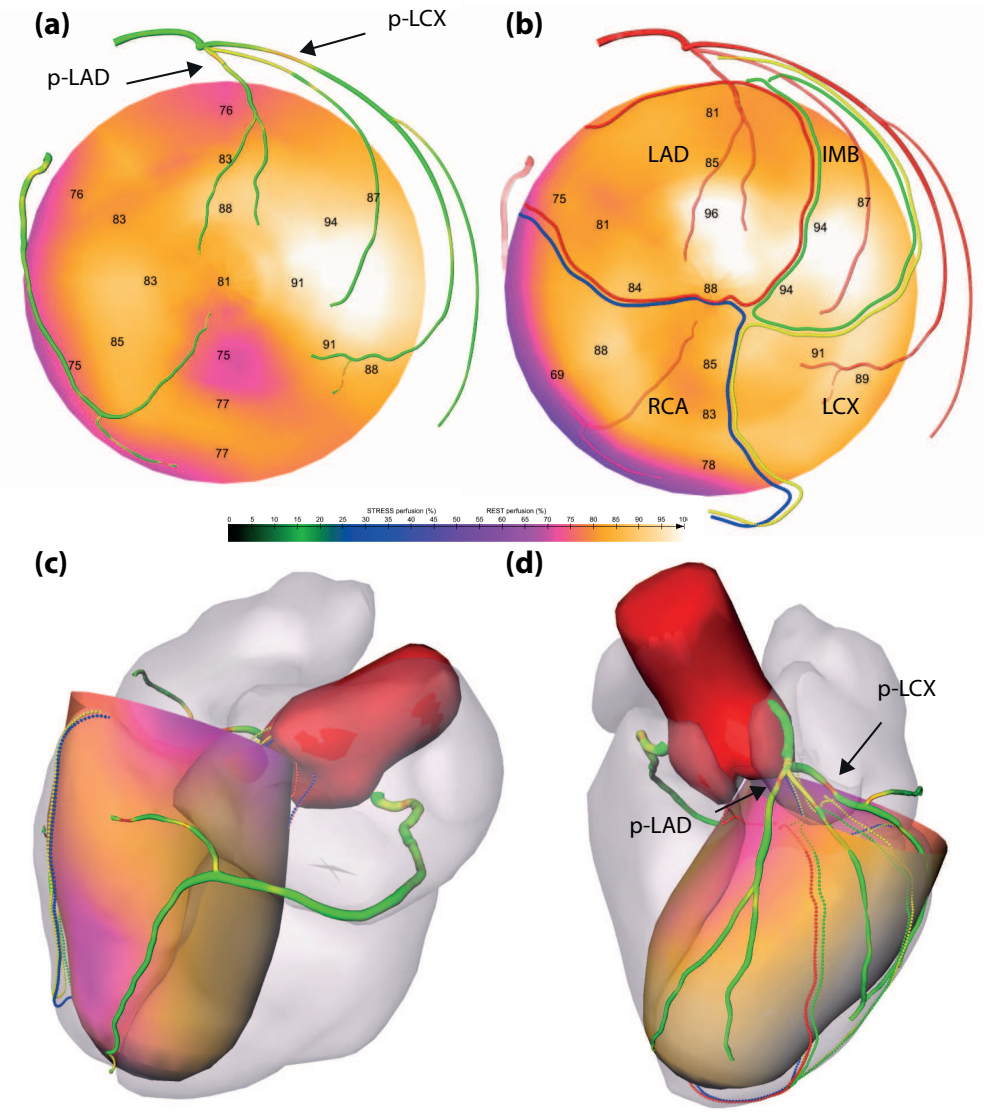

Figure 6.7: Example of patient 08 (61 y.o. male). **(a)** Stress polar map: the coronary vessel tree is color-coded with the automatically estimated degree of stenosis. **(b)** Rest polar map: the coronary arteries are coded with the distance to the epicardium: the more transparent the artery, the further it is from the epicardium. Patient-specific perfusion territories are also projected: LAD in red, LCX in yellow, MO in green and RCA in blue. **(c)(d)** 3D model of the heart and coronary artery tree extracted from CTA fused with 3D stress polar map.

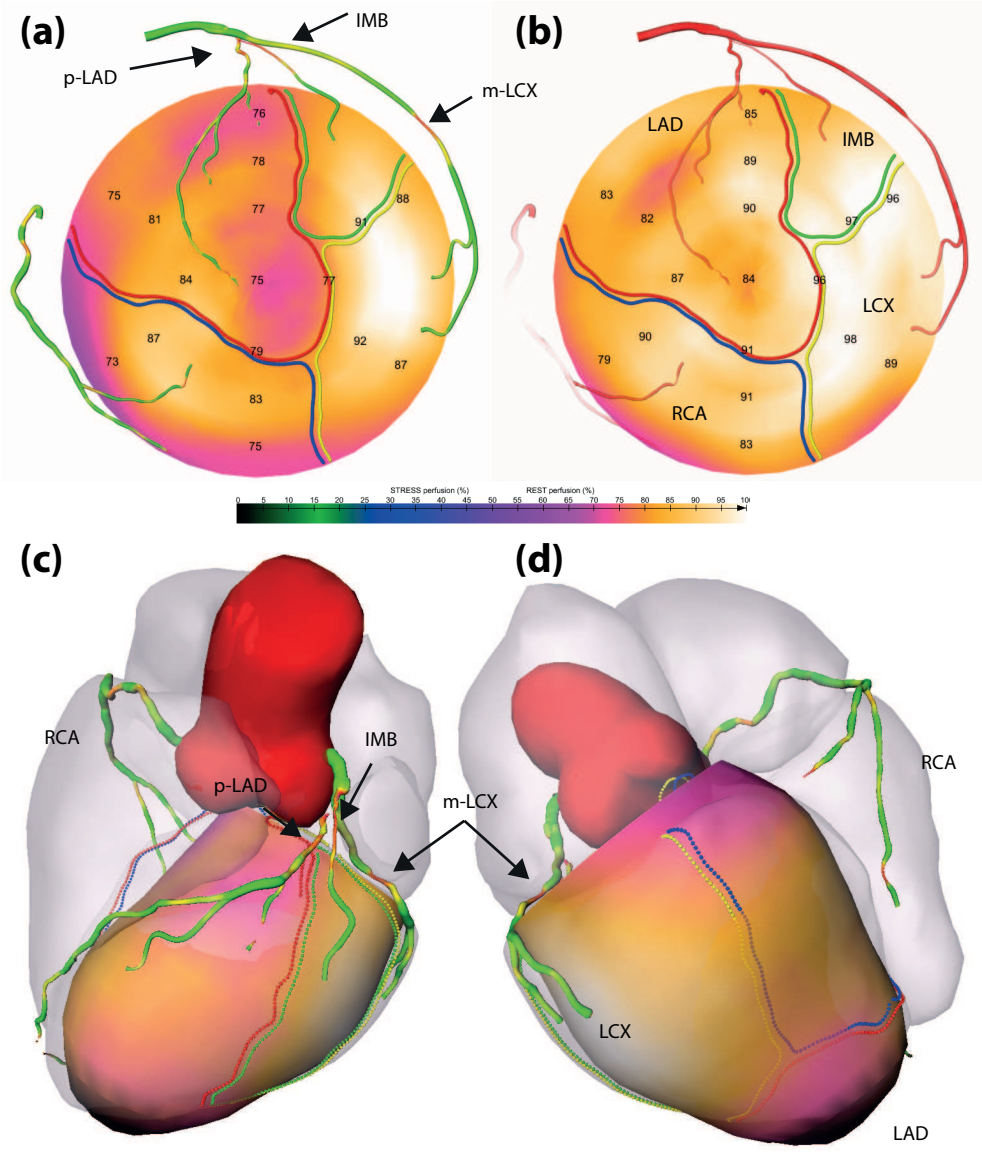

Figure 6.8: Example of patient 07 (65 y.o. male). **(a)** Stress polar map: the coronary vessel tree is color-coded with the automatically estimated degree of stenosis. **(b)** Rest polar map: the coronary arteries are coded with the distance to the epicardium: the more transparent the artery, the further it is from the epicardium. Patient-specific perfusion territories are also projected: LAD in red, LCX in yellow, MO in green and RCA in blue. **(c)(d)** 3D model of the heart and coronary artery tree extracted from CTA fused with 3D stress polar map.

For example, for patient 07 (65 y.o. male), the CTA report indicated the presence of a severe mixed stenosis in the p-LAD segment, a moderate mixed stenoses in the m-LCX segments, and multiple mild stenoses in the three main vessels (suspected double-vessel disease). The SPECT-MPI report indicated three reversible perfusion defects located in the anterior basal-mid, antero/infero-lateral apical and antero/infero-septal basal walls, as well as a fixed perfusion defect in the inferior wall (suspected triple-vessel disease). During the side-by-side analysis, all four observers agreed on the necessity to revascularize the stenosis in LAD, which causes the reversible anterior basal-mid defect. However, no consensus was reached for the therapeutic decision concerning the LCX and the IMB: two observers advised to perform revascularization, while the two others recommended taking medication. During the integrated analysis, the four observers further agreed to treat the IMB with only medication. Also, though all the observers linked the perfusion defect in the antero/infero-lateral basal wall to the lesions in the LCX, only one observer advised to perform revascularization of the LCX. Figure 6.8 presents some visualizations of the SMARTVis system. Here, the integrated analysis of using the SMARTVis system resulted in an increase of the inter-observer therapeutic decision agreement.

6.4 Discussion

6.4.1 Additional diagnostic value of cardiac CTA and SPECT-MPI fused analysis

The results of our case-study, performed with four experts at two medical centers in seventeen patients, demonstrated that in several cases, the integrated analysis of cardiac CTA and SPECT-MPI has a clinical benefit, in the sense that both the inter-observer agreement increased and the therapy planning decisions were in better agreement with the reference standard.

Specifically, we found the tool to be of additional value in the diagnosis of patients who have perfusion defect(s) in fewer coronary territories than suspected vessel disease on CTA, i.e. who have a perfusion defect in one coronary territory and suspected double-/triple-vessel disease on CTA (diagnosis of patients 10, 11 and 12 improved; diagnosis of patients 09 and 13 remained identical), a perfusion defect in two coronary territories and suspected double-/triple-vessel disease on CTA (diagnostic of patients 05, 08, 15 and 16 improved). In such cases, the relation between the coronary territories with a perfusion defect and its supplying coronary arteries is uncertain, thus making the use of the patient-specific SMARTVis system helpful.

The case study further revealed that the image fusion as implemented in the SMARTVis system does not have additional diagnostic value for patients with 1) no coronary stenoses (diagnosis of patients 01, 02 and 03 remained identical), 2) suspected single-vessel disease on both CTA and SPECT-MPI (diagnosis of patient 04 remained identical), and 3) triple-vessel disease (diagnosis of patient 17 remained identical; diagnosis of patient 06 got worse). In fact, if a patient has no significant stenoses reported, but the SPECT-MPI study reveals the presence of perfusion

defect(s), the observers consider that the perfusion defect(s) is/are not cause by obstruction in the epicardial coronary arteries, but may be the result of micro-vascular disease or of artifact. In case of suspected single-vessel disease, it is clear which coronary is causing the perfusion defect, and, thus, integrating information in a patient-specific way leads to the same diagnosis as during side-by-side analysis. Also, patients with suspected triple-vessel disease do not benefit from such a combined approach.

To summarize, integrated analysis of cardiac CTA and SPECT-MPI using the SMARTVis system results in an additional diagnostic value primarily for patients with angiographic CAD that exceeds myocardial hypoperfusion on SPECT-MPI.

6.4.2 Comparison to previous studies

Our work differs from previously published ones (Nakaura et al., 2005; Gaemperli et al., 2007b,a, 2009; Slomka et al., 2009; Kaufmann, 2009; Santana et al., 2009; Sato et al., 2010) primarily by the way the information from CTA and SPECT-MPI is fused, and how the evaluation has been carried out. Previously, CTA images were registered (i.e. aligned) with SPECT-MPI images to provide fused 3D SPECT/CT images. We introduce a comprehensive visualization system to fuse multi-modal imaging data, and provide fused representations in both 2D and 3D for the convenience of the observer. Such an integration of cardiac CTA and SPECT-MPI anatomical and functional information into a single coordinated visual analysis tool is novel, maximizing the diagnostic complementarities of CTA and SPECT-MPI imaging modalities.

The results of the presented work are consistent with the conclusions presented in previously published work on fusion of cardiac CTA and SPECT-MPI for assessment of CAD, where fused CTA/SPECT-MI interpretation appears to provide added diagnostic information on the hemodynamically relevance of coronary artery lesions.

Fusion of cardiac anatomical and functional information for the assessment of CAD has been introduced by (Nakaura et al., 2005). Based on four cases, the study suggested that fused interpretation improves the relationship of relevant coronary arteries and abnormal perfusion territory. Also, (Sato et al., 2010) demonstrated that, based on a population of 130 patients, side-by-side combined interpretation of CTA and SPECT-MPI provides added diagnostic value, as compared to stand-alone CTA interpretation. Recently, in (Gaemperli et al., 2007b,a, 2009), the authors further investigated the incremental diagnostic value of fused CTA/SPECT-MPI interpretation. In (Gaemperli et al., 2007b), thirty-eight patients who underwent both CTA and SPECT-MPI (twenty-five additionally underwent ICA) and presented with at least one perfusion defect on SPECT-MPI were included in an evaluation study similar to ours (i.e. side-by-side vs. fused). The authors demonstrated that fused analysis provides added diagnostic information on pathophysiologic lesion severity not obtained with side-by-side analysis. The evaluations were performed by a consensus of two observers. In our work, four independent observers were involved in the evaluation, which allowed us to also investigate the added diagnostic value of fused analysis to reduce inter-observer variability in revascularization strategy and target vessel

selection decisions. Also, (Gaemperli et al., 2009) demonstrated that fusion of CTA and SPECT-MPI allows accurate detection of flow-limiting coronary stenoses (i.e. significant stenoses inducing ischemia) and that it is thus a potential gatekeeper for ICA and coronary revascularization. In our work, we provide additional insights concerning which patients are more likely to benefit from integrated analysis of fused CTA/SPECT-MPI.

6.4.3 Limitations and strengths of the study design

One limitation of our study is the modest population size. However, results were consistent among observers and datasets. A strength of our study was the use of four independent observers in the evaluation study.

Whether integrated analysis of fused CTA/SPECT-MPI using the SMARTVis system is more time-efficient than side-by-side interpretation remains to be investigated. The interpretation using the SMARTVis system took from 3 minutes to 15 minutes, depending on the complexity of the case and on the observer. In the current study, the observers only had a training session of a few minutes using one excluded patient to get familiar with the SMARTVis system. A reliable investigation of the time-efficiency would require a substantial longer time of use in clinical practice.

Over all, the observers were enthusiastic about the presented integrated visualization tool and some were eager to use the SMARTVis system in clinical practice.

Further investigation also remains to be done to determine which patients should undergo such examination (increased imaging costs and radiation dose versus patient's benefits). We do not recommend all patients to undergo both CTA and SPECT-MPI examination, but underline that if both tests are performed, integrated analysis is to be preferred.

6.5 Conclusion

Integrated analysis of fused cardiac CTA and SPECT-MPI using the SMARTVis system primarily results in additional diagnostic value for patients presenting coronary artery disease in more vessels than the number of reported perfusion defects. The SMARTVis comprehensive visualization system can be effectively used to assess disease status in multi-vessel CAD patients, offering valuable new options for the diagnosis and management of these patients.

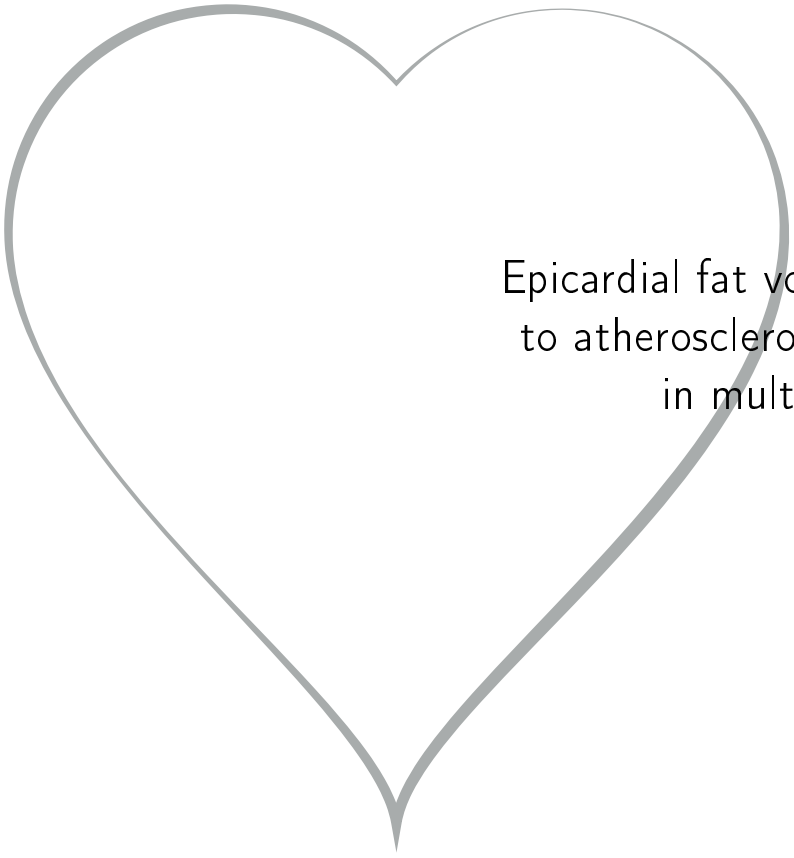

7

Epicardial fat volume is related to atherosclerotic calcification in multiple vessel beds

This chapter is based on the manuscript:
Epicardial fat volume is related to atherosclerotic calcification in multiple vessel beds,
D. Bos, **R. Shahzad**, T. van Walsum, L. van Vliet, O.H. Franco, A. Hofman, M.W. Vernooij,
W.J. Niessen, and A. van der Lugt, *submitted*.

Abstract

Purpose Epicardial fat is suggested to promote coronary artery atherosclerosis. It is yet unclear whether it is also associated with atherosclerosis in other vessels, and thereby represents a marker of systemic vascular risk. Hence, we investigated the association of epicardial fat volume with atherosclerosis in four major vessel beds in a large sample of community-dwelling elderly.

Methods From the population-based Rotterdam Study, 2,524 middle-aged and elderly participants underwent non-enhanced cardiac computed tomography (CT). We quantified epicardial fat volume in milliliters (ml) using a fully automatic method. Moreover, we quantified atherosclerotic calcification in the coronary arteries, aortic arch, extracranial and intracranial internal carotid arteries. We investigated the relationship between epicardial fat volume and atherosclerotic calcification volume in each vessel bed using linear regression models, adjusting for age and sex. Additionally we adjusted for cardiovascular risk factors.

Results We found that epicardial fat volume was positively correlated with calcification volume in all four vessel beds. Most prominent associations were found for coronary artery calcification and extracranial carotid artery calcification [fully-adjusted difference in standardized calcification volume per SD increase in epicardial fat volume: 0.10 (95%C.I.: 0.05; 0.15), and 0.12 (95%C.I. 0.07; 0.18), respectively].

Conclusions Epicardial fat is not only a marker of local, coronary atherosclerosis, but it also associates with extracranial carotid artery atherosclerosis. On the other hand, it is not related with the amount of atherosclerosis in the aortic arch or intracranial carotid arteries.

7.1 Introduction

The amount of epicardial fat is related to cardiovascular disease (Iacobellis and Bianco, 2011; Iacobellis and Willens, 2009; Mahabadi et al., 2013). Epicardial fat is defined as the adipose tissue located between the outer wall of the myocardium and the visceral layer of pericardium (Iacobellis, 2012; Dey et al., 2012). This anatomically close relationship with the coronary arteries may directly explain its association with cardiovascular disease. Indeed, several studies have shown an association between larger amounts of epicardial fat and the presence of coronary artery atherosclerosis (Iacobellis and Willens, 2009; Dey et al., 2012, 2010; Rosito et al., 2008; Bettencourt et al., 2011). Epicardial fat might directly influence the formation of coronary artery atherosclerosis through local secretion of pro-atherogenic factors, and might thereby contribute to clinical coronary events (Iacobellis and Willens, 2009; Dey et al., 2012, 2010; Rosito et al., 2008; Bettencourt et al., 2011). Despite this, it remains unclear whether the amount of epicardial fat also exerts a systemic effect on the development of atherosclerosis located in other vessel beds.

Conventional cardiovascular risk factors are associated with both the amount of epicardial fat (Mahabadi et al., 2013; Rosito et al., 2008), and with the amount of atherosclerosis across vessel beds (Allison et al., 2004; Lusis, 2000; Odink et al., 2009). It is therefore important to investigate whether any association between epicardial fat and atherosclerosis is present independent of conventional cardiovascular risk factors. Disentangling the role of epicardial fat in the etiology of atherosclerosis may eventually serve as a basis for developing therapeutic or preventive strategies for atherosclerosis.

In this study, we investigated risk factors that influence the amount of epicardial fat, and we set out to investigate the relationship of the epicardial fat volume with atherosclerotic calcification, as proxy of atherosclerosis, in the coronary arteries, aortic arch, extracranial carotid arteries and intracranial carotid arteries, in a large sample of participants from the population-based Rotterdam Study.

7.2 Materials and methods

7.2.1 Settings

This study is based on the population-based Rotterdam Study (Hofman et al., 2011), which is an ongoing cohort study that started in 1990, with follow-up every 3-4 years. Over 96% of Rotterdam Study participants is of white descent. From 2003 until 2006, all participants who completed a regular visit at the research center were invited to undergo multi-detector computed tomography (MDCT) of the coronary arteries, aortic arch, extracranial carotid arteries and intracranial carotid arteries. In total, 2,524 participants were scanned. The medical ethical committee of the Erasmus MC approved the study. All participants gave informed consent.

Table 7.1: Population characteristics. Values are mean (standard deviation) for continuous variables, percentages for dichotomous variables. * Median (interquartile range).

Variable	Value
Sample size	2298
Women	52.8%
Age, years	69.4 (6.6)
Obesity	23.9%
BMI, kg/m^2	27.7 (4.0)
Hypertention	73.4%
Systolic blood pressure, mmHg	146.7 (20.0)
Diastolic blood pressure, mmHg	80.4 (10.7)
Diabetes	10.9%
Serum glucose, mmol/l	5.7 (1.2)
Hypercholesterolemia	48.6%
Serum total cholesterol, mmol/l	5.7 (1.0)
Low HDL, $<$ 1.0 mmol/l	10.7%
Serum HDL-cholestrol, mmol/l	1.4 (0.4)
Past and current smokers	67.4%
Epicardial fat volume *, ml	101.5 (80.0 – 129.8)

7.2.2 Assessment of epicardial fat and atherosclerosis

CT-acquisition **-** A 16-slice (n = 785) or 64-slice (n = 1,739) MDCT-scanner (Somatom Sensation, Siemens, Forcheim, Germany) was used to perform non-enhanced CT-scanning. Using a cardiac scan and a scan that reached from the aortic arch to the intracranial vasculature (1 cm above the sella turcica), the following vessel beds were scanned: the coronary arteries, the aortic arch, the extracranial carotid arteries, and the intracranial carotid arteries. Detailed information regarding imaging parameters of both scans is provided in the work of Odink et al (Odink et al., 2007).

Quantification of epicardial fat **-** The cardiac scan was used for the quantification of epicardial fat (Figure 7.1). We used a fully automatic tool for quantification of epicardial fat in millilitres (ml) which has been explained in **Chapter 4** (Shahzad et al., 2013). Briefly, the quantification method consists of two steps: 1) whole heart segmentation, and 2) epicardial fat volume quantification. For whole heart segmentation, we used a multi-atlas based segmentation approach. Eight manually segmented contrast-enhanced cardiac CTA images (atlases) were registered (spatially aligned) with every participant's CT image. Next, the segmentations of these atlases were mapped onto the subjects scan to obtain the final segmentation. The fat was quantified by applying a threshold of -200 to -30 Hounsfield Units to the segmented heart region (Yoshizumi et al., 1999). A connected-component analysis was applied to all adipose tissue voxels using an 18-neighbourhood rule, in order to remove regions smaller than 10 voxels (2.8 mm^3) in size, which we considered to be noise. This

automatic method showed to be as good as manual quantification (Shahzad et al., 2013).

Quantification of atherosclerotic calcification - Dedicated commercially available software (Syngo CalciumScoring, Siemens, Germany) was used to automatically quantify atherosclerotic calcification in the coronary arteries, the aortic arch and the extracranial internal carotid arteries (Odink et al., 2007). Calcification in the intracranial internal carotid arteries was quantified using a semi-automated method (Bos et al., 2012; de Weert et al., 2009). Calcification volumes were expressed in cubic millimeters (mm^3).

7.2.3 Assessment of cardiovascular risk factors

Information on cardiovascular risk factors was obtained during a home-interview and a visit to the research center (Odink et al., 2009; Hofman et al., 2011). Height and weight were measured and the body mass index (BMI) [weight (kg)/height^2(m)] was calculated. Systolic and diastolic blood pressures were measured twice at the right arm using a random zero-sphygmomanometer. The mean of the two measurements was used for the analyses. Fasting blood samples were obtained and serum total cholesterol and high-density lipoprotein (HDL) cholesterol were measured using an automatic enzymatic procedure (Hitachi analyzer, Roche Diagnostics). Glucose was determined enzymatically by the Hexokinase method. Diabetes was defined as fasting serum glucose levels $\geq$ 7.0 mmol/l and/or the use of anti-diabetic therapy (ADA, 2013). Participants were categorized based on smoking status into "past or current smoker" or "never smoker". Finally, information on the use of blood pressure lowering medication and lipid-lowering medication was assessed by interview.

7.2.4 Population for analysis

Due to image artefacts (n = 189) or segmentation errors (n = 37), 226 from the 2,524 examinations were not gradable for either epicardial fat volume or calcification volume in one of the four vessel beds. Hence, the current study population consists of 2,298 participants with complete data on epicardial fat volume and calcification volume in each of the four vessel beds.

7.2.5 Statistical analysis

Due to the right skewness of the distribution of epicardial fat volume, this measure was natural log-transformed [ln(epicardial fat volume in ml)]. Using linear regression we investigated the association, both uni-variable and multi-variable, of BMI, systolic and diastolic blood pressure, total cholesterol, HDL cholesterol, diabetes, smoking, use of blood pressure lowering medication, and use of lipid-lowering medication with epicardial fat volume.

Next, we assessed the association of epicardial fat volume with atherosclerotic calcification volumes. Atherosclerotic calcification volumes had a highly skewed distribution. Therefore we used natural log-transformed values and added 1.0 mm^3

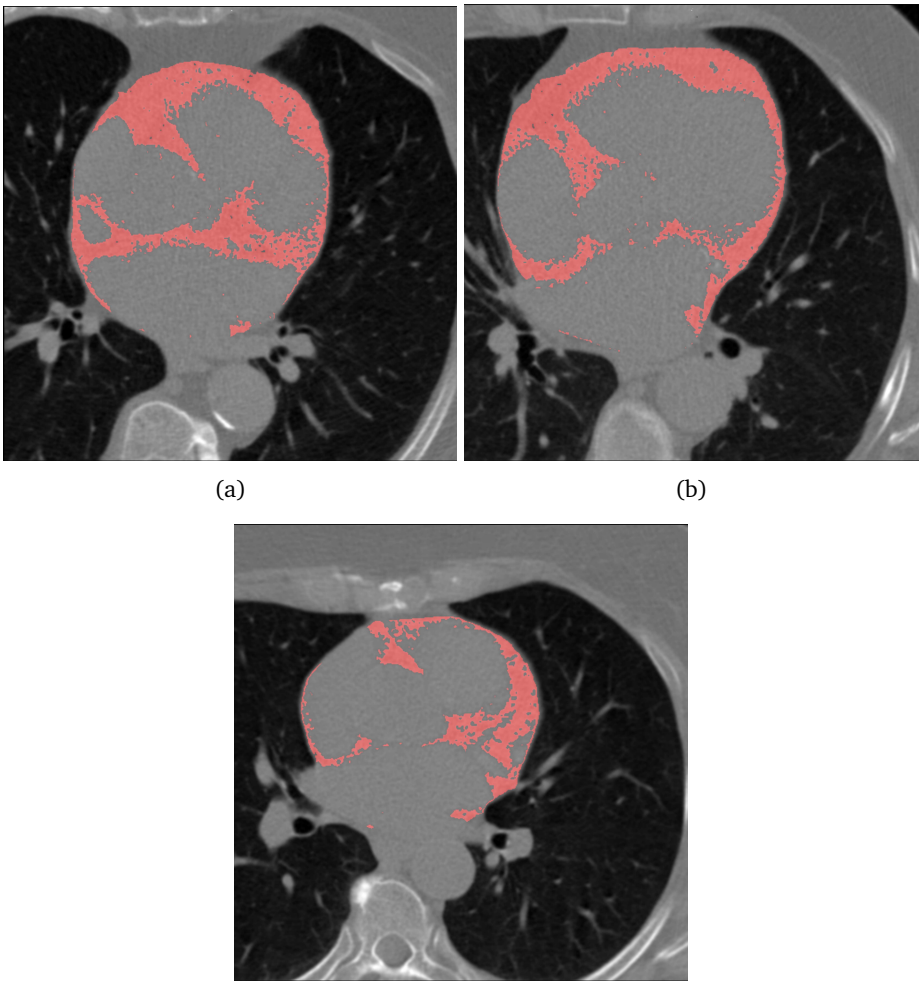

(a) (b)

(c)

Figure 7.1: Different degrees of epicardial fat volume. This figure shows epicardial fat (red) on approximately the same slice in three different study participants. The epicardial fat volume decreases from left to right.

to the non-transformed values in order to deal with participants with a calcium score of zero [ln (Calcification volume in mm^3 + 1 mm^3)]. We assessed the relationship between epicardial fat volume (per standard deviation increase) and the atherosclerotic calcification volume at each location using linear regression. Model 1 was adjusted for age and sex. In model 2, we additionally adjusted for all abovementioned cardiovascular risk factors.

IBM SPSS Statistics version 20 (International Business Machines Corporation, Armonk, New York) was used for statistical analyses.

7.3 Results

Table 7.1 shows the characteristics of the study population. The mean age was 69.4 ± 6.6 years and 52.8% was female. The median epicardial fat volume in the population was 101.5 ml (interquartile range: 80.0 – 129.8 ml).

The associations between conventional cardiovascular risk factors and epicardial fat volume are shown in Table 7.2. We found that all cardiovascular risk factors were significantly associated with larger epicardial fat volume in the age and sex-adjusted analyses. Yet, in the analyses which included all cardiovascular risk factors, systolic and diastolic blood pressures were no longer related to epicardial fat volume.

Figure 7.2 depicts the median calcification volumes for each vessel bed, per quartile of epicardial fat volume. Calcification volumes in all vessel beds increased over the quartiles. We found that a larger epicardial fat volume was associated with larger volumes of coronary, aortic, extracranial and intracranial internal carotid artery calcification (Table 7.3, model 1). After adjusting for cardiovascular risk factors, this association remained present for coronary artery calcification and extracranial carotid artery calcification. The differences in calcification volume per SD increase in epicardial fat volume: 0.10 (95% confidence interval (C.I.): [0.05; 0.15]), and 0.12 (95% C.I.: [0.07; 0.18]), respectively. The relationship between epicardial fat and aortic arch calcification and intracranial carotid artery calcification completely diminished (Table 7.3, model 2).

7.4 Discussion

In this large population-based study among middle-aged and elderly community dwelling persons, we demonstrated that, apart from systolic and diastolic blood pressure, all other conventional cardiovascular risk factors are associated with larger epicardial fat volume. Moreover, we found that a larger epicardial fat volume is associated with a larger amount of atherosclerotic calcification in both the coronary arteries and the extracranial carotid arteries.

Strengths of this study include the population-based setting, and the image-based quantification of both epicardial fat and atherosclerosis. Although the majority of previous studies performed measurements of epicardial fat using ultrasound, CT is superior in detecting and quantifying the amount of epicardial fat accurately (Mahabadi et al., 2013; Nichols et al., 2008). Moreover, we were the first to

Table 7.2: Values represent differences in standardized calcification volumes [Ln(calcification volume + 1 mm3)] with 95% confidence intervals in each vessel bed, per standard deviation (SD) increase in epicardial fat volume. Model 1: Adjusted for age and sex. Model 2: Additionally adjusted for cardiovascular risk factors.

Picardial fat volume	**Coronary artery calcification**	**Aortic arch calcification**	**Extracranial carotid artery calcification**	**Intracranial carotid artery calcification**
Model 1, per SD increase	0.15 (0.11;0.20)	0.11 (0.07;0.15)	0.14 (0.10;0.18)	0.07 (0.03;0.11)
Model 2, per SD increase	0.10 (0.05;0.15)	0.03 (-0.02;0.08)	0.13 (0.07;0.18)	0.01 (-0.04;0.07)

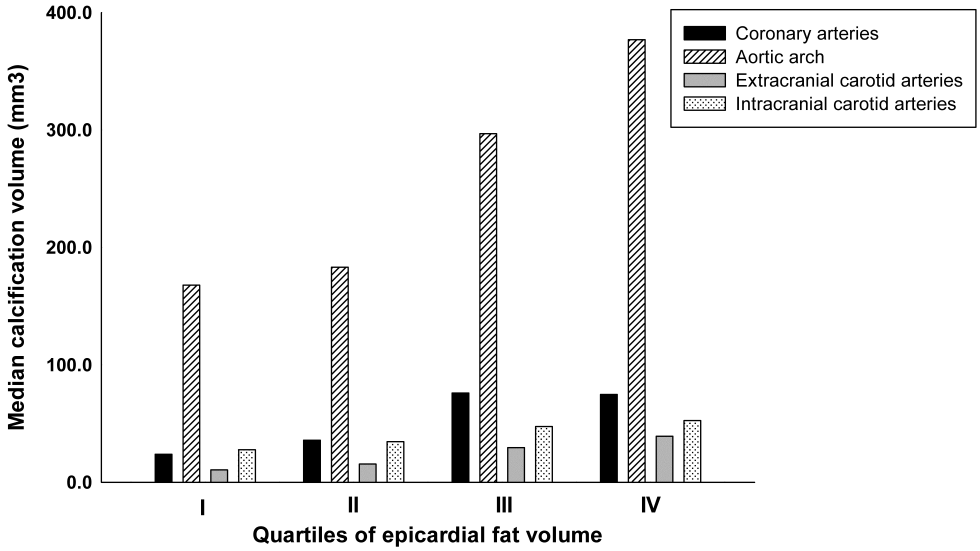

Figure 7.2: Distribution of atherosclerotic calcification over the quartiles of epicardial fat volume. Median calcification volumes are displayed per quartile of epicardial fat volume, for each of the four vessel beds.

develop and apply a fully automatic method to quantify epicardial fat volume on non-enhanced CT-scans (Shahzad et al., 2013). Several potential limitations of our study should also be addressed. First is the definition of epicardial fat which is used in the literature (Mahabadi et al., 2013; Dey et al., 2010; Rosito et al., 2008; Ding et al., 2008). Especially pericardial fat and epicardial fat are interchangeably used, which may hamper the comparison of results. In our study we applied the definition as proposed by Iacobellis et al (Iacobellis, 2012). Second, we were not able to measure the complete atherosclerotic plaque with non-enhanced CT. Nonetheless, there is strong evidence from autopsy studies that CT-based calcification quantification provides a sensitive and reliable marker of the total underlying atherosclerotic burden (Rumberger et al., 1995; Sangiorgi et al., 1998).

In agreement with others, we found that most conventional cardiovascular risk factors are associated with the amount of epicardial fat (Mahabadi et al., 2013; Dey et al., 2012; Rosito et al., 2008). Also our finding that systolic and diastolic blood pressure were not associated with epicardial fat volume has been shown before from a population-based perspective (Mahabadi et al., 2013).

We found a strong association between the amount of epicardial fat and larger volumes of coronary artery calcification, which was independent of conventional cardiovascular risk factors. The relationship between epicardial fat volume and the amount of coronary artery calcification has been demonstrated previously (Mahabadi

Table 7.3: Cardiovascular risk factors and epicardial fat volume. Values represent differences in standardized Ln(epicardial fat volume) with 95% confidence intervals per cardiovascular risk factor. Model 1: Adjusted for age and sex. Model 2: Additionally adjusted for obesity, hypertension, diabetes mellitus, hypercholesterolemia, low HDL-cholesterol, and smoking status.

	Differences in epicardial fat volume	
	Model 1	*Model 2*
Age	0.02 (0.01;0.02)	0.02 (0.01;0.02)
Sex	-0.80 (-0.88;-0.73)	-0.80 (-0.88;-0.73)
Obesity	0.87 (0.79;0.95)	0.78 (0.70;0.87)
Hypertension	0.38 (0.29;0.46)	0.22 (0.14;0.30)
Diabetes mellitus	0.46 (0.35;0.58)	0.20 (0.09;0.31)
Hypercholesterolemia	0.18 (0.10;0.25)	0.14 (0.07;0.21)
HDL < 1 mmol/l	0.32 (0.20;0.44)	0.17 (0.06;0.28)
Smoking (ever vs. never)	0.25 (0.17;0.34)	0.18 (0.10;0.26)

et al., 2013; Rosito et al., 2008; Ding et al., 2008), and has been postulated to be due to the production of inflammatory factors by epicardial fat, directly influencing the formation of atherosclerotic plaques in the coronary arteries (Mahabadi et al., 2013; Baker et al., 2006; Hirata et al., 2011). Yet, we also found an association between epicardial fat with atherosclerosis at other locations, namely in the extracranial carotid arteries. This was interesting, even more so because this relationship also remained present after adjusting for cardiovascular risk factors. Although data on this subject are scarce, it was demonstrated that in HIV-infected persons, epicardial fat is related to carotid artery atherosclerosis, as measured with carotid ultrasound (intima-media thickness) (Iacobellis et al., 2007). This suggests that, apart from a local effect on the formation of atherosclerosis, epicardial fat also exerts systemic influence on the formation of atherosclerosis in other vessel beds. A possible mechanism could be through systemic inflammation. In persons suffering from coronary artery disease, higher serum levels of certain adipocytokines (e.g. resistin, adiponectin), as produced by epicardial fat, were found (Baker et al., 2006; Reilly et al., 2005). Through these increased levels of inflammatory factors epicardial fat possibly also influences the development of atherosclerosis at other locations. It should also be acknowledged that there may be other factors, e.g. genetic, that influence both the amount of epicardial fat and atherosclerosis.

Contrary to the finding with extracranial carotid artery calcification, we did not find an association of epicardial fat with aortic arch or intracranial carotid artery calcification after adjustment for cardiovascular risk factors. In other words, the initial relationship we found between epicardial fat and calcification in these two vessels is completely explained by the cardiovascular risk factors. These differences in associations between epicardial fat and atherosclerotic calcification across various vessel beds may partly be explained by location-specific differences in the etiology

of atherosclerosis (Bos et al., 2013). Although atherosclerosis occurs systemically, correlations between atherosclerosis across different vessel beds are only moderate (Allison et al., 2004; Odink et al., 2007; Bos et al., 2011). Specifically for the associations with epicardial fat, it might be that certain vessels are more susceptible to the changes induced by epicardial fat than other vessel beds, where different factors might play a more important role. Another explanation might lay in the composition of plaques. Plaques in the aortic arch and intracranial carotid arteries tend to be more calcified and consist of less non-calcified plaque components than plaques in the extracranial carotid artery and the coronary arteries. Interestingly, epicardial fat is specifically suggested to be related to low-density non-calcified plaque (Dey et al., 2012). Yet, longitudinal research is needed to further disentangle the complex role of epicardial fat in the development of atherosclerosis in multiple locations.

7.5 Conclusion

In this population-based study we found that, apart from blood pressure, all conventional cardiovascular risk factors are associated with a larger amount of epicardial fat volume. Furthermore, we demonstrated that the amount of epicardial fat is associated with coronary atherosclerosis, and that it is related to extracranial carotid artery atherosclerosis. This suggests that epicardial fat not only locally influences the formation of atherosclerosis, but that it also exerts a systemic effect on atherosclerosis development.

8

Summary and General discussion

8.1 Summary

In this thesis work, we developed and evaluated techniques for automatic extraction of quantitative imaging biomarkers for cardiovascular diseases (CVDs) from CT imaging data. The biomarkers considered were coronary artery calcium, epicardial fat volume and coronary stenosis grade. Also, the relationship between epicardial fat volume and atherosclerotic calcifications was investigated. In addition to the CT based assessment, the additional diagnostic value of integrating cardiac anatomical and functional biomarkers obtained from multi-modal imaging techniques was studied.

8.1.1 Technical developments

In **Chapter 3**, we presented a method that automatically quantifies calcium scores. Calcium scores are relevant for treatment planning and monitoring the progression of coronary artery disease (CAD). The method we presented not only provides the commonly used whole heart calcium score but also vessel specific calcium scores, which provide local information on the distribution of the disease over the coronary arteries.

The calcium scoring method consists of two steps: calcium object candidate detection, followed by classification of these object into calcium and non-calcium objects. The classification method is based on a pattern recognition approach. We investigated 62 different features that could help us categorize the candidate objects. One of the key features used in our method, that not only helped us narrow down our search for true calcium objects, but also helped us label the detected calcium object to the respective artery was the so-called 'Coronary Density Estimate'. The development and evaluation of this feature was the subject of **Chapter 2**. Briefly, this feature estimates the likeliness that an object is located in a certain coronary artery, by computing a probability density function of coronary artery locations from a large set of images where the coronary artery locations are known.

Detection of calcified objects was achieved with a sensitivity of 81.2% per calcified object in data with a slice thickness of 1.5 mm and with a sensitivity of 86.6% per calcified object in data with a slice thickness of 3.0 mm. A larger slice thickness results in scans with lower amounts of noise, hence resulting in lower number of candidate objects being detected. This is the reason why the sensitivity on the 3.0 mm scans is slightly better than that on the 1.5 mm scans. The method made an average of 2.3 errors per patient on the data sets. The average R values for Agatston, mass, and volume scores for each of the arteries (left circumflex coronary artery, right coronary artery, and left main + left anterior descending coronary arteries) were 0.93, 0.96, and 0.99, respectively, for the 1.5 mm data sets. Similarly, for 3.0 mm data sets, R values were 0.94, 0.94, and 0.99, respectively. Risk category assignment was correct in 95% and 89% of the data sets in the 1.5 mm and 3.0 mm scans. Though the sensitivity on the 3.0 mm scans is higher than the 1.5 mm scans, the accuracy of correctly assigning the risk category on the 3.o mm scans is a bit lower, this could be due to the fact that the subjects lying at the border of calcium quantification intervals could easily be misclassified to an adjacent category, it should also be noted that we have twice as many 1.5 mm testing scans compared to the 3.0 mm testing scans.

In **Chapter 4**, we presented an atlas-based segmentation method to quantify the amount of fat that surrounds the coronary arteries and the heart. There is increasing evidence that suggests that fatty tissue around the coronary arteries facilitates local production of inflammatory factors which may directly contribute to the formation of coronary atherosclerosis. However, in order to validate this hypothesis, evaluation on a large number of clinical datasets needs to be performed. Such an investigation would benefit greatly from a fully automatic method.

The method developed uses eight CTA scans as atlases, in which the pericardium was manually delineated by an expert. In order to segment the pericardium on the CT scan, the eight atlases were spatially registered to the subject scan. The resulting transformations obtained from the registration were used to propagate the pericardium segmentation from the atlas scans to the subject's scan; a majority vote was applied to fuse the segmentations of the eight atlases into a single segmentation. Once the final segmentation was obtained, a threshold window of -200 to -30 HU was applied to obtain the epicardial fat volume.

Automatic segmentation of the pericardium was achieved with a Dice similarity index of 89.1 ± 2.6% with respect to the first observer and 89.2 ± 1.9% with respect to the second observer. The correlation between the automatic method and the manual observers with respect to the epicardial fat volume computed as the Pearson's correlation coefficient (R) was 0.91 ($P < 0.001$) for both observers. The method performed as good as the manual observers and could thus potentially be used in clinical settings.

In **Chapter 5**, we presented an automatic method to detect and quantify coronary artery stenoses from CTA data. The reference standard for coronary stenosis quantification is conventional coronary angiography (CCA) which is of projective nature and invasive. CTA scans are now also being routinely obtained to assess CAD. CTA has the advantage that it is a 3D imaging modality, and that it is noninvasive. In addition it can provide information on the plaque composition.

Extraction of coronary arteries from CTA data is a crucial step for accurate visualization, and pathology detection and quantification. The method developed by us consists of four stages: centerline extraction, bifurcation detection, lumen segmentation and finally detection and quantification of stenoses. In the first step the coronary centerline is obtained using a two stage minimum cost path approach, which is complemented with a calcium suppression step in order to avoid the centerline from running into calcium lesions. In the next stage coronary bifurcations of the coronary arteries are detected and the centerlines divided into segments. The following step delineates the lumen for each of the coronary artery segments, using the coronary centerline as initialization. In the final step the stenoses are detected and quantified from the segmented lumen, using the measured radius and estimated healthy radius of the artery.

Quantitative evaluation on 30 datasets of the publicly available *coronary artery stenosis detection and evaluation framework* showed, for the detection, a sensitivity of 29% and a PPV of 24% as compared to QCA, and a sensitivity of 21% and a PPV of 23% when compared to manual assessment on CTA. The stenosis degree was estimated with an absolute average difference of 31%, root mean square difference of 39.3%

when compared to QCA, and a weighted kappa value of 0.29 when compared to CTA. A Dice of 68% and 65% was reported for lumen segmentation of healthy and diseased vessel segments respectively.

The results thus show that once detected, automatic stenosis quantification on CTA can be performed with an accuracy close to those obtained by the observes. However, automatic discrimination between significant and non-significant lesions in CTA, as compared to QCA, remains a challenge.

8.1.2 Clinical applications

In **Chapter 6**, we presented the SMARTVis system to integrate perfusion information from SPECT-MPI with anatomical information obtained from CTA. The work presented in **Chapter 3** and **Chapter 5** has been integrated into the SMARTVis system. We investigated the additional diagnostic value of fused CTA/SPECT-MPI analysis compared to side-by-side analysis in patients with suspected CAD. A clinical evaluation was performed, involving four experts from two medical centers and 17 patients suspected of having single-, double- or triple-vessel disease. It was shown that the SMARTVis comprehensive visualization system can effectively be used to assess disease status in multi-vessel CAD patients, and thus is a valuable tool for the diagnosis and management of these patients.

In **Chapter 7**, we used the technology developed in **Chapter 4** to investigate the relationship between epicardial fat volumes with atherosclerosis in other vessels and the association of epicardial fat with cardiovascular risk factors. The study was performed on 2298 middle-aged subjects from the population-based Rotterdam Study. The automatic epicardial fat quantification method proposed in **Chapter 4** was used to obtain the epicardial fat volumes. It was visually observed that the automatic method failed only on 37 out of the 2298 subjects corresponding to a rate of 1.6%. The study demonstrated that epicardial fat volume was related to coronary and extracranial carotid artery calcium volume. There was also a strong association between larger epicardial fat volumes and conventional cardiovascular risk factors.

8.2 General discussion

For better management of cardiovascular disease, it is of utmost importance to categorize subjects into different risk groups. This categorization can be made based on cardiovascular risk factors including the family history of the subject. Imaging techniques play an increasing role in cardiovascular risk prediction. In this thesis we set out to develop and evaluate automatic techniques for the extraction of quantitative imaging biomarkers for coronary artery disease.

One of the important cardiovascular risk factor is the presence of calcium in the arteries. In **Chapter 3** we presented an automatic method that can compute the amount of calcium scores for the whole heart as well as for each of the coronary arteries from CT data. The system also categorizes patients into different risk groups. This vessel specific calcium lesion information can be used for treatment planning and assessing progression of CAD in follow up studies. The possibility to assign calcium to

individual coronary arteries was possible owing to the introduction of the 'Coronary Density Estimate' in **Chapter 2**. Next to automatic calcium scoring per artery, as presented in **Chapter 3**, this method could e.g. also be used in the application of automatic centerline extraction by providing a ROI for the algorithm, reducing the computational time and avoiding manual interactions.

A second imaging biomarker we considered, which is receiving increasing interest in CAD, is epicardial fat volume. In **Chapter 4**, we present a method that can accurately quantify the amount of epicardial fat volume. It was demonstrated that the method performs as good as the manual observers, hence has great potential to be used in daily clinical practice. In a clinical study presented in **Chapter 7** on 2298 subjects it was demonstrated that indeed larger volumes of epicardial fat volumes were related to larger volumes of calcified lesions in the various vessel beds. The potential of this biomarker will need to be established in multiple larger studies.

The third imaging biomarker in CAD considered in this thesis is coronary artery stenosis grade. Accurate detection and quantification of coronary stenoses is of great importance, as this information is very important for the clinician in order to make accurate treatment selection and planning. In **Chapter 5** we investigated the ability of detecting and quantifying coronary stenoses from CTA data. We demonstrated that the vessel lumen can be segmented with a precision similar to the human observers, but that it is still a challenge to be able to distinguish between significant and non-significant lesions.

Quantitative imaging biomarkers in CAD may provide both anatomical and functional information, and are often obtained from different imaging modalities. An important subject with respect to treatment planning is therefore the ability to combine information from different modalities in an integrated display. This would help the clinicians in better linking morphological (anatomical) and functional information. In **Chapter 6** the SMARTVis system was introduced, where anatomical information from CTA scans and functional information from SPECT-MPI were integrated into one visualization system. The integrated visualization proposed in the SMARTVis system enables a *one-stop-shop* visual exploration of cardiac anatomical and functional data, to maximally exploit the complementary information of multiple imaging modalities. It has been confirmed that such comprehensive visualizations allow to effectively relate perfusion defects and coronary lesions, and that fused integrated analysis leads to a more accurate diagnosis.

The challenge of extracting imaging biomarkers not only lies in the image processing methodology developed, but also on the quality of the imaging data that can be acquired. CT and CTA have greatly increased our capabilities to non-invasively assess different aspects of CAD. However, it has also caused serious concern with respect to the ionizing radiation patients are exposed to. Recently, there has been a lot of emphasis on decreasing dose levels in CT examinations. Previous generation of scanners could deliver effective radiation doses ranging between 4 mSv to 30 mSv. With new developments in scanner detectors, acquisition protocols, and reconstruction algorithms the effective radiation dose can now be reduced to as low as 1 mSv for an entire heart scan. However, there is always a trade-off between the noise level of the scan and the effective radiation dose. Care should be taken that

the scan obtained with really low radiation dose is still be of diagnostic quality. Here also, the role of automatic image processing will play an increasingly important role. Not only to extract relevant quantitative imaging biomarkers from CT imaging data, but also establish with what accuracy they can be assessed. For a number of relevant cardiovascular quantitative imaging biomarkers, this thesis has provided the required methodology for that purpose.

Bibliography

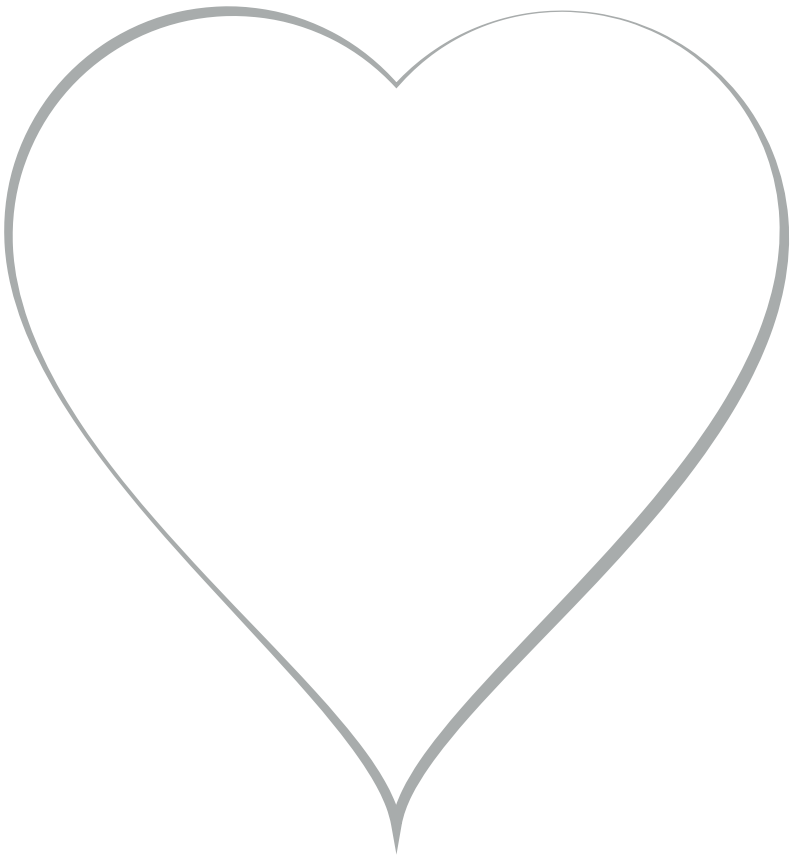

ADA, 2013. American Diabetes Association. Standards of medical care in diabetes – 2013. Diabetes care 36 (supplement 1), S11–S66.

Agatston, A. S., Janowitz, W. R., Hildner, F. J., Zusmer, N. R., Viamonte Jr, M., Detrano, R., 1990. Quantification of coronary artery calcium using ultrafast computed tomography. Journal of the American College of Cardiology 15 (4), 827–832.

Alexopoulos, N., McLean, D. S., Janik, M., Arepalli, C. D., Stillman, A. E., Raggi, P., 2010. Epicardial adipose tissue and coronary artery plaque characteristics. Atherosclerosis 210 (1), 150–154.

Allison, M. A., Criqui, M. H., Wright, C. M., 2004. Patterns and risk factors for systemic calcified atherosclerosis. Arteriosclerosis, Thrombosis, and Vascular Biology 24 (2), 331–336.

Arnoldi, E., Gebregziabher, M., Schoepf, U. J., Goldenberg, R., Ramos-Duran, L., Zwerner, P. L., Nikolaou, K., Reiser, M. F., Costello, P., Thilo, C., 2010. Automated computer-aided stenosis detection at coronary CT angiography: initial experience. European Radiology 20 (5), 1160–1167.

Arya, S., Mount, D. M., Netanyahu, N. S., Silverman, R., Wu, A. Y., 1998. An optimal algorithm for approximate nearest neighbor searching fixed dimensions. Journal of the ACM (JACM) 45 (6), 891–923.

Austen, W., Edwards, J., Frye, R., Gensini, G., Gott, V., Griffith, L., McGoon, D., Murphy, M., Roe, B., Apr 1975. A reporting system on patients evaluated for coronary artery disease. report of the ad hoc committee for grading of coronary artery disease, council on cardiovascular surgery, american heart association. Circulation 51 (4), 5–40.

Baker, A., da Silva, N., Quinn, D., Harte, A., Pagano, D., Bonser, R., Kumar, S., McTernan, P., 2006. Human epicardial adipose tissue expresses a pathogenic profile of adipocytokines in patients with cardiovascular disease. Cardiovascular Diabetology 5 (1), 1–7.

Bankman, I., 2000. Handbook of medical imaging: processing and analysis, Registration. Academic Pr.

Bax, J., Beanlands, R., Klocke, F., Knuuti, J., Lammertsma, A., Schaefers, M., Schelbert, H., Von Schulthess, G., Shaw, L., Yang, G., et al., 2007. Diagnostic and clinical perspectives of fusion imaging in cardiology: is the total greater than the sum of its parts? Heart 93 (1), 16–22.

Bettencourt, N., Toschke, A., Leite, D., Rocha, J., Carvalho, M., Sampaio, F., Xara, S., Leite-Moreira, A., Nagel, E., Gama, V., 2011. Epicardial adipose tissue is an independent predictor of coronary atherosclerotic burden. International Journal of Cardiology 158 (1), 26–32.

Bos, D., Ikram, M. A., Elias-Smale, S. E., Krestin, G. P., Hofman, A., Witteman, J. C., van der Lugt, A., Vernooij, M. W., 2011. Calcification in major vessel beds relates to vascular brain disease. Arteriosclerosis, Thrombosis, and Vascular Biology 31 (10), 2331–2337.

Bos, D., Ikram, M. A., Isaacs, A., Verhaaren, B. F., Hofman, A., van Duijn, C. M., Witteman, J. C., van der Lugt, A., Vernooij, M. W., 2013. Genetic loci for coronary calcification and serum lipids relate to aortic and carotid calcification. Circulation: Cardiovascular Genetics 6 (1), 47–53.

Bos, D., van der Rijk, M. J., Geeraedts, T. E., Hofman, A., Krestin, G. P., Witteman, J. C., van der Lugt, A., Ikram, M. A., Vernooij, M. W., 2012. Intracranial carotid artery atherosclerosis prevalence and risk factors in the general population. Stroke 43 (7), 1878–1884.

Broersen, A., Kitslaar, P., Frenay, M., Dijkstra, J., 2012. Frenchcoast: Fast, robust extraction for the nice challenge on coronary artery segmentation of the tree. In: Proceedings of MICCAI Workshop "3D Cardiovascular Imaging: a MICCAI segmentation Challenge".

Budoff, M. J., Gul, K. M., 2008. Expert review on coronary calcium. Vascular Health and Risk Management 4 (2), 315–324.

Budoff, M. J., Shaw, L. J., Liu, S. T., Weinstein, S. R., Mosler, T. P., Tseng, P. H., Flores, F. R., Callister, T. Q., Raggi, P., Berman, D. S., 2007. Long-term prognosis associated with coronary calcification: observations from a registry of 25,253 patients. Journal of the American College of Cardiology 49 (18), 1860–1870.

Cademartiri, F., La Grutta, L., Malagò, R., Alberghina, F., Meijboom, W. B., Pugliese, F., Maffei, E., Palumbo, A. A., Aldrovandi, A., Fusaro, M., et al., 2008. Prevalence of anatomical variants and coronary anomalies in 543 consecutive patients studied with 64-slice CT coronary angiography. European Radiology 18 (4), 781–791.

Callister, T. Q., Cooil, B., Raya, S. P., Lippolis, N. J., Russo, D. J., Raggi, P., 1998. Coronary artery disease: improved reproducibility of calcium scoring with an electron-beam CT volumetric method. Radiology 208 (3), 807–814.

Carreira-Perpinan, M. A., 2007. Gaussian mean-shift is an EM algorithm. IEEE Transactions on Pattern Analysis and Machine Intelligence 29 (5), 767–776.

Cerqueira, M. D., Weissman, N. J., Dilsizian, V., Jacobs, A. K., Kaul, S., Laskey, W. K., Pennell, D. J., Rumberger, J. A., Ryan, T., Verani, M. S., et al., 2002. Standardized myocardial segmentation and nomenclature for tomographic imaging of the heart a statement for healthcare professionals from the cardiac imaging committee of the council on clinical cardiology of the american heart association. Circulation 105 (4), 539–542.

Cetin, S., Unal, G., 2012. Automatic detection of coronary artery stenosis in CTA based on vessel intensity and geometric features. In: Proceedings of MICCAI Workshop "3D Cardiovascular Imaging: a MICCAI segmentation Challenge".

Cheng, K., Chu, C., Lee, K., Lin, T., Hsieh, C., Chiu, C., Voon, W., Sheu, S., Lai, W., 2007. Adipocytokines and proinflammatory mediators from abdominal and epicardial adipose tissue in patients with coronary artery disease. International Journal of Obesity 32 (2), 268–274.

Comaniciu, D., Meer, P., 2002. Mean shift: A robust approach towards feature space analysis. IEEE Transactions on Pattern Analysis and Machine Intelligence 24 (5), 603–619.

de Vos, A. M., Prokop, M., Roos, C. J., Meijs, M. F., van der Schouw, Y. T., Rutten, A., Gorter, P. M., Cramer, M.-J., Doevendans, P. A., Rensing, B. J., et al., 2008. Peri-coronary epicardial adipose tissue is related to cardiovascular risk factors and coronary artery calcification in post-menopausal women. European Heart Journal 29 (6), 777–783.

de Weert, T., Cakir, H., Rozie, S., Cretier, S., Meijering, E., Dippel, D., van der Lugt, A., 2009. Intracranial internal carotid artery calcifications: association with vascular risk factors and ischemic cerebrovascular disease. American Journal of Neuroradiology 30 (1), 177–184.

Debruyne, M., Hubert, M., Suykens, J. A., 2008. Model selection in kernel based regression using the influence function. Journal of Machine Learning Research 9, 2377–2400.

Detrano, R., Guerci, A. D., Carr, J. J., Bild, D. E., Burke, G., Folsom, A. R., Liu, K., Shea, S., Szklo, M., Bluemke, D. A., et al., 2008. Coronary calcium as a predictor of coronary events in four racial or ethnic groups. New England Journal of Medicine 358 (13), 1336–1345.

Dey, D., Nakazato, R., Li, D., Berman, D. S., 2012. Epicardial and thoracic fat-noninvasive measurement and clinical implications. Cardiovascular Diagnosis and Therapy 2 (2), 85–93.

Dey, D., Suzuki, Y., Suzuki, S., Ohba, M., Slomka, P. J., Polk, D., Shaw, L. J., Berman, D. S., 2008. Automated quantitation of pericardiac fat from noncontrast CT. Investigative Radiology 43 (2), 145–153.

Dey, D., Wong, N. D., Tamarappoo, B., Nakazato, R., Gransar, H., Cheng, V. Y., Ramesh, A., Kakadiaris, I., Germano, G., Slomka, P. J., et al., 2010. Computer-aided non-contrast CT-based quantification of pericardial and thoracic fat and their associations with coronary calcium and metabolic syndrome. Atherosclerosis 209 (1), 136–141.

Dijkstra, E. W., 1959. A note on two problems in connexion with graphs. Numerische Mathematik 1 (1), 269–271.

Ding, J., Hsu, F.-C., Harris, T. B., Liu, Y., Kritchevsky, S. B., Szklo, M., Ouyang, P., Espeland, M. A., Lohman, K. K., Criqui, M. H., et al., 2009. The association of pericardial fat with incident coronary heart disease: the multi-ethnic study of atherosclerosis (MESA). The American Journal of Clinical Nutrition 90 (3), 499–504.

Ding, J., Kritchevsky, S. B., Harris, T. B., Burke, G. L., Detrano, R. C., Szklo, M., Carr, J. J., 2008. The association of pericardial fat with calcified coronary plaque. Obesity 16 (8), 1914–1919.

Duval, M., Ouzeau, E., Precioso, F., Matuszewski, B., 2012. Coronary artery stenoses detection with random forest. In: Proceedings of MICCAI Workshop "3D Cardiovascular Imaging: a MICCAI segmentation Challenge".

Elias-Smale, S. E., Proença, R. V., Koller, M. T., Kavousi, M., van Rooij, F. J., Hunink, M. G., Steyerberg, E. W., Hofman, A., Oudkerk, M., Witteman, J. C., 2010. Coronary calcium score improves classification of coronary heart disease risk in the elderly: The Rotterdam Study. Journal of the American College of Cardiology 56 (17), 1407–1414.

Elias-Smale, S. E., Wieberdink, R. G., Odink, A. E., Hofman, A., Hunink, M. G., Koudstaal, P. J., Krestin, G. P., Breteler, M. M., van der Lugt, A., Witteman, J. C., 2011. Burden of atherosclerosis improves the prediction of coronary heart disease but not cerebrovascular events: The Rotterdam Study. European Heart Journal 32 (16), 2050–2058.

Elkeles, R., 2008. Computed tomography imaging, coronary calcium and atherosclerosis. Expert review of cardiovascular therapy 6 (8), 1083–1093.

Eslami, A., Aboee, A., Hodaei, Z., Moghaddam, M. J., Carlier, S., Katouzian, A., Navab, N., 2012. Quantification of coronary arterial stenosis by inflating tubes in CTA images. In: Proceedings of MICCAI Workshop "3D Cardiovascular Imaging: a MICCAI segmentation Challenge".

Fayad, Z., Fuster, V., 2001. Clinical imaging of the high-risk or vulnerable atherosclerotic plaque. Circulation Research 89 (4), 305–316.

Ficaro, E. P., Lee, B. C., Kritzman, J. N., Corbett, J. R., 2007. Corridor4DM: the Michigan method for quantitative nuclear cardiology. Journal of Nuclear Cardiology 14 (4), 455–465.

Flórez-Valencia, L., Orkisz, M., Jerez, R. A. C., González, J. S. T., Agudelo, E. M. C., Mouton, C., Hoyos, M. H., et al., 2012. Coronary artery segmentation and stenosis quantification in CT images with use of a right generalized cylinder model. In: Proceedings of MICCAI Workshop "3D Cardiovascular Imaging: a MICCAI segmentation Challenge".

Folks, R. D., 2002. Interpretation and reporting of myocardial perfusion SPECT: a summary for technologists. Journal of Nuclear Medicine Technology 30 (4), 153–163.

Frangi, A. F., Niessen, W. J., Vincken, K. L., Viergever, M. A., 1998. Multiscale vessel enhancement filtering. In: Medical Image Computing and Computer-Assisted Interventation-MICCAI. Vol. 1496. Springer, pp. 130–137.

Gaemperli, O., Husmann, L., Schepis, T., Koepfli, P., Valenta, I., Jenni, W., Alkadhi, H., Lüscher, T. F., Kaufmann, P. A., 2009. Coronary CT angiography and myocardial perfusion imaging to detect flow-limiting stenoses: a potential gatekeeper for coronary revascularization? European Heart Journal 30 (23), 2921–2929.

Gaemperli, O., Schepis, T., Kalff, V., Namdar, M., Valenta, I., Stefani, L., Desbiolles, L., Leschka, S., Husmann, L., Alkadhi, H., et al., 2007a. Validation of a new cardiac image fusion software for three-dimensional integration of myocardial perfusion SPECT and stand-alone 64-slice CT angiography. European Journal of Nuclear Medicine and Molecular Imaging 34 (7), 1097–1106.

Gaemperli, O., Schepis, T., Valenta, I., Husmann, L., Scheffel, H., Duerst, V., Eberli, F. R., Luscher, T. F., Alkadhi, H., Kaufmann, P. A., 2007b. Cardiac image fusion from stand-alone SPECT and CT: clinical experience. Journal of Nuclear Medicine 48 (5), 696–703.

Goldenberg, R., Eilot, D., Begelman, G., Walach, E., Ben-Ishai, E., Peled, N., 2012. Computer-aided simple triage (CAST) for coronary CT angiography (CCTA). International Journal of Computer Assisted Radiology and Surgery 7 (6), 819–827.

Greenland, P., LaBree, L., Azen, S. P., Doherty, T. M., Detrano, R. C., 2004. Coronary artery calcium score combined with Framingham score for risk prediction in asymptomatic individuals. JAMA: The Journal of the American Medical Association 291 (2), 210–215.

Gülsün, M. A., Tek, H., 2008. Robust vessel tree modeling. In: Medical Image Computing and Computer-Assisted Interventation-MICCAI. Vol. 5241. Springer, pp. 602–611.

Halpern, E. J., Halpern, D. J., 2011. Diagnosis of coronary stenosis with CT angiography: comparison of automated computer diagnosis with expert readings. Academic radiology 18 (3), 324–333.

Harada, K., Amano, T., Uetani, T., Tokuda, Y., Kitagawa, K., Shimbo, Y., Kunimura, A., Kumagai, S., Yoshida, T., Kato, B., et al., 2011. Cardiac 64-multislice computed tomography reveals increased epicardial fat volume in patients with acute coronary syndrome. The American Journal of Cardiology 108 (8), 1119–1123.

Hirata, Y., Tabata, M., Kurobe, H., Motoki, T., Akaike, M., Nishio, C., Higashida, M., Mikasa, H., Nakaya, Y., Takanashi, S., et al., 2011. Coronary atherosclerosis is associated with macrophage polarization in epicardial adipose tissue. Journal of the American College of Cardiology 58 (3), 248–255.

Hoff, J. A., Chomka, E. V., Krainik, A. J., Daviglus, M., Rich, S., Kondos, G. T., 2001. Age and gender distributions of coronary artery calcium detected by electron beam tomography in 35,246 adults. The American Journal of Cardiology 87 (12), 1335–1339.

Hofman, A., van Duijn, C. M., Franco, O. H., Ikram, M. A., Janssen, H. L., Klaver, C. C., Kuipers, E. J., Nijsten, T. E., Stricker, B. H. C., Tiemeier, H., et al., 2011. The Rotterdam Study: 2012 objectives and design update. European Journal of Epidemiology 26 (8), 657–686.

Hong, C., Becker, C. R., Schoepf, U. J., Ohnesorge, B., Bruening, R., Reiser, M. F., 2002. Coronary artery calcium: Absolute quantification in nonenhanced and contrast-enhanced multi–detector row CT studies. Radiology 223 (2), 474–480.

Iacobellis, G., 2012. Epicardial and pericardial fat: close, but very different. Obesity 17 (4), 625–625.

Iacobellis, G., Bianco, A. C., 2011. Epicardial adipose tissue: emerging physiological, pathophysiological and clinical features. Trends in Endocrinology and Metabolism 22 (11), 450–457.

Iacobellis, G., Pellicelli, A. M., Sharma, A. M., Grisorio, B., Barbarini, G., Barbaro, G., et al., 2007. Relation of subepicardial adipose tissue to carotid intima-media thickness in patients with human immunodeficiency virus. The American Journal of Cardiology 99 (10), 1470–1472.

Iacobellis, G., Pistilli, D., Gucciardo, M., Leonetti, F., Miraldi, F., Brancaccio, G., Gallo, P., di Gioia, C., 2005. Adiponectin expression in human epicardial adipose tissue in vivo is lower in patients with coronary artery disease. Cytokine 29 (6), 251–255.

Iacobellis, G., Willens, H. J., 2009. Echocardiographic epicardial fat: a review of research and clinical applications. Journal of the American Society of Echocardiography 22 (12), 1311–1319.

Isğum, I., van Ginneken, B., Olree, M., 2004. Automatic detection of calcifications in the aorta from CT scans of the abdomen: 3d computer-aided diagnosis. Academic Radiology 11 (3), 247–257.

Kalbfleisch, H., Hort, W., 1977. Quantitative study on the size of coronary artery supplying areas postmortem. American Heart Journal 94 (2), 183–188.

Kaufmann, P. A., 2009. Cardiac hybrid imaging: state-of-the-art. Annals of Nuclear Medicine 23 (4), 325–331.

Kelm, B. M., Mittal, S., Zheng, Y., Tsymbal, A., Bernhardt, D., Vega-Higuera, F., Zhou, S. K., Meer, P., Comaniciu, D., 2011. Detection, grading and classification of coronary stenoses in computed tomography angiography. In: Medical Image Computing and Computer-Assisted Intervention–MICCAI. Vol. 6893. Springer, pp. 25–32.

Khan, M. F., Wesarg, S., Gurung, J., Dogan, S., Maataoui, A., Brehmer, B., Herzog, C., Ackermann, H., Aßmus, B., Vogl, T. J., 2006. Facilitating coronary artery evaluation in MDCT using a 3D automatic vessel segmentation tool. European Radiology 16 (8), 1789–1795.

Kirişli, H., Schaap, M., Klein, S., Papadopoulou, S., Bonardi, M., Chen, C., Weustink, A., Mollet, N., Vonken, E., van der Geest, R., et al., 2010. Evaluation of a multi-atlas based method for segmentation of cardiac CTA data: a large-scale, multicenter, and multivendor study. Medical Physics 37 (12), 6279–6291.

Kirişli, H., Schaap, M., Metz, C., Dharampall, A., Meijboom, W., Papadopoulou, S., Dedic, A., Nieman, K., de Graaf, M., Meijs, M., et al., 2013. Standardized evaluation framework for evaluating coronary artery stenosis detection, stenosis quantification and lumen segmentation algorithms in computed tomography angiography. Medical Image Analysis 17 (8), 859–876.

Kirişli, H. A., Gupta, V., Kirschbaum, S. W., Rossi, A., Metz, C., Schaap, M., van Geuns, R. J., Mollet, N., Lelieveldt, B. P., Reiber, J. H., et al., 2012. Comprehensive visualization of multimodal cardiac imaging data for assessment of coronary artery disease: first clinical results of the SMARTVis tool. International Journal of Computer Assisted Radiology and Surgery 7 (4), 557–571.

Kitamura, Y., Li, Y., Ito, W., 2012. Automatic coronary extraction by supervised detection and shape matching. In: IEEE International Symposium on Biomedical Imaging (ISBI). IEEE, pp. 234–237.

Klein, S., Pluim, J. P., Staring, M., Viergever, M. A., 2009. Adaptive stochastic gradient descent optimisation for image registration. International Journal of Computer Vision 81 (3), 227–239.

Klein, S., Staring, M., Murphy, K., Viergever, M. A., Pluim, J. P., 2010. Elastix: a toolbox for intensity-based medical image registration. IEEE Transactions on Medical Imaging 29 (1), 196–205.

Kondos, G. T., Hoff, J. A., Sevrukov, A., Daviglus, M. L., Garside, D. B., Devries, S. S., Chomka, E. V., Liu, K., 2003. Electron-beam tomography coronary artery calcium and cardiac events a 37-month follow-up of 5635 initially asymptomatic low-to intermediate-risk adults. Circulation 107 (20), 2571–2576.

Kortelainen, M., 2002. Myocardial infarction and coronary pathology in severely obese people examined at autopsy. International Journal of Obesity 26 (1), 73–79.

Levine, G. N., Bates, E. R., Blankenship, J. C., Bailey, S. R., Bittl, J. A., Cercek, B., Chambers, C. E., Ellis, S. G., Guyton, R. A., Hollenberg, S. M., et al., 2011. 2011 ACCF/AHA/SCAI guideline for percutaneous coronary intervention:executive summary: A report of the american college of cardiology foundation/american heart association task force on practice guidelines and the society for cardiovascular angiography and interventions. Journal of the American College of Cardiology 58 (24), 2550–2583.

Lor, K., Chen, C., 2012. Probabilistic model based evaluation of coronary artery stenosis on CTA. In: Proceedings of MICCAI Workshop "3D Cardiovascular Imaging: a MICCAI segmentation Challenge".

Lusis, A., 2000. Atherosclerosis. Nature 407, 233–241.

Mahabadi, A. A., Berg, M. H., Lehmann, N., Kälsch, H., Bauer, M., Kara, K., Dragano, N., Moebus, S., Jöckel, K.-H., Erbel, R., et al., 2013. Association of epicardial fat with cardiovascular risk factors and incident myocardial infarction in the general population: The Heinz Nixdorf Recall Study. Journal of the American College of Cardiology 61 (13), 1388–1395.

Mahabadi, A. A., Massaro, J. M., Rosito, G. A., Levy, D., Murabito, J. M., Wolf, P. A., O'Donnell, C. J., Fox, C. S., Hoffmann, U., 2009. Association of pericardial fat, intrathoracic fat, and visceral abdominal fat with cardiovascular disease burden: the Framingham Heart Study. European Heart Journal 30 (7), 850–856.

Mahabadi, A. A., Reinsch, N., Lehmann, N., Altenbernd, J., Kälsch, H., Seibel, R. M., Erbel, R., Möhlenkamp, S., 2010. Association of pericoronary fat volume with atherosclerotic plaque burden in the underlying coronary artery: a segment analysis. Atherosclerosis 211 (1), 195–199.

Maintz, J., Viergever, M. A., 1998. A survey of medical image registration. Medical Image Analysis 2 (1), 1–36.

Martin Bland, J., Altman, D., 1986. Statistical methods for assessing agreement between two methods of clinical measurement. The Lancet 327 (8476), 307–310.

Mattes, D., Haynor, D. R., Vesselle, H., Lewellen, T. K., Eubank, W., 2003. PET-CT image registration in the chest using free-form deformations. IEEE Transactions on Medical Imaging 22 (1), 120–128.

Melchionna, S., Amati, G., Bernaschi, M., Bisson, M., Succi, S., Mitsouras, D., Rybicki, F. J., 2013. Risk assessment of atherosclerotic plaques based on global biomechanics. Medical Engineering and Physics, in press.

Melki, I., Talbot, H., Cousty, J., Pruvot, C., Knoplioch, J., Launay, L., Najman, L., 2012. Automatic coronary arteries stenoses detection in 3D CTA. In: Proceedings of MICCAI Workshop "3D Cardiovascular Imaging: a MICCAI segmentation Challenge".

Metz, C., Schaap, M., Weustink, A., Mollet, N., van Walsum, T., Niessen, W., 2009. Coronary centerline extraction from CT coronary angiography images using a minimum cost path approach. Medical Physics 36 (12), 5568–5579.

Miller, J. M., Rochitte, C. E., Dewey, M., Arbab-Zadeh, A., Niinuma, H., Gottlieb, I., Paul, N., Clouse, M. E., Shapiro, E. P., Hoe, J., et al., 2008. Diagnostic performance of coronary angiography by 64-row CT. New England Journal of Medicine 359 (22), 2324–2336.

Min, J. K., Leipsic, J., Pencina, M. J., Berman, D. S., Koo, B.-K., van Mieghem, C., Erglis, A., Lin, F. Y., Dunning, A. M., Apruzzese, P., et al., 2012. Diagnostic accuracy of fractional flow reserve from anatomic CT angiography. JAMA: The Journal of the American Medical Association 308 (12), 1237–1245.

Möhlenkamp, S., Lehmann, N., Schmermund, A., Pump, H., Moebus, S., Baumgart, D., Seibel, R., Grönemeyer, D. H., Jöckel, K.-H., Erbel, R., 2003. Prognostic value of extensive coronary calcium quantities in symptomatic males-a 5-year follow-up study. European Heart Journal 24 (9), 845–854.

Mohr, B., Masood, S., Plakas, C., 2012. Accurate lumen segmentation and stenosis detection and quantification in coronary CTA. In: Proceedings of MICCAI Workshop "3D Cardiovascular Imaging: a MICCAI segmentation Challenge".

Nakaura, T., Utsunomiya, D., Shiraishi, S., Tomiguchi, S., Honda, T., Ogawa, H., Awai, K., Yamashita, Y., 2005. Three-dimensional cardiac image fusion using new CT angiography and SPECT methods. American Journal of Roentgenology 185 (6), 1554–1557.

Nichols, J. H., Samy, B., Nasir, K., Fox, C. S., Schulze, P. C., Bamberg, F., Hoffmann, U., 2008. Volumetric measurement of pericardial adipose tissue from contrast-enhanced coronary computed tomography angiography: a reproducibility study. Journal of Cardiovascular Computed Tomography 2 (5), 288–295.

Odink, A., van der Lugt, A., Hofman, A., Hunink, M., Breteler, M., Krestin, G., Witteman, J., 2009. Risk factors for coronary, aortic arch and carotid calcification; The Rotterdam Study. Journal of Human Hypertension 24 (2), 86–92.

Odink, A. E., van der Lugt, A., Hofman, A., Hunink, M., Breteler, M., Krestin, G. P., Witteman, J., et al., 2007. Association between calcification in the coronary arteries, aortic arch and carotid arteries: The Rotterdam Study. Atherosclerosis 193 (2), 408–413.

Oeppen, J., Vaupel, J. W., 2002. Broken limits to life expectancy. Science 296 (5570), 1029–1031.

Ohnesorge, B., Flohr, T., Becker, C., Kopp, A. F., Schoepf, U. J., Baum, U., Knez, A., Klingenbeck-Regn, K., Reiser, M. F., 2000. Cardiac imaging by means of electrocardiographically gated multisection spiral CT: Initial experience. Radiology 217 (2), 564–571.

Ohnesorge, B., Flohr, T., Fischbach, R., Kopp, A., Knez, A., Schröder, S., Schöpf, U., Crispin, A., Klotz, E., Reiser, M., et al., 2002. Reproducibility of coronary calcium quantification in repeat examinations with retrospectively ECG-gated multisection spiral CT. European Radiology 12 (6), 1532–1540.

Öksüz, d., Ünay, D., Kadipaşaoğlu, K., 2012. A hybrid method for coronary artery stenosis detection and quantification. In: Proceedings of MICCAI Workshop "3D Cardiovascular Imaging: a MICCAI segmentation Challenge".

Oudkerk, M., Stillman, A. E., Halliburton, S. S., Kalender, W. A., Möhlenkamp, S., McCollough, C. H., Vliegenthart, R., Shaw, L. J., Stanford, W., Taylor, A. J., et al., 2008. Coronary artery calcium screening: current status and recommendations from the european society of cardiac radiology and north american society for cardiovascular imaging. The International Journal of Cardiovascular Imaging 24 (6), 645–671.

Peifer, J. W., Ezquerra, N. F., Cooke, C. D., Mullick, R., Klein, L., Hyche, M. E., Garcia, E., 1990. Visualization of multimodality cardiac imagery. IEEE Transactions on Biomedical Engineering 37 (8), 744–756.

Pereztol-Valdés, O., Candell-Riera, J., Santana-Boado, C., Angel, J., Aguadé-Bruix, S., Castell-Conesa, J., Garcia, E. V., Soler-Soler, J., 2005. Correspondence between left ventricular 17 myocardial segments and coronary arteries. European Heart Journal 26 (24), 637–2643.

Pham, D. L., Xu, C., Prince, J. L., 2000. Current methods in medical image segmentation. Annual Review of Biomedical Engineering 2 (1), 315–337.

Polonsky, T. S., McClelland, R. L., Jorgensen, N. W., Bild, D. E., Burke, G. L., Guerci, A. D., Greenland, P., 2010. Coronary artery calcium score and risk classification for coronary heart disease prediction. JAMA: The Journal of The American Medical Association 303 (16), 1610–1616.

Pugliese, F., Hunink, M., Gruszczynska, K., Alberghina, F., Malagó, R., van Pelt, N., Mollet, N., Cademartiri, F., Weustink, A., Meijboom, W., et al., 2009. Learning curve for coronary CT angiography: What constitutes sufficient training? Radiology 251 (2), 359–368.

Qian, Z., Anderson, H., Marvasty, I., Akram, K., Vazquez, G., Rinehart, S., Voros, S., 2010. Lesion-and vessel-specific coronary artery calcium scores are superior to whole-heart agatston and volume scores in the diagnosis of obstructive coronary artery disease. Journal of Cardiovascular Computed Tomography 4 (6), 391–399.

Raff, G. L., Abidov, A., Achenbach, S., Berman, D. S., Boxt, L. M., Budoff, M. J., Cheng, V., DeFrance, T., Hellinger, J. C., Karlsberg, R. P., 2009. SCCT guidelines for the interpretation and reporting of coronary computed tomographic angiography. Journal of Cardiovascular Computed Tomography 3 (2), 122–136.

Raggi, P., 2002. Coronary-calcium screening to improve risk stratification in primary prevention. The Journal of the Louisiana State Medical Society 154 (6), 314–318.

Reiber, J., Serruys, P. W., Kooijman, C. J., Wijns, W., Slager, C. J., Gerbrands, J., Schuurbiers, J., Den Boer, A., Hugenholtz, P., Feb 1985. Assessment of short-, medium-, and long-term variations in arterial dimensions from computer-assisted quantitation of coronary cineangiograms. Circulation 71 (2), 280–288.

Reilly, M. P., Lehrke, M., Wolfe, M. L., Rohatgi, A., Lazar, M. A., Rader, D. J., 2005. Resistin is an inflammatory marker of atherosclerosis in humans. Circulation 111 (7), 932–939.

Roger, V. L., Go, A. S., Lloyd-Jones, D. M., Benjamin, E. J., Berry, J. D., Borden, W. B., Bravata, D. M., Dai, S., Ford, E. S., Fox, C. S., et al., 2012. Heart disease and stroke statistics-2012 update a report from the american heart association. Circulation 125 (1), e2–e220.

Rohlfing, T., Brandt, R., Menzel, R., Maurer Jr, C. R., 2004. Evaluation of atlas selection strategies for atlas-based image segmentation with application to confocal microscopy images of bee brains. NeuroImage 21 (4), 1428–1442.

Rohlfing, T., Brandt, R., Menzel, R., Russakoff, D. B., Maurer Jr, C. R., 2005. Quo vadis, atlas-based segmentation? In: Handbook of Biomedical Image Analysis. Springer, pp. 435–486.

Rosen, B. D., Fernandes, V., McClelland, R. L., Carr, J. J., Detrano, R., Bluemke, D. A., Lima, J. A., 2009. Relationship between baseline coronary calcium score and demonstration of coronary artery stenoses during follow-up MESA (Multi-Ethnic Study of Atherosclerosis). JACC: Cardiovascular Imaging 2 (10), 1175–1183.

Rosito, G., Massaro, J., Hoffmann, U., Ruberg, F., Mahabadi, A., Vasan, R., OŠDonnell, C., Fox, C., 2008. Pericardial fat, visceral abdominal fat, cardiovascular disease risk factors, and vascular calcification in a community-based sample The Framingham Heart Study. Circulation 117 (5), 605–613.

Rueckert, D., Sonoda, L. I., Hayes, C., Hill, D. L., Leach, M. O., Hawkes, D. J., 1999. Nonrigid registration using free-form deformations: application to breast MR images. IEEE Transactions on Medical Imaging 18 (8), 712–721.

Rumberger, J. A., Simons, D. B., Fitzpatrick, L. A., Sheedy, P. F., Schwartz, R. S., 1995. Coronary artery calcium area by electron-beam computed tomography and coronary atherosclerotic plaque area: a histopathologic correlative study. Circulation 92 (8), 2157–2162.

Rybicki, F. J., Otero, H. J., Steigner, M. L., Vorobiof, G., Nallamshetty, L., Mitsouras, D., Ersoy, H., Mather, R. T., Judy, P. F., Cai, T., et al., 2008. Initial evaluation of coronary images from 320-detector row computed tomography. The international Journal of Cardiovascular Imaging 24 (5), 535–546.

Samet, H., Tamminen, M., 1988. Efficient component labeling of images of arbitrary dimension represented by linear bintrees. IEEE Transactions on Pattern Analysis and Machine Intelligence 10 (4), 579–586.

Sangiorgi, G., Rumberger, J. A., Severson, A., Edwards, W. D., Gregoire, J., Fitzpatrick, L. A., Schwartz, R. S., 1998. Arterial calcification and not lumen stenosis is highly correlated with atherosclerotic plaque burden in humans: a histologic study of 723 coronary artery segments using nondecalcifying methodology. Journal of the American College of Cardiology 31 (1), 126–133.

Santana, C. A., Sirineni, G. K., Esteves, F. P., Sanyal, R., Halkar, R., Ornelas, M., Verdes, L., Lerakis, S., Ramos, J. J., Aguadé-Bruix, S., et al., 2009. Diagnostic performance of fusion of myocardial perfusion and computed tomography coronary angiography. Journal of Nuclear Cardiology 16 (2), 201–211.

Sarin, S., Wenger, C., Marwaha, A., Qureshi, A., Go, B. D., Woomert, C. A., Clark, K., Nassef, L. A., Shirani, J., 2008. Clinical significance of epicardial fat measured using cardiac multislice computed tomography. The American Journal of Cardiology 102 (6), 767–771.

Sato, A., Nozato, T., Hikita, H., Miyazaki, S., Takahashi, Y., Kuwahara, T., Takahashi, A., Hiroe, M., Aonuma, K., 2010. Incremental value of combining 64-slice computed tomography angiography with stress nuclear myocardial perfusion imaging to improve noninvasive detection of coronary artery disease. Journal of Nuclear Cardiology 17 (1), 19–26.

Saur, S. C., Alkadhi, H., Desbiolles, L., Székely, G., Cattin, P. C., 2008. Automatic detection of calcified coronary plaques in computed tomography data sets. In: Medical Image Computing and Computer-Assisted Intervention–MICCAI 2008. Vol. 5241. Springer, pp. 170–177.

Schaap, M., Metz, C. T., van Walsum, T., van der Giessen, A. G., Weustink, A. C., Mollet, N. R., Bauer, C., Bogunović, H., Castro, C., Deng, X., et al., 2009a. Standardized evaluation methodology and reference database for evaluating coronary artery centerline extraction algorithms. Medical Image Analysis 13 (5), 701–714.

Schaap, M., Neefjes, L., Metz, C., van der Giessen, A., Weustink, A., Mollet, N., Wentzel, J., van Walsum, T., Niessen, W., 2009b. Coronary lumen segmentation using graph cuts and robust kernel regression. In: Information Processing in Medical Imaging. Vol. 5636. Springer, pp. 528–539.

Schindler, T. H., Magosaki, N., Jeserich, M., Oser, U., Krause, T., Fischer, R., Moser, E., Nitzsche, E., Zehender, M., Just, H., et al., 1999. Fusion imaging: combined visualization of 3D reconstructed coronary artery tree and 3D myocardial scintigraphic image in coronary artery disease. The International Journal of Cardiac Imaging 15 (5), 357–368.

Shahzad, R., Bos, D., Metz, C., Rossi, A., Kirişli, H., van der Lugt, A., Klein, S., Witteman, J., de Feijter, P., Niessen, W., van Vliet, L., van Walsum, T., 2013. Automatic quantification of epicardial fat volume on non-enhanced cardiac CT scans using a multi-atlas segmentation approach. Medical Physics 40 (9), 091910.

Shahzad, R., Schaap, M., van Walsum, T., Klien, S., Weustink, A., van Vliet, L., Niessen, W., 2010. A patient-specific coronary density estimate. In: IEEE International Symposium on Biomedical Imaging: From Nano to Macro. IEEE, pp. 9–12.

Shahzad, R., van Walsum, T., Kirisli, H., Tang, H., Metz, C., Schaap, M., van Vliet, L., Niessen, W., 2012a. Automatic stenoses detection, quantification and lumen segmentation of the coronary arteries using two-point centerline extraction scheme. In: Proceedings of MICCAI Workshop "3D Cardiovascular Imaging: a MICCAI segmentation Challenge".

Shahzad, R., van Walsum, T., Schaap, M., Rossi, A., Klein, S., Weustink, A. C., de Feyter, P. J., van Vliet, L. J., Niessen, W. J., 2012b. Vessel specific coronary artery calcium scoring: an automatic system. Academic Radiology 20 (1), 1–9.

Shaw, L. J., Raggi, P., Schisterman, E., Berman, D. S., Callister, T. Q., 2003. Prognostic value of cardiac risk factors and coronary artery calcium screening for all-cause mortality. Radiology 228 (3), 826–833.

Slomka, P. J., Cheng, V. Y., Dey, D., Woo, J., Ramesh, A., Van Kriekinge, S., Suzuki, Y., Elad, Y., Karlsberg, R., Berman, D. S., et al., 2009. Quantitative analysis of myocardial perfusion SPECT anatomically guided by coregistered 64-slice coronary CT angiography. Journal of Nuclear Medicine 50 (10), 1621–1630.

Steigner, M. L., Mitsouras, D., Whitmore, A. G., Otero, H. J., Wang, C., Buckley, O., Levit, N. A., Hussain, A. Z., Cai, T., Mather, R. T., et al., 2010. Iodinated contrast opacification gradients in normal coronary arteries imaged with prospectively ECG-gated single heart beat 320-detector row computed tomography. Circulation: Cardiovascular Imaging 3 (2), 179–186.

Suri, J., Wilson, D., Laxminarayan, S., 2005. Handbook of Biomedical Image Analysis: Volume III: Registration Models. Vol. 3. Plenum Pub Corp.

Taguchi, R., Takasu, J., Itani, Y., Yamamoto, R., Yokoyama, K., Watanabe, S., Masuda, Y., 2001. Pericardial fat accumulation in men as a risk factor for coronary artery disease. Atherosclerosis 157 (1), 203–209.

Tang, H., Walsum, T., van Onkelen, R. S., Hameeteman, R., Klein, S., Schaap, M., Tori, F. L., van den Bouwhuijsen, Q. J., Witteman, J., der Lugt, A., et al., 2012. Semiautomatic carotid lumen segmentation for quantification of lumen geometry in multispectral MRI. Medical Image Analysis 16 (6), 1201–1215.

Tessmann, M., Vega-Higuera, F., Fritz, D., Scheuering, M., Greiner, G., 2009. Multi-scale feature extraction for learning-based classification of coronary artery stenosis. In: SPIE Medical Imaging. International Society for Optics and Photonics, pp. 726002–726002.

Theodoridis S, K. K., 2009. Pattern Recognition. Academic Press.

Thomas, S. Y., Harmancey, R., Taegtmeyer, H., 2010. Fat around the heart. JACC: Cardiovascular Imaging 3 (7), 786–787.

Thompson, R. C., Allam, A. H., Lombardi, G. P., Wann, L. S., Sutherland, M. L., Sutherland, J. D., Soliman, M. A.-T., Frohlich, B., Mininberg, D. T., Monge, J. M., et al., 2013. Atherosclerosis across 4000 years of human history: the Horus study of four ancient populations. The Lancet 381 (9873), 1211–1222.

van Walsum, T., Schaap, M., Metz, C., van der Giessen, A., Niessen, W., 2008. Averaging centerlines: mean shift on paths. In: Medical Image Computing and Computer-Assisted Intervention–MICCAI 2008. Vol. 5241. Springer, pp. 900–907.

Vliegenthart, R., Oudkerk, M., Hofman, A., Oei, H.-H. S., van Dijck, W., van Rooij, F. J., Witteman, J. C., 2005. Coronary calcification improves cardiovascular risk prediction in the elderly. Circulation 112 (4), 572–577.

Wang, C., Moreno, R., Smedby, Ö., 2012. Vessel segmentation using implicit model-guided level sets. In: Proceedings of MICCAI Workshop "3D Cardiovascular Imaging: a MICCAI segmentation Challenge".

Wayhs, R., Zelinger, A., Raggi, P., 2002. High coronary artery calcium scores pose an extremely elevated risk for hard events. Journal of the American College of Cardiology 39 (2), 225–230.

Wesarg, S., Khan, M., Firle, E., 2006. Localizing calcifications in cardiac CT data sets using a new vessel segmentation approach. Journal of Digital Imaging 19 (3), 249–257.

Weustink, A., de Feyter, P., 2011. The role of multi-slice computed tomography in stable angina management: a current perspective. Netherlands Heart Journal 19 (7-8), 1–8.

Weustink, A. C., Mollet, N. R., Pugliese, F., Meijboom, W. B., Nieman, K., Heijenbrok-Kal, M. H., Flohr, T. G., Neefjes, L. A., Cademartiri, F., de Feyter, P. J., et al., 2008. Optimal electrocardiographic pulsing windows and heart rate: Effect on image quality and radiation exposure at dual-source coronary CT angiography. Radiology 248 (3), 792–798.

Wheeler, G. L., Shi, R., Beck, S. R., Langefeld, C. D., Lenchik, L., Wagenknecht, L. E., Freedman, B. I., Rich, S. S., Bowden, D. W., Chen, M. Y., et al., 2005. Pericardial and visceral adipose tissues measured volumetrically with computed tomography are highly associated in type 2 diabetic families. Investigative Radiology 40 (2), 97–101.

WHO, 2012. Cardiovascular Diseases, Fact sheet 317. World Health Organization.

Williams, M., Shaw, L. J., Raggi, P., Morris, D., Vaccarino, V., Liu, S. T., Weinstein, S. R., Mosler, T. P., Tseng, P. H., Flores, F. R., et al., 2008. Prognostic value of number and site of calcified coronary lesions compared with the total score. JACC: Cardiovascular Imaging 1 (1), 61–69.

Xu, Y., Liang, G., Hu, G., Yang, Y., Geng, J., Saha, P. K., 2012. Quantification of coronary arterial stenoses in CTA using fuzzy distance transform. Computerized Medical Imaging and Graphics 36 (1), 11–24.

Yang, G., Kitslaar, P., Frenay, M., Broersen, A., Boogers, M. J., Bax, J. J., Reiber, J. H., Dijkstra, J., 2012. Automatic centerline extraction of coronary arteries in coronary computed tomographic angiography. The International Journal of Cardiovascular Imaging 28 (4), 921–933.

Yoshizumi, T., Nakamura, T., Yamane, M., Islam, A., Menju, M., Yamasaki, K., Arai, T., Kotani, K., Funahashi, T., Yamashita, S., et al., 1999. Abdominal fat: Standardized technique for measurement at CT. Radiology 211 (1), 283–286.

Zambal, S., Hladuvka, J., Kanitsar, A., Bühler, K., 2008. Shape and appearance models for automatic coronary artery tracking. The Insight Journal 4.

Zuluaga, M. A., Magnin, I. E., Hoyos, M. H., Leyton, E. J. D., Lozano, F., Orkisz, M., 2011. Automatic detection of abnormal vascular cross-sections based on density level detection and support vector machines. International Journal of Computer Assisted Radiology and Surgery 6 (2), 163–174.

Layman's summary

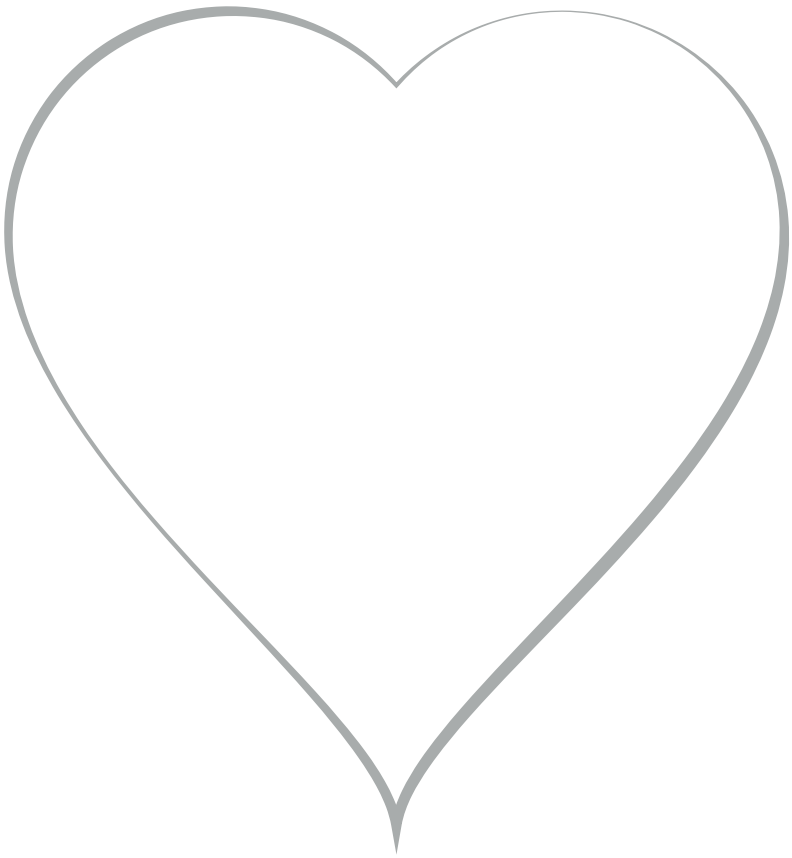

For better management of cardiovascular disease, it is of utmost importance to categorize the subjects into different risk groups. This categorization can be made based on cardiovascular risk factors including the family history of the subject. Imaging techniques play an increasing role in order to assess cardiovascular risk factors. In this thesis we set out to develop and evaluate automatic techniques for the extraction of quantitative imaging biomarkers for coronary artery disease (CAD).

One of the important cardiovascular risk factor is the presence of calcium in the arteries. We presented an automatic method that can compute the amount of calcium scores for the whole heart as well as for each of the coronary arteries from CT data. The system also categorizes patients into different risk groups. This vessel specific calcium lesion information can be used for treatment planning and assessing progression of CAD in follow up studies. The possibility to assign calcium to individual coronary arteries was possible owing to the 'Coronary Density Estimate'.

The second imaging biomarker is epicardial fat volume. We present a method that can accurately quantify the amount of epicardial fat volume. It was demonstrated that the method performs as good as the manual observers, hence has great potential to be used in daily clinical practice. In a clinical study on 2298 subjects it was demonstrated that indeed larger volumes of epicardial fat volumes were related to larger volumes of calcified lesions in the various vessel beds. The potential of this biomarker will need to be established in multiple larger studies.

The third imaging biomarker in CAD considered in this thesis is coronary artery stenosis grade. Accurate detection and quantification of coronary stenoses is of great importance, as this information is very important for the clinician in order to make accurate treatment selection and planning. We investigated the ability of detecting and quantifying coronary stenoses from CTA data. We demonstrated that the vessel lumen can be segmented with a precision similar to the human observers, but that it is still a challenge to be able to distinguish between significant and non-significant lesions.

Quantitative imaging biomarkers in CAD may provide both anatomical and functional information, and are often obtained from different imaging modalities. An important subject with respect to treatment planning is therefore the ability to combine information from different modalities in an integrated display. The SMARTVis system was introduced to fuse anatomical information from CTA scans and functional information from SPECT-MPI into one display. The integrated visualization proposed in the SMARTVis system enables a one-stop-shop visual exploration of cardiac anatomical and functional data, to maximally exploit the complementary information of multiple imaging modalities. It has been confirmed that such comprehensive visualizations allow to effectively relate perfusion defects and coronary lesions, and that fused integrated analysis leads to a more accurate diagnosis.

Automatic image processing plays an increasingly important role. Not only to extract relevant quantitative imaging biomarkers from CT imaging data, but also establish with what accuracy they can be assessed. For a number of relevant cardiovascular quantitative imaging biomarkers, this thesis has provided the required methodology.

Samenvatting

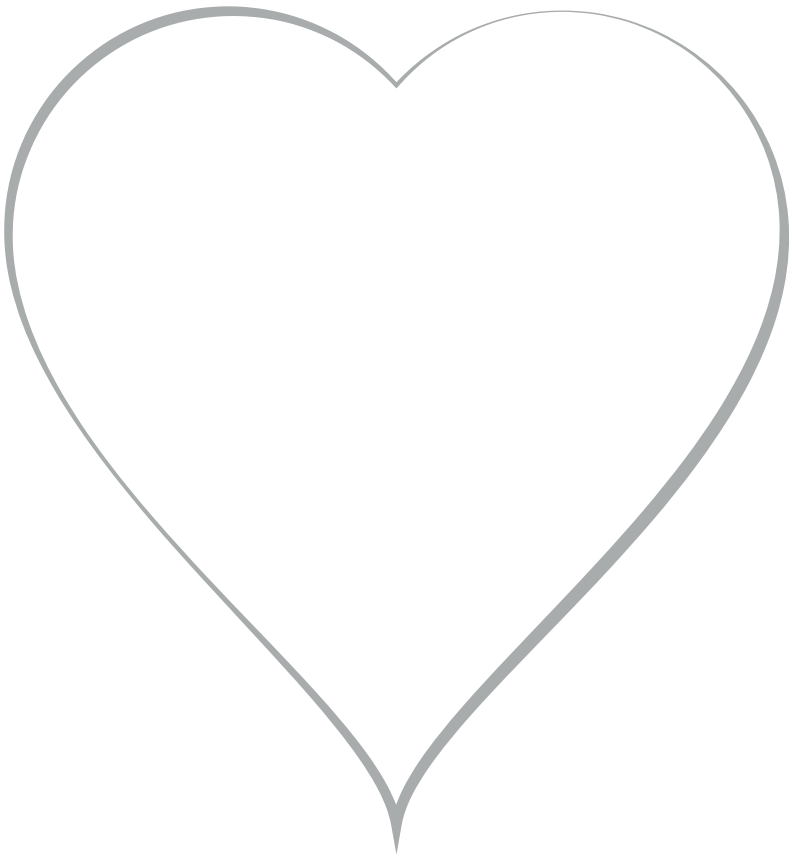

Voor beter behandeling van cardiovasculaire aandoeningen is het belangrijk om de patiënten in te delen in verschillende risicogroepen. Deze verdeling wordt gebaseerd op risicofactoren voor hart- en vaatziekten, inclusief de familiegeschiedenis van de patiënt. Beeldvormende technieken spelen een steeds grotere rol bij het bepalen van deze risicofactoren. In dit proefschrift ontwikkelen en evalueren we automatische technieken voor het bepalen van kwantitatieve biomarkers uit beelden voor ziekte van de kransslagaders (KSZ).

Een van de belangrijkste biomarkers voor hart- en vaatziekte is de aanwezigheid van calcium in de vaten. Wij hebben een automatische methode ontwikkeld om de hoeveelheid calcium voor het hele hart en voor elk van de kransslagaders te berekenen op basis van een CTA afbeelding. Deze informatie kan worden gebruikt voor de behandeling, en ook voor voortgangsbeoordeling van KSZ. Om de hoeveelheid calcium voor individuele kransslagaders te bepalen ontwikkelden we de 'Coronary Density Estimate'.

De tweede biomarker is het vetvolume rondom het hart. Wij presenteren een methode om dit nauwkeurig te meten. Gebleken is dat deze methode net zo goed werkt als bestaande methodes, en dus een groot potentieel heeft om te worden gebruikt in de dagelijkse klinische praktijk. Bij een klinische studie op 2298 patiënten werd aangetoond dat een grotere hoeveelheid vet rondom het hart inderdaad verband hield met grotere volumes van calcium in de verschillende vaatbedden. De hoeveelheid vet kan dus gezien worden als een onafhankelijke biomarker. Het belang van deze biomarker zal moeten worden vastgesteld in meerdere grote studies. De derde biomarker voor KSZ is de mate van vernauwing van de kransslagader. Nauwkeurige detectie en kwantificering van vernauwing in kransslagaders is van groot belang, aangezien deze informatie noodzakelijk is voor een arts om de juiste behandeling te kunnen kiezen. We onderzochten de mogelijkheid tot het opsporen en kwantificeren van vernauw ingingen in kransslagaders in CTA beelden. We toonden aan dat het lumen van het vat met onze methode net zo goed kan worden bepaald als door menselijke waarnemers, maar dat het nog een uitdaging is om onderscheid te maken tussen belangrijke en onbelangrijke vernauwingen.

Kwantitatieve biomarkers uit beelden in KSZ kunnen zowel anatomische en functionele informatie verschaffen, en vaak van verschillende beeldvormende modaliteiten worden verkregen. De mogelijkheid om informatie van verschillende modaliteiten in een geïntegreerd display te combineren is daarom belangrijk voor de behandeling. Het SMARTVis systeem werd ontwikkeld om een geÃŕntegreerde visualisatie van anatomische informatie uit CTA beelden en functionele informatie uit SPECT-MPI beelden mogelijk te maken, om zo het maximale te halen uit informatie van meerdere beeldvormende modaliteiten. Het is gebleken dat dergelijke uitgebreide visualisaties effectief tot een meer accurate diagnose kunnen leiden.

De automatische beeldverwerking speelt een steeds belangrijkere rol. Dit proefschrift heeft de vereiste methodologie verstrekt om een aantal relevante biomarkers voor hart- en vaatziekten uit beelden te kunnen bepalen.

Publications

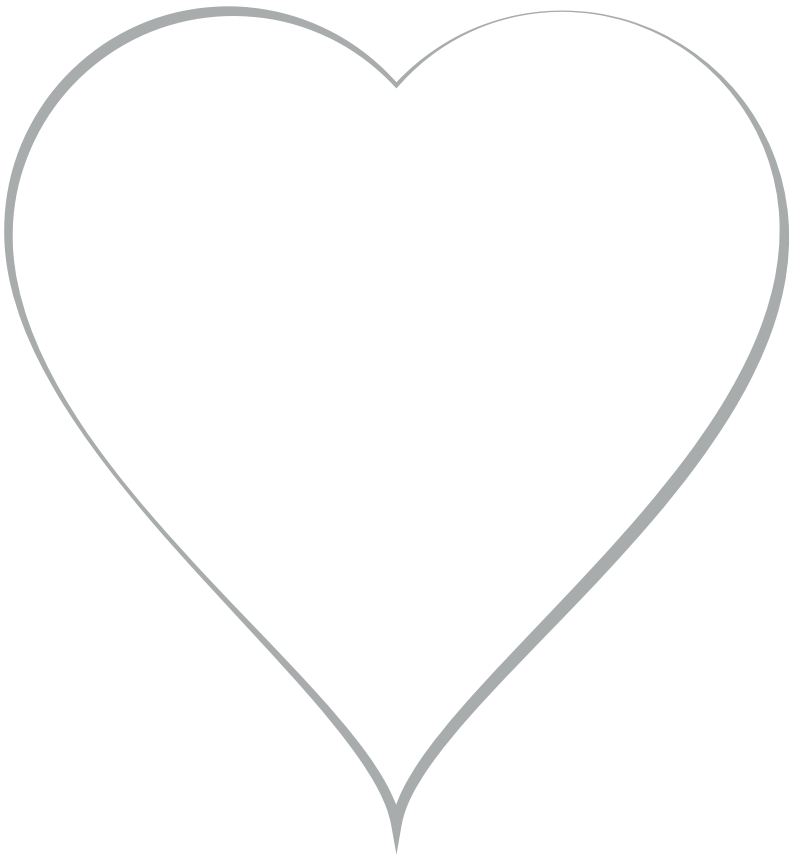

Journal Papers

- **R. Shahzad**, T. van Walsum, M. Schaap, A. Rossi, S. Klein, A.C. Weustink, P. de Feyter, L.J. van Vliet and W.J. Niessen, Vessel Specific Coronary Artery Calcium Scoring: An Automatic System, *Academic Radiology*, 20(1):1–9, 2013.

- H. Tang, T. van Walsum, K. Hameeteman **R. Shahzad**, L.J. van Vliet and W.J. Niessen, Lumen Segmentation and Stenosis Quantification of Atherosclerotic Carotid Arteries in CTA Utilizing a Centerline Intensity Prior, *Medical Physics*, 40(5):051721, 2013.

- **R. Shahzad***, H.A. Kirişli*, C. Metz, H. Tang, W.J. Niessen, L. van Vliet and T. van Walsum *(* both authors contributed equally to this research)*, Automatic Segmentation, Detection and Quantification of Coronary Artery Stenoses on CTA, *International Journal of Cardiovascular Imaging*, in press.

- H.A. Kirişli*, V. Gupta*, **R. Shahzad***, I. Al Younis, A. Dharampal, R.-J.M. van Geuns, A. Scholte, M.A. de Graaf, R.M.S. Joemai, K. Nieman, L. van Vliet, T. van Walsum, B.P.F. Lelieveldt and W.J. Niessen *(* shared first authorship)*, Additional diagnostic value of integrated analysis of cardiac CTA and SPECT-MPI using the SMARTVis system in patients with suspected coronary artery disease, *Journal of Nuclear Medicine*, in press.

- **R. Shahzad**, D. Bos, C. Metz, A. Rossi, H.A. Kirişli, A. van der Lugt, S. Klein, J. Witteman, P. de Feyter, W.J. Niessen, L.J. van Vliet and T. van Walsum, Automatic Quantification of Epicardial Fat Volume on Non-enhanced Cardiac CT Scans Using a Multi-Atlas Segmentation Approach, *Medical Physics*, in press.

- H.A. Kirişli, M. Schaap, C. Metz, A.S. Dharampal, W.B. Meijboom, S.L. Papadopoulou, A. Dedic, K. Nieman, M.A. de Graaf, M.F.L. Meijs, M.J. Cramer, A. Broersen, S. Cetin, A. Eslami, L. Flórez-Valencia, K.L. Lor, B. Matuszewski, I. Melki, B. Mohr, I. Öksüz, **R. Shahzad**, C. Wang, P.H. Kitslaar, G. Unal, A. Katouzian, M. Orkisz, C.M. Chen, F. Precioso, L. Najman, S. Masood, D. Ünay, L. van Vliet, R. Moreno, R. Goldenberg, E. Vuçini, G.P. Krestin, W.J. Niessen, T. van Walsum, Standardized evaluation framework for evaluating coronary artery stenoses detection, stenoses quantification and lumen segmentation algorithms in Computed Tomography Angiography, *Medical Image Analysis*, 17(8):859–876, 2013.

- D. Bos, **R. Shahzad**, A. van der Lugt, S. Klein, J. Witteman, P. de Feyter, W.J. Niessen, L.J. van Vliet and T. van Walsum, Epicardial fat volume is related to atherosclerotic calcification in multiple vessel beds, *Submitted.*

Conference Papers

- **R. Shahzad**, M. Schaap, T. van Walsum, S. Klein, A.C. Weustink, L.J. van Vliet and W.J. Niessen, A Patient-Specific Coronary Density Estimate, *Proc. IEEE*

International Symposium on Biomedical Imaging: from Nano to Macro (ISBI), 9–12, 2010.

- **R. Shahzad**, M. Schaap, F.B. Goncalves, C.T. Metz, H. Tang, T. van Walsum, A. Moelker, L.J. van Vliet and W.J. Niessen, Automatic Detection of Calcified Lesions in the Descending Aorta using Contrast Enhanced CT Scans, *Proc. IEEE International Symposium on Biomedical Imaging: from Nano to Macro (ISBI)*, 250–253, 2012.
- **R. Shahzad**, T. van Walsum, H.A. Kirişli, H. Tang, C.T. Metz, M. Schaap, L.J. van Vliet and W.J. Niessen, Automatic detection, quantification and lumen segmentation of the coronary arteries using a two point centerline extraction scheme, *15th International Conference on Medical Image Computing and Computer Assisted Intervention - MICCAI - Workshop proceedings - 3D Cardiovascular Imaging: A MICCAI segmentation challenge*, 2012.

Conference Abstracts

- **R. Shahzad**, M. Schaap, T. van Walsum, S. Klein, A.C. Weustink, L.J. van Vliet and W.J. Niessen, Coronary Artery Density Estimate for Calcium Scoring in CT Scans, *Dutch Conference on Bio-Medical Engineering (BME)*, 2011.
- **R. Shahzad**, T. van Walsum, M. Schaap, S. Klein, L.J. van Vliet and W.J. Niessen, Vessel Specific Coronary Artery Calcium Scoring: An Automatic Method *NVPHBV Spring Meeting*, 2011.
- H.A. Kirişli, V. Gupta, **R. Shahzad**, S. Kirschbaum, A. Rossi, R.J. van Geuns, N.R.A. Mollet, B.P.F. Lelieveldt, J.H.C. Reiber, T. van Walsum and W.J. Niessen, SMARTVis: a computer-aided diagnosis system for comprehensive visualization and analysis of multi-modal cardiac imaging data for the assessment of coronary artery disease, *European Congress of Radiology (ECR)*, 2012.
- **R. Shahzad**, D Bos, C.T. Metz, H.A. Kirişli, A. van der Lugt, L. J. van Vliet, W.J. Niessen and T. van Walsum, Automatic method for quantification of pericardial fat on non-enhanced cardiac CT, *European Congress of Radiology (ECR)*, 2013.

Acknowledgments

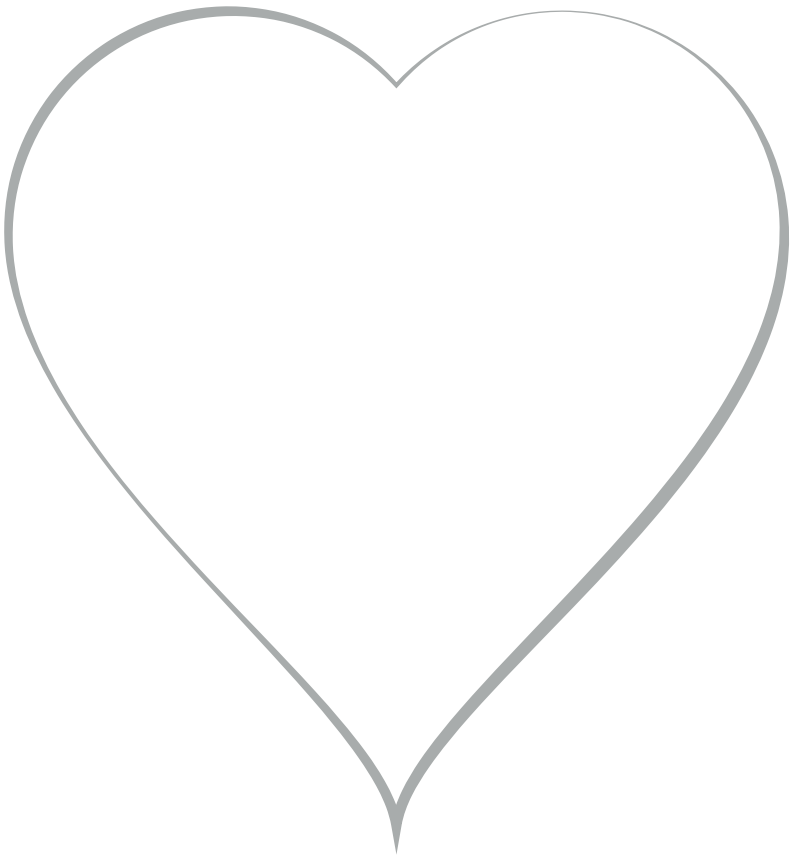

It was 24^{th} of November 2008, the first time I travelled to The Netherlands for an interview for a PhD position on the *'Heart in 3D'* project. I met a bunch of really nice folk some of them really tall, especially this very young and charismatic professor and chair of the BIGR group. Later that week I got a positive response. I was so eager, I wanted to start immediately. But due to all the visa issues I could arrive in The Netherlands only in March 2009. PhD life hasn't been very smooth, there were a few ups and downs. There were a lot of supporting and encouraging people around me who kept my spirits up and kept me going. Now, four and a half years later; I have learned a lot, gained so much experience and the most important part, completed my PhD thesis.

I want to take this opportunity to thank everyone who has contributed to this thesis, supported me and made my stay in Holland really enjoyable. I was part of this Medical Delta project and was a shared PhD student between TU Delft and Erasmus MC, being part of two universities and multiple departments meant that I met a lot of interesting people and was acquainted with many people, if I forgot to mention you here, my apologies.

My promotors and my copromotor – My first promotor Prof. Wiro Niessen. Dear Wiro, your energy, your enthusiasm and the the dedication towards the field of medical imaging is simply awesome. I want to thank you again for offering me the PhD position and guiding me throughout the journey. The insights you have in the field, the way you manage the group and the really friendly environment that you have created made it a real pleasure working with you. Not only are you a great professor but also an amazing football player, I had a lot of fun playing with you and against you during numerous BIGR/MI outings.

My second promotor Prof. Lucas van Vliet. Dear Lucas, I am really grateful for everything, the motivation, the enthusiasm, the approachability and the constant encouragement that you have provided me with. The regular progress meetings, the feedback that you provided me with and all the counselling sessions we had when I was going through difficult times have really helped me and kept me motivated. You also made sure that I had a regular and updated time schedule, this really helped with planning my tasks and made sure I finished most of the work on time. Though I didn't spend much part of the week at QI, we still had a lot of non-work related conversations during the regular coffee breaks.

My copromotor Dr. Theo van Walsum. Dear Theo, you have been a very great daily supervisor. We have always had such informal discussions which always helped me feel very comfortable. I am thankful for all the help and guidance you have provided me with. I would also like to thank you with all the help I received with regards to programming and debugging my MeVisLab modules. I also respect the tremendous amount of patience you have, you have read all my manuscripts a zillion times and made sure they are accurate and error free. I have also troubled you during weekends and during your vacations, you always found time for helping me out. I really enjoyed working with you and learned a lot from you. Thank you so much! I also had a lot of fun during the Wednesday night skate event, its not very common to go skating with your supervisor but you joined us.

My Paranymphs – Hortense, not only were you a colleague, a project mate and a room mate, but you are also a very good friend, a skating partner, a cinema company,

a travelling buddy, and the list just keeps on going. I really had fun working on the 'Heart in 3D' project and sitting in the same office for four years. The work that we did together has resulted in a few publications and three chapters in this thesis were a result of the collaborative work we did together. I also had fun during the conference trips, FIMH in Nice, BME at Egmond aan zee, ECR in Vienna and then the last conference of our PhD MICCAI in Nice. It was also a lot of fun travelling with you to help you with the apartment in Paris, the New years eve was a disappointment (without the fire works) but everything else was so much fun, Disney Land, Cirque du soleil, the pastries, croissants and all the other lovely things about Paris. I really enjoyed being your paranymph and now you are repaying the favour by standing next to me during my defence, thank you for that. Lastly, the last page of my thesis has a line of pink (not sure if its the right shade) hearts dedicated to you!

Gerardo, dude! You are such a fun guy to hang out with, you have also been my office mate for a short but fun time. I really enjoyed sharing the office on the 23^{rd} floor and also guiding you with the centerline extraction problems for your project. We have so many common interests, our love of food, movies, apple products and gadgets. You are also an amazing guitar player. Thank you for making my social life a lot of fun and convincing me to join the gym and make my lifestyle a bit healthier. Whenever you feel like going out for Sushi or having Indian food, give me a shout.

My colleagues and friends – First and foremost I would like to thank all the Dept. secretaries both at EMC and TUD, Petra, Desiree, Tinneke, Carmen, Mandy and Anjella. Petra and Mandy you have no idea how grateful I am to both of you. You have helped me in so many ways, work related, visa related and my personal issues. Life in Holland would have been very difficult without your help. I enjoyed going to Cirque du soleil Alegria with both of you. Petra, I had a lot of fun arranging the BIGR social events, the cooking workshops and the time spent with Thijs.

All my office mates, I spent most of the time at EMC on the 23^{rd} floor with Hortense and TT, later with Gerardo and Gijs. TT, thank you for all the brainstorm sessions we had and help with the centerline work, I think I in turn helped you with testing and finding bugs in your codes. All the best with finishing your thesis. Gerardo and Gijs, it was a short time in this office before we moved to the new building, I had fun with you guys. Other part of my time was spent in TUD with Ganesh, you always had so many questions, work related, political, cultural etc., we sometimes had real deep and insightful discussions which made me see things with a different perspective. Good luck with finalizing your PhD. A very short time was spent in the new building with Carolyn, Emilie, Esther, Eugene and Francesco, thank you guys for making my last few days in EMC fun and taking care of the big ass 'BIGR' plant that has been passed on over the generations.

All the CVIP'ers, these were great meetings! Coert my MeVisLab guru, thank you for helping me with all the troubles I had with everything related to it. Also, thank you for all the great ideas and suggestions you provided me for the papers. Michiel thank you for all the help you have provided me with, you really helped me kick start my PhD with all the great brainstorm sessions and all the programming help. Nora thank you for everything, especially 'the candy time'. You made the working environment more fun and I also had fun outside work, skating, stunt kite, BBQ, etc. Michiel and

Coert thank you for teaching me how to juggle, I haven't become as good as you but I can still throw and catch the balls.

All the past and present people at TUD: Ted, Bernd, Sjoerd, Piet, Frans, Ronald for reminding us its coffee time, all the technical help and making the environment so much fun, Wim for the amazing coffee, easter eggs, etc,. Lennard for the first hand experience of the events during a music festival, Milos for all the IFFR tickets you provided me with, Alex for all your crazy jokes and the bicycle trip to kinderdijk was really nice, Robiel for teaching me squash, one day I will beat you at it, Nadya, Jeroen, Zhang, Jelena, Vincent, Christiaan, Mojtaba, Jianfei, Qiaole, Sanneke, Mattan, Martijn, Arno, Rosalie, Arun, it was a lot of fun being with you guys, the interesting discussions during the coffee breaks, QI day out, after work drinks, sinterklas events, Christmas lunches etc.

All the past and present people at EMC: Azadeh, you were the first person at BIGR who I got in touch with, it was with your suggestions and feedback that I applied here, and look at me now 'I am done with the thesis', you have been a great support during the PhD time, it was a great pleasure being your paranymph, I hope you have a lot of fun at Oxford. Stefan the registration guru, thank you for all the help and all the suggestion with my papers. Erik, it was interesting having all the discussions, hope talking to me helped you with your spiritual quest. Marcel, thank you for helping me with all the CT and scanner related questions. Ihor, it was fun hanging with you and the interesting discussion about fishes, cameras and gadgets. Arna, it was fun arranging the dept. outing with you. Noemie, thank you for showing me around Barcelona. Esther, thank you for taking over the MISP responsibility. Diego and Andreas, it was a fun filled Formula 1 weekend at Spa. Marius, thank you for all the help with the cluster, all the interesting conversations and always encouraging me to talk in Dutch, good luck with finishing up your PhD. Jean-Marie, your love for learning new languages has left me baffled. Reinhard, all the conversations we had during the coffee breaks, all the best with your defence. Esben, I would never forget the ISBI in Barcelona. Emilie, it was a lot of fun arranging all the things during Hortense's defence, Mart, Jifke, Marleen, Henri, Fedde, Dirk, Renske, Marcel K, Hakim, Pierre, Joytirmoy, Karin, Valerio, Carolyn, Eugene, Luu, Annegreet, Wyke, Miroslav, Henk, Wei, Lejla, Danijela, Adrienne, I really enjoyed your company during all the dept. outings, events, movie nights and drinks.

People at LKEB: Boudwijn thank you for all the feedback during the Heart in 3D project meetings and Rob, thank you for your understanding and giving me some time off my post-doc to complete my PhD thesis. Trung, it was fun organizing MISP, I think we acquired some experience that we will never forget. Oleh, I have known you from the BIGR days and now, once again we are colleagues, thanks for teaching me how to fish. Pieter, thanks for all the suggestions during the Heart in 3D meetings. Alexander thank you for your help with the calcium scoring tool and helping me get in touch with the LUMC clinicians. Ahmed, it was fun hanging out with you and Nesma during the various events.

Heart in 3D project members: Bob, Prof. Reiber, Prof. de Roos, Robert-Jan, Gerrit-Anne, Marion, Emile, Albert, Michiel and all the other people involved, thank you for all your valuable feedback during the project meetings, this has helped me to finish my PhD work.

Alexia, you are a great friend you also helped me a lot with all the clinical related work. You were always so eager to help me, even with your real busy schedule you always found time to help me with my research, it was an honour standing next to you during your PhD, I hope to see you around soon, hope you have a nice time in Trieste. Ali bhai, I have to thank you for a lot of things but most importantly for convincing me to start doing a PhD soon after the masters, you have a tendency to keep disappearing I hope I can find you soon and give you a copy of this thesis. Mayalla my sweet flat mate, it was great living in the same flat with you, all the skating, cooking and Harry Potter talk we had, I wish you and Frans a very happy life in Sao Paulo and hope to come and visit you one day. Riri I am glad I met you, not because I get to eat all the different kinds of amazing cakes you bake, but because of the nice company and a friend that you are, I wish you and Ihor a very happy time together. Vikas, the third parter in crime from Heart in 3D, thank you for everything, you have been my guide in so many ways, you inspired me with your photography and convinced me to buy a camera, I really enjoy this hobby, I wish you and Shivani with a long and happy life together. Michael and Anoeshka, I had fun during your wedding, I could experience an Indian wedding in Holland which was awesome, also had a good time in Vienna during our photography quest. Tanveer it was so nice of you to come and visit me here, the euro trip we took together was quite memorable. Norton thank you for everything you have done for me, helping out mom during the tough times, thanks bro. Madhu you have been so encouraging, never grew tired of listening to my stories and all the kind words whenever I was feeling low really helped me keep going. Menaka and Niveditha, you always found time off your busy schedule to write to me, and ask how everything were, also your encouragement helped me during difficult times.

Frans, Christel, Anneroos and Jannike you are not only my neighbours but have made me feel like a part of your family. Thank you for everything you have done for me, inviting me for coffee, lunch, dinner, desserts, etc. You have also invited me on your family holidays, I am really glad to have found such loving and kind people. Frans, thank you for teaching me how to sail, I can now proudly tell that during my stay in Holland I learned a new skill. Also thank you for listening to all my constant problems and helping to fix them. Not to mention helping me with the cover of my PhD thesis, without your help I would have ended with circles instead of hearts. Christel thank you for translating my summery into Dutch. Floris the feline, who is always happy to keep me company when I am feeling lonely. I love you guys!

I would like to express my deepest gratitude to my Mom, you have always been so strong and have always put my interests before your own, even after going through the most difficult phase of your life you made sure that I finished what I set out to do, even though that would leave you alone. I really respect the strength of a mother, thank you Ammi for everything, hope I have made you proud. I would also like to thank all my uncles, aunts and cousins for supporting me and helping me in finishing this piece of work.

Last but not the least, I would like to thank Coffee. Oh Caffeine you have always been by me side when I needed you the most. Thank you for being there for me, I do not think I would have been able to finish this thesis without you!

About the author

Rahil Shahzad was born on 15 November 1985 in Bangalore, India.

He obtained his Bachelors in Engineering (BE) degree with Distinction in the field of Medical Electronics from M.S. Ramaiah Institute of Technology in 2007. During his final year of bachelor study he did his internship at GE Health Care, Bangalore.

Immediately after finishing his BE, Rahil started his Masters in the UK. He Graduated from The University of Warwick in 2009, by obtaining his M.Sc degree with Distinction in Advanced Biomedical Engineering. His M.Sc thesis was titled 'Early Diabetes Detection Using Infra-red Signatures' and was performed in close collaboration between the School of Engineering and Warwick Medical School.

In March 2009, Rahil started his PhD research. He was involved in the 'Heart in 3D' project which was performed in close collaboration with the Quantitative Imaging (QI) group, Delft University of Technology and at the Biomedical Imaging Group Rotterdam (BIGR), Erasmus MC. His research was in the field of cardiovascular image processing and mainly focused around CT imaging modality. This work resulted in a few automatic quantification methods for coronary calcium lesions and epicardial fat volume and has resulted in this thesis.

Since July 2013, he is a post-doctoral researcher at The Division on Image Processing (LKEB), Leiden University Medical Center.

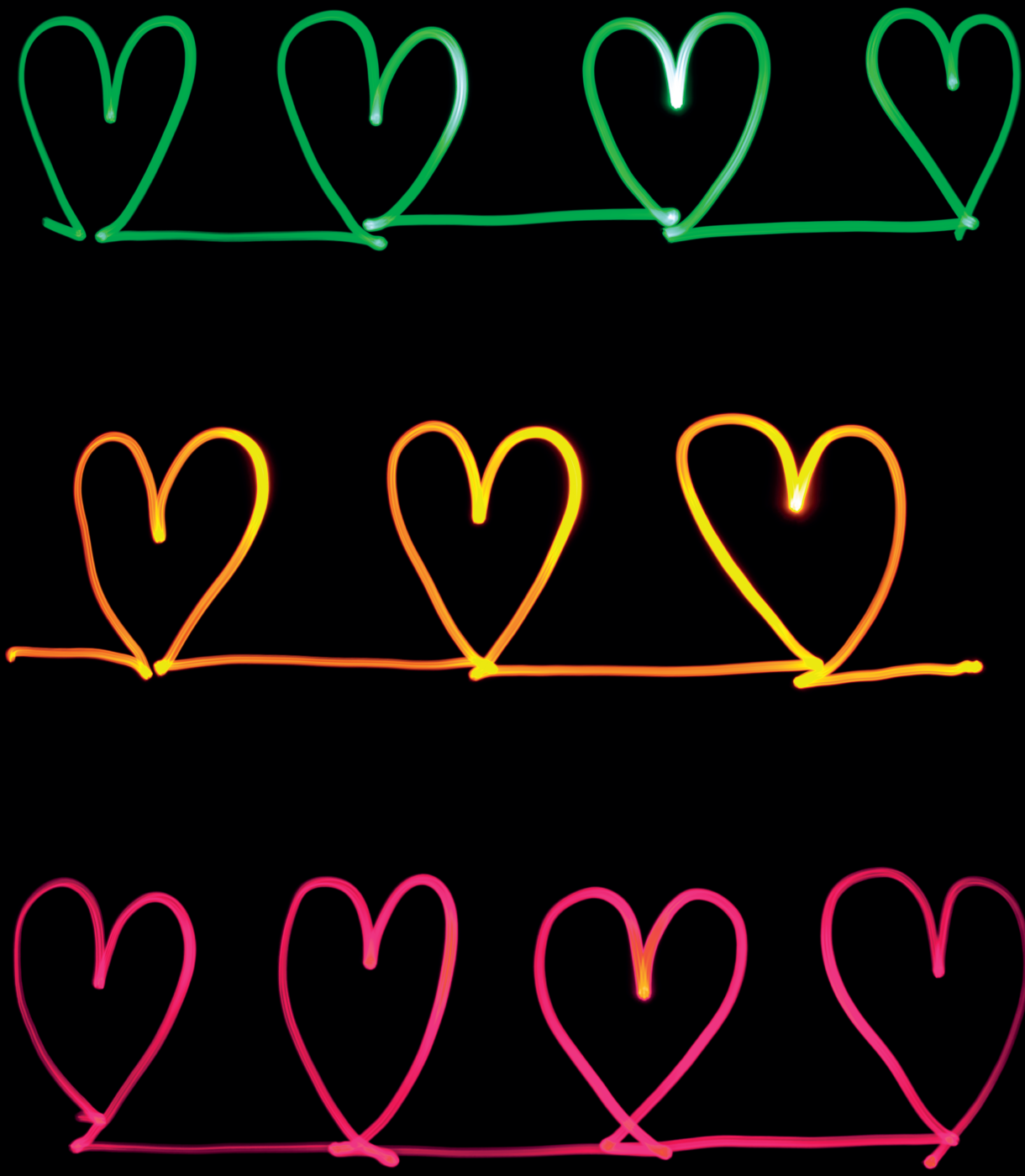

ISBN 978-90-6464-705-5